

THESIS FOR THE DEGREE OF DOCTOR OF PHILOSOPHY

# Ultralow-loss silicon nitride waveguides for nonlinear optics

Zhichao Ye



**CHALMERS**

Photonics Laboratory  
Department of Microtechnology and Nanoscience (MC2)  
CHALMERS UNIVERSITY OF TECHNOLOGY  
Gothenburg, Sweden, 2021

Ultralow-loss silicon nitride waveguides for nonlinear optics

Zhichao Ye

© Zhichao Ye, 2021

ISBN 978-91-7905-458-8

Doktorsavhandlingar vid Chalmers tekniska högskola, Ny series nr 4925  
ISSN 0346-718X

Chalmers University of Technology  
Department of Microtechnology and Nanoscience  
Photonics Laboratory  
SE-412 96 Göteborg  
Sweden  
Telephone: +46 (0)31-772 10 00

**Front cover illustration:** The schematic illustration of a dark pulse microcomb, a bright soliton microcomb and a parametric amplifier based on microring resonators and a spiral waveguide. The colors of the waveguides indicate the group velocity dispersion.

Printed by Chalmers digitaltryck, Chalmers tekniska högskola, Sweden,  
2021

# Ultralow-loss silicon nitride waveguides for nonlinear optics

Zhichao Ye

Photonics Laboratory

Department of Microtechnology and Nanoscience

Chalmers University of Technology

## Abstract

The field of nonlinear optics relies on the interaction between high-intensity optical waves and nonlinear media. An integrated waveguide with large refractive index contrast allows to highly confine optical waves in a sub- $\mu\text{m}^2$  area, thus enhancing the optical intensity. However, such a high optical confinement increases the susceptibility to scattering losses induced from nanometer-level inhomogeneities.

Silicon nitride is a dielectric material featuring a relatively large nonlinear-index coefficient and a broadband transparency window, from ultraviolet to mid-infrared. Its refractive index contrast to silica allows high confinement and controlling the dispersion with the waveguide geometry. This material platform has emerged in the past years as a workhorse for nonlinear optics applications that rely on the Kerr effect, from microcomb generation to parametric amplification. In this thesis work, we focused on the development of advanced manufacturing techniques for the realization of ultralow-loss silicon nitride waveguides. Meter long high-confinement waveguides with record low losses in the order of 1.4 dB/m and dispersion-engineered microresonators with quality factors of 19 million are reported. Based on this technology, we demonstrated octave-spanning coherent microcombs and microcombs with photodetectable repetition rates occupying a device area less than  $1\text{ mm}^2$ , i.e., one order of magnitude smaller than state of the art. The high yield and ultralow-loss  $\text{Si}_3\text{N}_4$  waveguides also allowed us to achieve, for the first time, continuous-wave parametric amplification in an integrated waveguide, with a demonstrated gain of 9.5 dB and noise figure of 1.2 dB when operated in phase-sensitive mode.

**Keywords:** silicon nitride, ultralow loss, integrated waveguide, Kerr nonlinear optics, DKS microcombs, parametric amplifiers



# Acknowledgment

First I would like to thank my supervisor, Associate Prof. Victor Torres-Company, without his talented leadership, solid supports and fruitful discussions I would not have made it this far. I also would like to thank my examiner and co-supervisor, Prof. Peter Andrekson for giving me opportunity to pursue the research work in the photonics laboratory and providing a challenging but achievable research goal which motivated me through the past five years.

I would like to thank Dr. Morten Bache and Simon Christensen from DTU for the collaboration. I also thank Prof. Andrew Weiner, Prof. Minghao Qi, Dr Cong Wang and Dr. Mohammed Alshaykh from Purdue university for the collaboration.

I would like to acknowledge all the staffs at the nanofabrication laboratory, without their hard work to keep the cleanroom operational I would not have made such ultralow-loss silicon nitride waveguides. Especially, I would like to thank Dr. Marcus Rommel for teaching me EBL and providing supports for Beamer flows. I also thank Johan Karl Andersson for his best efforts on maintaining LPCVD furnaces operational.

Moreover, I would like to thank all the members in the photonics laboratory at Chalmers for both technical and non-technical supports. I would like to acknowledge Dr. Clemens Krüchel for developing the initial nanofabrication processes and teaching me professional cleanroom skills. Dr. Attila Fülöp deserves acknowledgment for spending so much time teaching me microcomb experiments and help me program equipment. I appreciate Óskar Bjarki Helgason for fruitful discussion about nonlinear optics and endless talk on everything. I have to thank my office mates gratefully. Kovendhan Vijayan and Dr. Ravikiran Kakarla for discussions and playing table tennis, Dr. Xiaonan Hu for being my first Chinese colleague and having discussion both on and beyond research work, Marcello Girardi for creating nice

working environment and making work more enjoyable. I would like to thank Dr. Fuchuan Lei and Dr. Ping Zhao for sharing both enriched knowledge about physics and funny stories about physicists.

I spent so much time in the cleanroom to optimize the processes. I would like to thank Dr. Michael Alexander Bergmann for being my lab buddy, having nice discussions when waiting for processes and showing his nice UV LED devices.

I gratefully appreciate Prof. Yaocheng Shi from Zhejiang university, without his support and encouragement I would not have come to Sweden for both my master program and PhD work. It turns out to be a good decision.

Last but not least, I would like to thank my family and friends for supports. Especially, I appreciate my girlfriend Jingwen Zhang for her support, company and encouragement throughout the years.

Zhichao Ye  
*Gothenburg, March 2021*

# Abbreviations

<b>BSS</b>	Beam step size
<b>CMOS</b>	Complementary metal-oxide-semiconductor
<b>CVD</b>	Chemical vapor deposition
<b>CW</b>	Continuous-wave
<b>DCS</b>	Dichlorosilane
<b>DFB</b>	Distributed feedback
<b>DKS</b>	Dissipative Kerr soliton
<b>DUV</b>	Deep ultraviolet
<b>EBL</b>	Electron beam lithography
<b>FCA</b>	Free carrier absorption
<b>FSR</b>	Free spectral range
<b>FWM</b>	Four-wave mixing
<b>ICP RIE</b>	Inductively-coupled-plasma reactive-ion etching
<b>LPCVD</b>	Low pressure chemical vapor deposition
<b>NF</b>	Noise figure
<b>OFDR</b>	Optical frequency-domain reflectometry
<b>OPA</b>	Optical parametric amplification
<b>PECVD</b>	Plasma-enhanced chemical vapor deposition
<b>PIC</b>	Photonic integrated circuit
<b>RMS</b>	Root mean square
<b>SCG</b>	Supercontinuum generation
<b>SEM</b>	Scanning electron microscopy
<b>SiRN</b>	Silicon-rich silicon nitride
<b>TEOS</b>	Tetraethyl orthosilicate
<b>TPA</b>	Two-photon absorption

**VLSI** Very large scale integration

# List of papers

This thesis is based on the following appended papers:

- [Paper A] **Zhichao Ye**, Attila Fülöp, Óskar Bjarki Helgason, Peter A. Andrekson, and Victor Torres-Company, "Low-loss high-Q silicon-rich silicon nitride microresonators for Kerr nonlinear optics", *Opt. Lett.*, vol. 44, no. 13, pp. 3326-3329 (2019).
- [Paper B] **Zhichao Ye**, Krishna Twayana, Peter A. Andrekson, and Victor Torres-Company, "High-Q  $\text{Si}_3\text{N}_4$  microresonators based on a subtractive processing for Kerr nonlinear optics", *Opt. Express*, vol. 27, no. 24, pp. 35719-35727 (2019).
- [Paper C] Simon Christensen, **Zhichao Ye**, Morten Bache, and Victor Torres-Company, "Octave-spanning frequency comb generation in all-normal-dispersion silicon-rich silicon nitride waveguide", in *Conference on Lasers and Electro-Optics (CLEO)*, San jose, USA, paper. STu3H.7, May 2020.
- [Paper D] **Zhichao Ye**, Ping Zhao, Krishna Twayana, Magnus Karlsson, Victor Torres-Company, and Peter A. Andrekson, "Low-noise continuous-wave-pumped parametric amplifier using a silicon-nitride waveguide", Manuscript submitted, 2021.
- [Paper E] **Zhichao Ye**, Fuchuan Lei, Krishna Twayana, Marcello Girardi, Peter A. Andrekson, and Victor Torres-Company, "Integrated, ultra-compact high-Q silicon nitride microresonators for low-repetition-rate soliton microcombs", Manuscript submitted, 2021.

[Paper F] Mohammed S. Alshaykh, Cong Wang, Nathan P. O'Malley, **Zhichao Ye**, Abdullah Al Noman, Daniel E. Leaird, Minghao Qi, Victor Torres-Company, and Andrew M. Weiner, "Optical Dual-Comb Vernier Division of an Octave-Spanning Kerr Microcomb", To be presented at CLEO 2021.

Related publications and conference contributions by the author:

Journal papers:

- [Paper G] Clemens J. Krücker, Attila Fülöp, **Zhichao Ye**, Peter A. Andrekson, and Victor Torres-Company, "Optical bandgap engineering in nonlinear silicon nitride waveguides," *Opt. Express* 25, 15370-15380 (2017).
- [Paper H] Xiaonan Hu, Marcello Girardi, **Zhichao Ye**, Pascual Muñoz, Anders Larsson, and Victor Torres-Company, "Si<sub>3</sub>N<sub>4</sub> photonic integration platform at 1 μm for optical interconnects," *Opt. Express* 28, 13019-13031 (2020).
- [Paper I] Ping Zhao, **Zhichao Ye**, Kovendhan Vijayan, Corentin Naveau, Jochen Schröder, Magnus Karlsson, and Peter A. Andrekson, "Waveguide tapering for improved parametric amplification in integrated nonlinear Si<sub>3</sub>N<sub>4</sub> waveguides," *Opt. Express* 28, 23467-23477 (2020).
- [Paper J] Óskar B. Helgason, Francisco R. Arteaga-Sierra, **Zhichao Ye**, Krishna Twayana, Peter A. Andrekson, Magnus Karlsson, Jochen Schröder and Victor Torres-Company, "Dissipative solitons in photonic molecules", *Nature Photonics* 2021, <https://doi.org/10.1038/s41566-020-00757-9>.
- [Paper K] Fuchuan Lei, **Zhichao Ye**, Attila Fülöp and Victor Torres-Company, "Fundamental optical linewidth of soliton microcombs", arXiv:2102.05517.

Conference presentations and papers

- [Paper L] Victor Torres-Company, **Zhichao**, Attila Fülöp, Clemens J. Krücker, and Peter A. Andrekson, "High-confinement high-Q silicon-rich silicon nitride nonlinear microresonators," in *Advanced Photonics 2018*, paper ITh2J.2.
- [Paper M] Luis A. Bru, **Zhichao Ye**, Daniel Pastor, Pascual Muñoz, "Multi-parameter estimation of high-Q silicon rich nitride resonators using optical frequency domain reflectometry" *Proc. SPIE*, vol. 10535, pp. 1053518. 2018.

- [Paper N] **Zhichao Ye**, Attila Fülöp, Óskar Bjarki Helgason, Peter A. Andrekson, and Victor Torres-Company, "Low Loss Silicon-Rich Silicon Nitride for Nonlinear Optics," in Conference on Lasers and Electro-Optics (CLEO), San Jose, USA, paper. STu3F.1. May 2018.
- [Paper O] Xiaonan Hu, **Zhichao Ye**, Marcello Girardi, Pascual Muñoz, Anders Larsson, and Victor Torres-Company, "Passive SiN Photonic Integrated Platform at  $1\mu\text{m}$  for Short-Range Optical Interconnects," 2019 Conference on Lasers and Electro-Optics(CLEO) Europe, Munich, Germany, pp. 1-1, June 2019.
- [Paper P] Óskar B. Helgason, **Zhichao Ye**, Krishna Twayana, Peter A. Andrekson, Jochen Schroder and Victor Torres-Company, "Dark-pulse Kerr combs in linearly coupled microring structures," in Conference on Lasers and Electro-Optics (CLEO), San jose, USA, paper. STu3H.5, May 2020.
- [Paper Q] D. Kong, A. A. Jørgensen, M. R. Henriksen, F. Klejs, **Z. Ye**, Ò. B. Helgason, H. E. Hansen, H. Hu, M. Yankov, S. Forchhammer, P. Andrekson, A. Larsson, M. Karlsson, J. Schröder, Y. Sasaki, K. Aikawa, J.W. Thomsen, T. Morioka, M. Galili, V. Torres-Company, and L. K. Oxenløwe, "Single Dark-Pulse Kerr Comb Supporting 1.84 Pbit/s Transmission over 37-Core Fiber," in Conference on Lasers and Electro-Optics (CLEO), San jose, USA, **Post Deadline** paper. JTh4A.7, May 2020.
- [Paper R] **Zhichao Ye**, Fuchuan Lei, Krishna Twayana, Marcello Girardi, Peter A. Andrekson, and Victor Torres-Company, "25 GHz soliton microcombs in high-Q  $\text{Si}_3\text{N}_4$  racetrack-shaped microresonators," in Conference on Lasers and Electro-Optics(CLEO), San jose, USA, paper. JTh2F.29, May 2020.
- [Paper S] **Zhichao Ye**, Krishna Twayana, Peter A. Andrekson, and Victor Torres-Company, "High-Q Dispersion-Engineered  $\text{Si}_3\text{N}_4$  Microresonators Based on a Subtractive Processing Technique," in Conference on Lasers and Electro-Optics(CLEO), San jose, USA, paper. JTh2F.24, May 2020.

# Contents

<b>Abstract</b>	<b>i</b>
<b>Acknowledgment</b>	<b>iii</b>
<b>Abbreviations</b>	<b>v</b>
<b>List of papers</b>	<b>vii</b>
<b>1 Introduction</b>	<b>1</b>
1.1 Historical overview . . . . .	1
1.2 This thesis . . . . .	6
<b>2 Optical waveguide characteristics</b>	<b>9</b>
2.1 Optical confinement . . . . .	9
2.2 Dispersion engineering . . . . .	11
<b>3 Waveguide losses</b>	<b>15</b>
3.1 Origin of waveguide losses . . . . .	15
3.1.1 Bending losses . . . . .	15
3.1.2 Design imperfections . . . . .	16
3.1.3 Mode coupling due to interfacial inhomogeneities . . . . .	19
3.1.4 Material losses . . . . .	24
3.2 Waveguide loss characterization methods . . . . .	25
3.2.1 Cut-back method . . . . .	25
3.2.2 Microring resonator . . . . .	26
3.2.3 Optical frequency-domain reflectometry . . . . .	29

<b>4</b>	<b>Effect of linear losses in Kerr nonlinear optics</b>	<b>31</b>
4.1	Kerr effect . . . . .	31
4.2	Effect of loss on parametric amplifiers . . . . .	33
4.3	Effect of loss on Kerr microcombs . . . . .	37
<b>5</b>	<b>Fabrication techniques of ultra-low-loss silicon nitride waveguides</b>	<b>41</b>
5.1	Overview of fabrication process . . . . .	41
5.2	Silicon nitride thin film deposition . . . . .	43
5.3	Electron beam lithography . . . . .	45
5.3.1	Within a writing field . . . . .	46
5.3.2	Between writing fields . . . . .	48
5.4	Inductively-coupled-plasma reactive-ion etching . . . . .	49
5.5	SiO <sub>2</sub> cladding deposition . . . . .	51
5.6	Analysis of fabrication yield . . . . .	54
<b>6</b>	<b>Summary and future outlook</b>	<b>57</b>
<b>7</b>	<b>Summary of papers</b>	<b>59</b>
	<b>Appendices</b>	<b>63</b>
	<b>Papers A–F</b>	<b>85</b>

# Chapter 1

## Introduction

### 1.1 Historical overview

Before the 18th century, the limited industrial power and transportation engine relied on animal and human muscle, wind and river. Long-haul traveling and communication were limited, and continents were quite isolated. Since the first and second industrial revolution, the unprecedented boost of machine engine enabled fast and convenient traveling between countries and continents, and new ideas spread quickly. Later on, thanks to the invention of telephone and the success of optical fiber communication, people from all over the world became fully connected. The globe turned into a small village.

A similar evolution happened in electrical circuits. The first transistor was invented by J. Bardeen, W. Brattain and W. Shockley at Bell labs, and they shared the 1956 Nobel Prize in Physics for their achievement. The early transistors were large, and long wires were needed to connect different components. For a computer with complex microelectric circuits, these wires can significantly slow the computer. The invention of the integrated circuit by J. Kilby and R. Noyce solved this problem by integrating all the functional components on a single-crystal Si wafer. It is worth mentioning that Jack Kilby also got the Nobel Prize in Physics in 2000 for this achievement. The past 50 years have witnessed a steady development of integrated circuits following Moore's law. It is remarkable that the increasing number of transistors in a densely integrated circuit is encompassed with a significant reduction in computer volume:

from the size of an entire room to a light and portable device.

The techniques that have been developed for the manufacturing of microelectronic circuitry (e.g. lithography, etching, film deposition) can be used to manufacture photonic integrated circuits. PICs have a dominant application in the field of high-bandwidth communications [1], but new applications are continuously emerging that could leverage the ability to mass-produce photonic systems on chip.

## Silicon photonics

Nowadays, there are two major paths for the monolithic integration of PICs: InP and silicon photonics. InP features a direct bandgap and has a relatively large electro-optic (Pockels) coefficient, and thus is suitable for the realization of lasers, photodetectors and modulators. However, photonic integration based on InP is typically more expensive compared with Si photonics due to the scarcity of In, the small size of wafers and the poor native oxide [2]. Moreover, InP is not compatible with CMOS manufacture, thus can't get the benefit from the high-volume low-cost processing in existing CMOS fabrication.

The first optical waveguide in Si was demonstrated in 1986 [3], showing its compatibility with the fabrication environment of Si microelectronic industries. Thanks to its full CMOS-compatibility, photonics integration based on Si photonics features high volume, low cost, high yield and high reproducibility. Although Si lacks the Pockels effect, Si based modulators can be achieved by modifying the charge density by e.g. carrier injection, depletion and accumulation [4]. Regarding waveguide losses, the high index contrast between the Si core and the SiO<sub>2</sub> cladding results in extremely high susceptibility to scattering losses introduced from nanometer-level interfacial inhomogeneities of the sidewalls. Even though substantial efforts from both academia and industry were paid to reduce waveguide loss, high-confinement Si waveguides still display losses in the order of 1 dB/cm [5–7]. Due to the relatively small bandgap (1.1 eV), Si waveguides feature two-photon absorption and free carrier absorption in the near infrared and telecommunication band, which limit the launched optical power. The main challenge of Si photonics is the lack of a native laser due to the indirect bandgap of Si. In spite of tremendous efforts, a Si-based laser source as efficient as a III-V based laser remains elusive [8, 9].

### Expanding the library of building blocks in Si photonics

Due to the lack of a native laser on Si, it's clear that heterogeneous integration is needed to complement the building blocks in Si photonics [10]. Regarding the building blocks of lasers and optical amplifiers, substantial efforts are being paid on bonding III-V material on a Si wafer [11–15]. In fact, narrow-linewidth efficient electrically pumped laser has recently been achieved through III-V/Si/Si<sub>3</sub>N<sub>4</sub> heterogeneous integration [16]. Optical modulator is one of the key components for high speed optical transmitters. Recently in 2018, thanks to the breakthrough of LiNbO<sub>3</sub> nanofabrication technique [17], modulators simultaneously featuring CMOS-compatible V<sub>π</sub>, low phase-shifter loss and large bandwidth (80 GHz) were achieved in LiNbO<sub>3</sub> platform [18]. Moreover, high-performance modulator was also achieved through heterogeneous integration of LiNbO<sub>3</sub> and Si [19]. Ultralow-loss waveguides, being the most fundamental component of photonic integration, find their applications in phase shifters, delay lines and ultrahigh-Q microresonators. Ultralow-loss waveguides are realized using a dielectric material with lower refractive index than silicon as core. The lowest loss have been recently reported using Si<sub>3</sub>N<sub>4</sub> in a low-confinement geometry [20]. Additionally, a low-linewidth III-V DFB laser (1.2 Hz) has been achieved through injection locking to a ultrahigh-Q (220 million) Si<sub>3</sub>N<sub>4</sub> microresonator [21]. In order to bridging above mentioned platforms, 3D integration with low loss is needed. Recent demonstration in [22] proved that less than 0.15 dB interlayer (silicon to silicon nitride) taper transition loss can be achieved for broad wavelength range from 1480 nm to 1620 nm.

### The race to ultralow-loss high-confinement Si<sub>3</sub>N<sub>4</sub> waveguides

Apart from Si, integrated waveguides based on numerous materials, including Hydex, Si<sub>3</sub>N<sub>4</sub>, Ta<sub>2</sub>O<sub>5</sub>, AlN, chalcogenide and AlGaAs [23–32], have been widely investigated in the past decades. Among these materials, Si<sub>3</sub>N<sub>4</sub> is one of the most outstanding materials. Its CMOS-compatibility allows for high-volume and low-cost fabrication. High quality Si<sub>3</sub>N<sub>4</sub> films (with estimated material loss <0.03 dB/m in [33]) can be acquired from LPCVD, where a massive number of wafers can be loaded simultaneously into the furnace. The transparency window of Si<sub>3</sub>N<sub>4</sub> ranges from ultraviolet (UV) wavelength to 5 μm, thus making it suitable for broadband applications. The large bandgap indicates that nonlinear losses are negligible in the

near-infrared. Its modest refractive index simultaneously allows high confinement and relaxes the requirements in nanofabrication in order to attain ultralow propagation loss. The modest Kerr nonlinearity of  $\text{Si}_3\text{N}_4$  makes it suitable for nonlinear optics.

In fact, ultralow-loss  $\text{Si}_3\text{N}_4$  waveguides with propagation losses down to 0.045 dB/m were achieved as early as 2011 [34]. In this work, a low confinement geometry was adopted to significantly reduce the susceptibility to scattering losses induced from sidewall roughness. However, these waveguides require bending radii larger than 5 mm to cope undesired bending loss. The required large bending radii dramatically increase the footprint of photonic integration. Moreover, due to the large effective area of the mode, the nonlinear parameter of the waveguides is quite small and the dispersion cannot be engineered to be anomalous, making it an impractical geometry for many applications in nonlinear optics. Nevertheless, ultralow-loss low-confinement waveguides found their applications in ultralow-loss delay lines [35], and, strictly speaking, the low loss is used to fabricate external cavities for low linewidth lasers [21].

For nonlinear optics, high-confinement  $\text{Si}_3\text{N}_4$  waveguides with small effective area are needed to achieve high optical intensity. Compared with low confinement waveguides, the tightly confined  $\text{Si}_3\text{N}_4$  waveguides become extremely susceptible to the scattering losses introduced from nanometer level interfacial inhomogeneities of the waveguides [36]. This issue must be overcome by advanced nano-fabrication techniques.

One critical outstanding issue towards achieving high-confinement  $\text{Si}_3\text{N}_4$  waveguides starts already with the deposition of thick films. Before 2009, the height of  $\text{Si}_3\text{N}_4$  waveguides was limited below 300 nm due to the crack formation originated from the tensile stress of thick  $\text{Si}_3\text{N}_4$  film [37]. In 2009, Gondarenko et al. implemented a thermal cycling process to successfully deposit  $\text{Si}_3\text{N}_4$  film with thickness up to 744 nm [38]. The achieved thickness allowed to engineer the dispersion of the waveguide to be anomalous in the near-infrared. In the same year, microresonator frequency comb generation [39] was achieved in a  $\text{Si}_3\text{N}_4$  microring for the first time [25]. This was a hallmark in the field and sparked an ever growing interest towards the realization of chip-scale frequency combs using silicon photonics technology. Later on, in 2013, Luke et al. combined both thermal cycling and mechanical trenches [40] to achieve crack-free  $\text{Si}_3\text{N}_4$  films with thickness up to 910 nm [41]. Besides implementing thermal cycling and mechanical trenches to obtain crack-free thick  $\text{Si}_3\text{N}_4$  films, Epping et al. introduced an alternative process, consist-

## 1.1. Historical overview

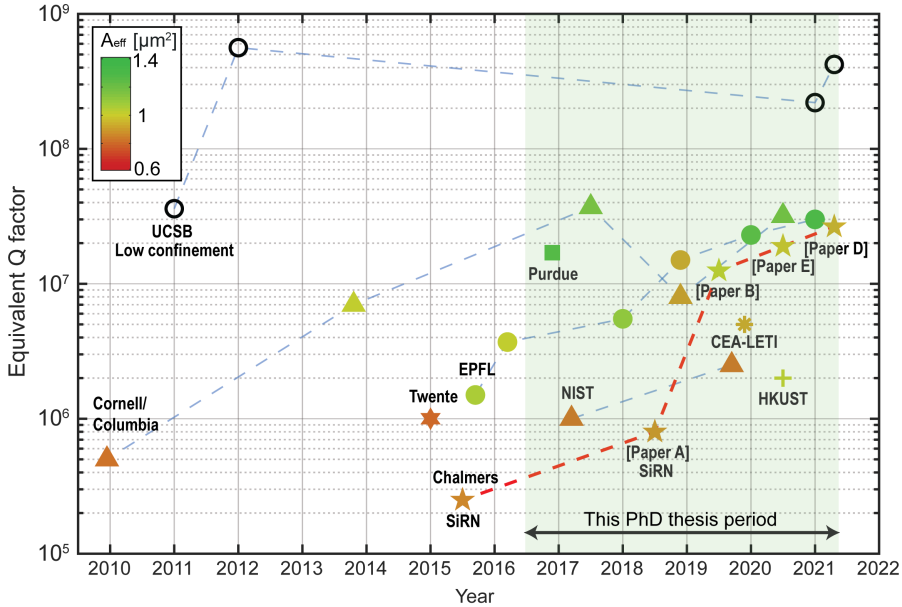


**Figure 1.1:** The progress of Q factors of  $\text{Si}_3\text{N}_4$  microresonators and equivalent Q factors of  $\text{Si}_3\text{N}_4$  spiral waveguides since 2010. Results from several groups, including UCSB [20, 21, 34, 47], Columbia university [25, 41, 48–50], EPFL [33, 43, 51–54], Purdue university [55], Chalmers university of technology [56][Paper B, D, E], NIST [57, 58], University of Twente [42], HKUST [59] and CEA-LETI [60] are presented

ing on depositing a  $\text{Si}_3\text{N}_4$  film on a preformed  $\text{SiO}_2$  substrate, followed by a chemical mechanical polishing step [42].  $\text{Si}_3\text{N}_4$  waveguides 900 nm thick and without cracks were successfully generated. This process was further optimized in the so-called Damascene process by Marin et al [43]. The progress of increased film thickness enabled the flexibility of dispersion engineering. As a consequence, octave-spanning dissipative Kerr soliton (DKS) microcombs, which enable  $f$ - $2f$  self-referencing, were achieved in  $\text{Si}_3\text{N}_4$  microrings [44, 45]. Dispersive wave engineered supercontinuum generation (SCG) with an overall bandwidth spanning up to three octaves was also realized in a  $\text{Si}_3\text{N}_4$  waveguide [46].

Besides the firmly increased  $\text{Si}_3\text{N}_4$  film thickness, the race of attaining ultralow-

loss  $\text{Si}_3\text{N}_4$  started simultaneously. The progress of equivalent Q factors of high-confinement  $\text{Si}_3\text{N}_4$  microring resonators and spiral waveguides is shown in Fig. 1.1, including the results from Columbia university [25, 41, 48–50], EPFL [33, 43, 51–54], Purdue university [55], Chalmers university of technology [56][Paper B, D, E], NIST [57, 58], university of Twente [42], HKUST [59] and CEA-LETI [60]. The colors of the markers indicate the effective area of the waveguides, and small effective area enabling large nonlinear parameter is desired for nonlinear optics. As can be seen in Fig. 1.1, Columbia group (originally from Cornell university) is the pioneer using  $\text{Si}_3\text{N}_4$  waveguides for nonlinear optics, and steadily pushed Q factors to  $31 \times 10^6$  using a subtractive processing method. The achieved high-Q  $\text{Si}_3\text{N}_4$  waveguides feature a relatively large effective area ( $\sim 1.25 \mu\text{m}^2$ ) due to increased waveguide width. EPFL fabricated  $\text{Si}_3\text{N}_4$  waveguides using photonics damascene process, and firmly improved the Q factors to  $30 \times 10^6$ . The waveguide geometry also features a relatively large effective area ( $\sim 1.37 \mu\text{m}^2$ ) due to a relatively large core height. We started to work on silicon nitride relatively late, and focused the efforts on SiRN because it can be directly deposited without crack formation [61], thus easing the need to fabricate trenches for stress release. Substantial efforts were paid on SiRN since 2015, but Q factors were limited below  $1 \times 10^6$ . More recently, we shifted the interest towards  $\text{Si}_3\text{N}_4$ . Thanks to significantly improved fabrication techniques, we obtained waveguides with losses of 1.4 dB/m (equivalent Q factor of  $26 \times 10^6$ ).

The decrease in losses of high-confinement silicon nitride waveguides has enabled multiple applications in nonlinear optics. The first DKS microcomb in  $\text{Si}_3\text{N}_4$  was achieved in 2016, allowing subsequently realization of high-speed coherent optical communications [62–64], optical frequency synthesis [65], light detection and ranging [66, 67], microwave generation [54] and spectroscopy [68]. More recently, DKS microcombs have been co-integrated with lasers [49], and turnkey soliton microcombs were demonstrated [69]. Apart from microresonators, the low-loss and broad transparency can also be capitalized in a straight waveguide geometry for e.g. super-continuum generation [46] and dual-comb spectroscopy [70].

## 1.2 This thesis

This thesis focuses on the realization of ultralow-loss high-confinement silicon nitride waveguides and corresponding applications in nonlinear optics. In order to

achieve high yield fabrication, we started with SiRN with an optimized stoichiometry, i.e., the minimum gas ratio between  $\text{SiH}_2\text{Cl}_2$  and  $\text{NH}_3$  to achieve crack-free SiRN film with thickness  $\sim 700\text{nm}$ , which is needed for dispersion engineering. High  $Q \sim 0.8 \times 10^6$  microresonators and low noise microcombs were achieved in this platform [Paper A]. Later on, low-noise octave-spanning SCG was obtained in an all-normal dispersion waveguide [Paper C]. It's the first octave-spanning supercontinuum generation in an all-normal-dispersion nanophotonic waveguide.

Even though substantial efforts were further paid to optimize material growth, EBL and dry etching,  $Q$  factors of SiRN microrings were limited below  $1 \times 10^6$ . We suspected that the  $Q$  factors were limited by scattering losses and absorption losses in the films, and decided to move toward silicon nitride in its stoichiometric form. Using a similar etching recipe, the  $Q$  factor increased dramatically to  $11 \times 10^6$ , and both dark and bright soliton microcombs with 100 GHz [71] as well as octave-spanning bright soliton microcombs [Paper F] were achieved. With a further optimized process and design, DKS microcomb with repetition rate down to 14 GHz was achieved for the first time in a compact ( $< 1\text{mm}^2$  footprint) snail-shaped microresonator with statistical  $Q$ s of  $19 \times 10^6$  [Paper E].

With respect to long spiral waveguides, we overcame the challenges of EBL and required high yield for long waveguides. A CW-pumped OPA was firstly realized in an integrated Kerr nonlinear waveguide [Paper D].

### **Thesis outline**

Chapter 2 introduces the basic characteristics of optical waveguides, and emphasizes the requirements for precise dispersion engineering. In chapter 3, some of the most prominent sources of losses are discussed, including bending loss, design imperfections, interfacial inhomogeneities and material loss, are discussed. The pros and cons of three different characterization methods for waveguide losses used in this thesis work are also provided. Chapter 4 shows why ultralow-loss  $\text{Si}_3\text{N}_4$  waveguides are important for high performance parametric amplifiers and DKS microcombs. Chapter 5 presents the overview of the fabrication flow of ultralow-loss silicon nitride waveguides. The photonics yield parameter is discussed, and few key fabrication steps which significantly contribute to ultralow-loss waveguide are described in detail. In the end, chapter 6 provides a summary and future outlook.



## Chapter 2

# Optical waveguide characteristics

In contrast to traditional optical fibers, integrated waveguides can highly confine light in a sub- $\mu\text{m}^2$  area thanks to the large index contrast between the core and cladding materials. The optical confinement and dispersion can be dramatically modified by precisely engineering the width and height of the core. This chapter introduces the concepts of optical confinement and dispersion engineering.

### 2.1 Optical confinement

Typically, an optical waveguide needs a core with refractive index larger than its surrounding cladding layers. The optical guiding in a waveguide can be understood by total internal reflection at the interface between the core and cladding materials. The precise mode field of a waveguide can be solved from Maxwell's equations. In integrated platforms, the commonly used waveguide geometries include slab waveguides, rib waveguides and strip waveguides. An analytical solution of the mode field can be acquired for slab waveguides, while numerical simulations are needed for rib waveguides and strip waveguides. The waveguides used in this thesis are strip waveguides. Nowadays, the mode field of a waveguide can be simulated by commercially available softwares, e.g., COMSOL Multiphysics. It uses finite element methods to

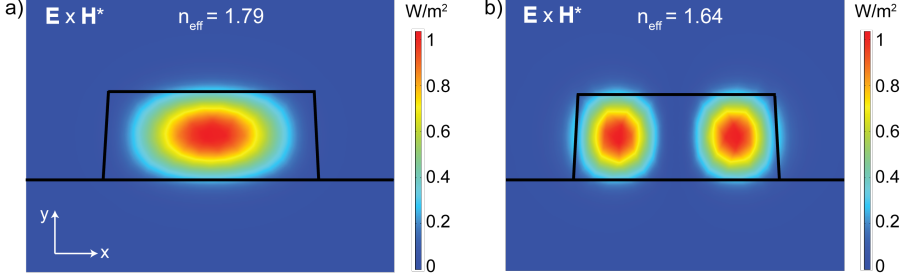


**Figure 2.1:** Simulation results of a  $\text{Si}_3\text{N}_4$  waveguide with height 660 nm and width 1600 nm based on COMSOL. The sidewall angle of the waveguide is  $87^\circ$ . The modes profiles of the Poynting vector in  $z$  direction for fundamental TE mode (a) and second-order TE mode (b) are presented.

solve the modified Helmholtz equation. The FEM solver outputs the eigenvectors (modes) and corresponding eigenvalues (propagation constant of the modes). The propagation constant  $\beta$  accounts for the phase delay accumulated per unit length for light of a certain wavelength propagating along the direction of invariance symmetry. From the propagation constant, the effective index ( $n_{\text{eff}}$ ) of the mode can be defined as

$$n_{\text{eff}} = \frac{\beta}{k_0}, \quad (2.1)$$

where  $k_0$  is the wavenumber in vacuum,  $k_0 = 2\pi/\lambda_0$ .  $\lambda_0$  is the wavelength in vacuum. An example of the simulated mode field of a waveguide ( $\text{Si}_3\text{N}_4$  core and  $\text{SiO}_2$  cladding) with height 660 nm and width 1600 nm at the wavelength of 1550 nm is shown in Fig. 2.1. For TE polarization, the waveguide supports two transverse modes, i.e., fundamental TE mode and second-order TE mode. The effective index is 1.79 for fundamental TE mode, and is 1.64 for second-order TE mode.

The effective area,  $A_{\text{eff}}$ , is introduced in order to quantitatively evaluate the area that the mode of a waveguide effectively covers in the transverse dimension, and has expression as [72]

$$A_{\text{eff}} = \frac{|\int \vec{E} \times \vec{H}^* \cdot \hat{z} dA|^2}{\int |\vec{E} \times \vec{H}^* \cdot \hat{z}|^2 dA}, \quad (2.2)$$

where  $\vec{E}$  and  $\vec{H}$  are electric field and magnetic field, respectively. The integral should be taken over the entire cross section. The effective area of a waveguide can be dramatically modified by engineering the waveguide geometry. The mode profile

## 2.2. Dispersion engineering

---

of a  $\text{Si}_3\text{N}_4$  waveguide ( $660\text{nm} \times 1600\text{nm}$ ) has an  $A_{\text{eff}}$  less than  $1 \mu\text{m}^2$  whereas a  $\text{Si}_3\text{N}_4$  waveguide with core cross-section dimension  $150\text{nm} \times 1000\text{nm}$  results in an  $A_{\text{eff}}$  larger than  $5 \mu\text{m}^2$ , see Fig. 2.2a and b. The effective area of the fundamental TE mode with respect to different waveguide geometries is shown in Fig. 2.2c.

A waveguide with small effective area indicates high optical intensity can be achieved with reasonable optical power assuming the light source can efficiently excite the corresponding mode, which is essential for nonlinear optics. The smallest effective area for a  $\text{Si}_3\text{N}_4$  waveguide is  $0.75 \mu\text{m}^2$  and is achieved by a height of 500 nm and a width of 1000 nm. However, it features normal dispersion (described in next section). In order to achieve anomalous dispersion, the  $\text{Si}_3\text{N}_4$  waveguides need to be thick and wide enough, as illustrated in Fig. 2.2c. Strip  $\text{Si}_3\text{N}_4$  waveguides designed to attain anomalous dispersion in the telecommunication region are multimode.

Moreover, a waveguide with small effective area also dictates the possibility to achieve small bending radius, which is beneficial for dense photonic integration. While a small effective area is beneficial for nonlinear optics and compact integration, a waveguide with large effective area is commonly used to match the optical mode field between a waveguide and an optical fiber to reduce coupling losses [73]. Moreover, typically, weakly confined waveguides have much lower propagation losses than high confinement waveguides, and find their applications in ultralow-loss delay lines [35] and ultra-narrow linewidth lasers [74, 75].

## 2.2 Dispersion engineering

The propagation constant is in reality wavelength (frequency) dependent, and can be expanded in Taylor series. The Taylor expansion of  $\beta$  around an angular frequency  $\omega_0$  is

$$\beta(\omega) = \beta_0(\omega_0) + \beta_1(\omega - \omega_0) + \sum_{n=2}^{\infty} \frac{\beta_n}{n!} (\omega - \omega_0)^n, \quad (2.3)$$

where  $\beta_1$  is related to the group velocity by  $v_g = 1/\beta_1$ .  $\beta_n$  is  $n^{\text{th}}$ -order dispersion at angular frequency  $\omega_0$

$$\beta_n = \frac{d^n \beta}{d\omega^n}, \quad (2.4)$$

Here,  $\beta_2$  (group velocity dispersion parameter, and it's later referred to dispersion.) describes the pulse broadening along propagation. A waveguide has normal dispersion when  $\beta_2 > 0$ , while has anomalous dispersion when  $\beta_2 < 0$ . The dispersion

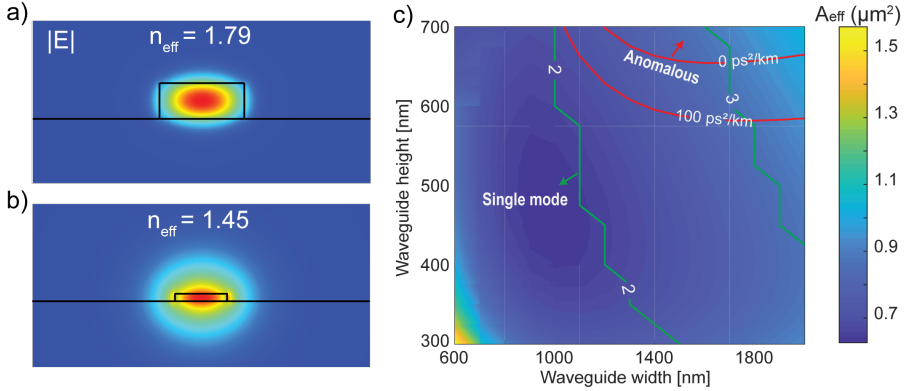


**Figure 2.2:** Mode profiles of fundamental TE mode of  $\text{Si}_3\text{N}_4$  waveguides with geometries  $660\text{nm} \times 1600\text{nm}$  (a) and  $150\text{nm} \times 1000\text{nm}$  (b). (c) Effective area of fundamental TE mode of the waveguides with different geometries. The green contour lines show the number of modes that the waveguide supports in TE polarization. The red contour lines show the dispersion of the fundamental TE mode of the waveguides at the wavelength  $1550\text{ nm}$ .

of the modes has two contributions, from the material and the waveguide geometry. The material dispersion of  $\text{Si}_3\text{N}_4$  and SiRN (used in [Paper A]) is shown in Fig. 2.3a. Due to the absorption resonance at the ultraviolet wavelength, the material dispersion is normal at short wavelengths ( $< 1650\text{ nm}$ ). The dispersion originated from the confinement of a waveguide can be simulated by setting the refractive indices of core and cladding material constant at all frequencies. Here, the refractive indices of  $\text{Si}_3\text{N}_4$ , SiRN (used in [Paper A]) and  $\text{SiO}_2$  are set to 1.99, 2.07 and 1.443, respectively. The simulation results can be seen in Fig. 2.3b. The dispersion originated from the confinement of a waveguide is anomalous at short wavelengths and normal at long wavelengths, i.e., opposite to the material dispersion. The SiRN waveguide features stronger anomalous dispersion than  $\text{Si}_3\text{N}_4$ , due to its higher index contrast to the cladding layer. By properly selecting waveguide materials and geometries, a variety of dispersion profiles can be acquired. It needs to be pointed out that the overall dispersion of a waveguide can't be simply calculated by adding material dispersion to the dispersion originated from the confinement of a waveguide. The simulations of the waveguide modes should be carried out considering the frequency dependent refractive index of both core and cladding materials.

## 2.2. Dispersion engineering

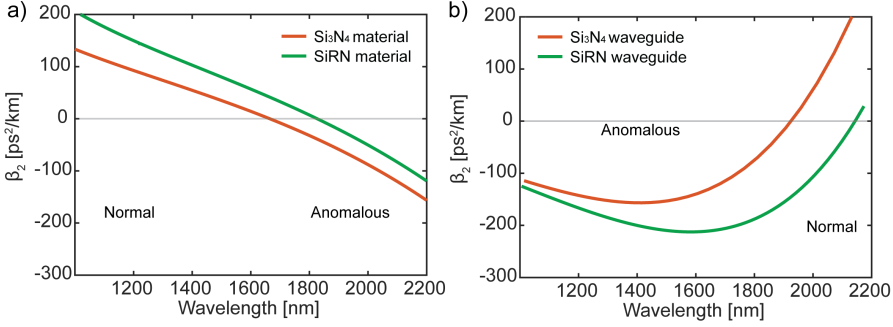


**Figure 2.3:** a) Dispersion of bulk Si<sub>3</sub>N<sub>4</sub> and SiRN materials. b) Dispersion originated from the confinement of Si<sub>3</sub>N<sub>4</sub> and SiRN waveguides. The waveguide geometry is 800 nm × 1600 nm.

It's worthwhile to see how sensitive the waveguide dispersion is to small variations of the waveguide geometry or the refractive indices of the materials. Fig. 2.4a shows the dispersion of the fundamental TE mode of a Si<sub>3</sub>N<sub>4</sub> waveguide (660 nm × 1600 nm) and two waveguides with slightly modified height (+ 10nm) and width (+ 100nm). As can be seen, with 100 nm difference of waveguide width, the slope of  $\beta_2$  is slightly changed, i.e.,  $\beta_3$  is changed. With an increased height of 10 nm, the waveguide dispersion is down shifted by  $\sim 10$  ps<sup>2</sup>/km. In practice, although the waveguide width can be precisely controlled by lithography with an accuracy < 10 nm, it's difficult to avoid  $\sim 2\%$  variation of waveguide height across a wafer due to LPCVD Si<sub>3</sub>N<sub>4</sub> deposition (see section 5.2). Additional to the variations of waveguide geometries, the dispersion changes due to small variations of material refractive index are shown in Fig. 2.4b. Here, the refractive index of Si<sub>3</sub>N<sub>4</sub> is offset by  $\pm 0.005$  on purpose. It's obvious that, by offsetting the refractive index by  $\pm 0.005$ , the waveguide dispersion is up/down shifted by  $\sim 7$  ps<sup>2</sup>/km. Note, only refractive index offset is considered here, and more dispersion variation can be observed if the wavelength dependent refractive index is taken into account. This indicates that the refractive index of the materials should be precisely measured prior to the fabrication of waveguides. The above analysis conveys that the variation of dispersion should be carefully taken into account when precise dispersion engineering is needed, e.g., for dispersive wave engineering [76] and octave-spanning DKS microcomb [45, 65, 77].

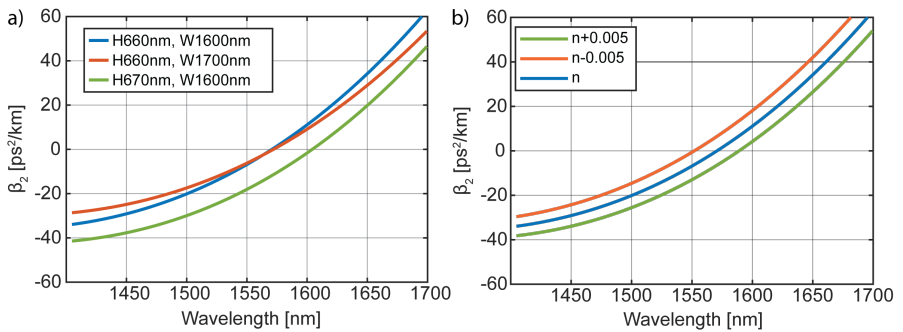


**Figure 2.4:** Sensitivity of group velocity dispersion parameter to waveguide parameters. (a) Si<sub>3</sub>N<sub>4</sub> waveguides with small variations of height or width. (b) Waveguides with small variations of the refractive index of the core material.

## Chapter 3

# Waveguide losses

The optical waveguide is the most fundamental element of any photonic integrated component. Undesired waveguide losses can result in significant power attenuation and crosstalk, thus undermining the possibility to create complex PICs. Waveguide losses include scattering losses and absorptive losses. This chapter introduces the origins of waveguide losses including design imperfections, bending losses, waveguide imperfections and material losses. The characterization methods for waveguide loss used in this Thesis are also introduced.

### 3.1 Origin of waveguide losses

#### 3.1.1 Bending losses

In complex PICs, it's unavoidable to introduce bent waveguides to modify the propagation direction of the light. When a waveguide is dramatically bent, the phase front of the optical mode at the outside of the bend needs to travel faster than the inner side of the bend, and couples to radiation modes when it tends to travel faster than the speed of light in the cladding layer [78]. Therefore, bending loss should be taken into account for bent waveguides. Typically, the bending radius of a waveguide should be maintained large enough so that the bending loss is negligible compared with waveguide losses introduced from fabrication imperfections. This bending radius is referred to as minimum bending radius. The minimum bending radius is related to

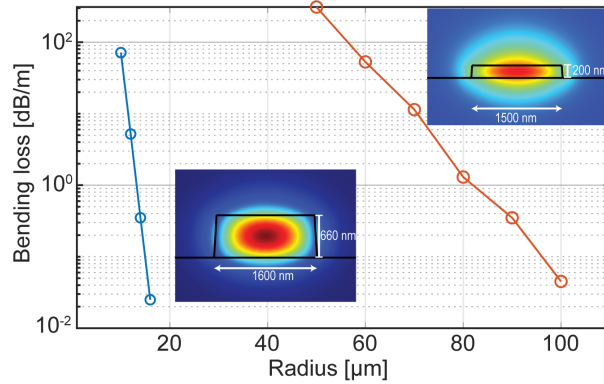


**Figure 3.1:** Simulated bending loss of a  $\text{Si}_3\text{N}_4$  waveguide with  $A_{\text{eff}}=0.85 \mu\text{m}^2$  (blue circles), and a  $\text{Si}_3\text{N}_4$  waveguide with  $A_{\text{eff}}=2.39 \mu\text{m}^2$  (orange circles).

the effective area of the waveguide mode. The simulated bending losses of a  $\text{Si}_3\text{N}_4$  waveguide ( $660 \text{ nm} \times 1600 \text{ nm}$ ) with  $A_{\text{eff}}=0.85 \mu\text{m}^2$  and a  $\text{Si}_3\text{N}_4$  waveguide ( $200 \text{ nm} \times 1500 \text{ nm}$ ) with  $A_{\text{eff}}=2.39 \mu\text{m}^2$  at wavelength of  $1550 \text{ nm}$  are shown in Fig. 3.1. Both results are based on the fundamental TE mode of the waveguides. A minimum bending radius of  $16 \mu\text{m}$  is sufficient for the high confinement  $\text{Si}_3\text{N}_4$  waveguide in order to achieve bending loss less than  $0.1 \text{ dB/m}$ . Such small bending radii are critical for DKS microcombs with repetition rates of  $\sim 1 \text{ THz}$ , which are described in [Paper B, F]. However, a minimum bending radius of  $100 \mu\text{m}$  is needed for the low confinement  $\text{Si}_3\text{N}_4$  waveguide to achieve bending loss less than  $0.1 \text{ dB/m}$ . Due to the increased minimum bending radii, low confinement waveguides significantly increase the footprint of PICs.

### 3.1.2 Design imperfections

Design imperfections include (but not limited to) the improper design of both GDSII files and curves used to connect different bends.

#### Squaring the circles

GDSII files containing the patterns of waveguides are used to guide EBL for waveguide fabrication. If a GDSII file with a coarse grid is used, the waveguide patterns can be significantly distorted. The distorted patterns can be translated into the fabricated waveguides through EBL and, consequently, introduce scattering losses. Apart from the required fine grid for GDSII files, sufficient polygons should be used for the patterns of bent waveguides so that the aliasing resulting from a finite number of polygons is much smaller than the waveguide roughness introduced during nanofabrication [79]. A guideline for the required number of polygons for creating a circle is

$$R - \sqrt{R^2 - \left(\frac{2\pi R}{2N}\right)^2} \ll \sigma, \quad (3.1)$$

where  $R$  is the radius of a circle,  $\sigma$  is the RMS roughness of the fabricated waveguides and  $N$  is the number of polygons for a circle. In this thesis work, 4000 polygons are used for a circle with radius of  $220 \mu\text{m}$ . This means the aliasing resulting from squaring the circle is  $0.06 \text{ nm}$ , which is much smaller than the RMS roughness ( $1 \text{ nm}$ ) reported in [Paper B]. Although squaring the circles can be a severe imperfection in EBL, this problem is less significant in DUV stepper lithography due to the demagnification factor.

#### Matching modes in bends

In PICs, bent waveguides are commonly used for  $90^\circ/180^\circ$  turns and connections between clockwise and counter-clockwise spiral waveguides. The mode mismatch between waveguides with different curvatures can significantly introduce radiation loss and coupling between different transverse modes. Therefore, Euler bend [80] and modified versions [81, 82] were proposed to keep the curvature of the waveguide continuous along propagation. Even though the solutions based on Euler bends work well for connections between straight waveguides, it's difficult to apply them on two arbitrary bends as the solution is based on the symmetry of the structure. In fact, a more general design algorithm was proposed earlier in [83] to minimize the variation of the curvature [84], which in turn minimizes the coupling from the fundamental mode to other transverse modes [83]. The proposed solution to the problem

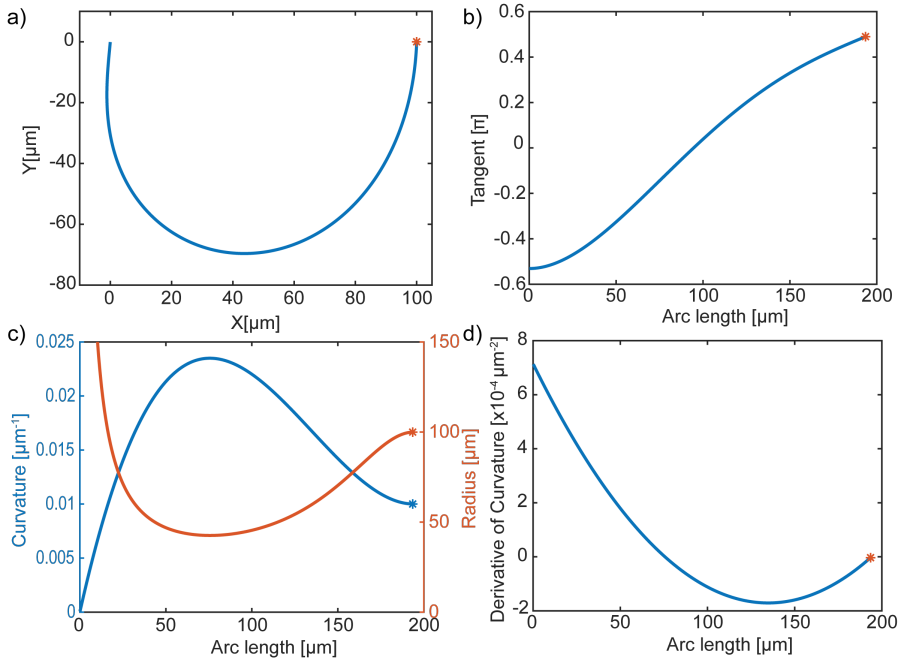


**Figure 3.2:** The physical position, the tangent, the curvature and the change of the curvature with respect to the arc length  $s$  are presented in (a), (b), (c) and (d), respectively. The bend is used to connect the clockwise and counter-clockwise Archimedean spirals.

### 3.1. Origin of waveguide losses

---

of minimization of the variation of the curvature is [85]

$$\kappa(s) = a_0 + a_1s + a_2s^2 + a_3s^3, \quad (3.2)$$

where  $\kappa$  (with unit  $\mu\text{m}^{-1}$ ) is the curvature with respect to arc length  $s$  from the start point of the bend. Coefficients  $a_0, a_1, a_2, a_3$  need to be solved using the physical position, the tangent of the bend, the curvature and the change of the curvature at the start and end points as boundary conditions. The physical position, the tangent, the curvature and the change of the curvature at the end of the curve are

$$x_1 = \text{Re}\left\{\int_0^{s_1} \exp[i\theta(s)]ds\right\}, \quad (3.3)$$

$$y_1 = \text{Im}\left\{\int_0^{s_1} \exp[i\theta(s)]ds\right\}, \quad (3.4)$$

$$\theta_1 = \theta_0 + \int_0^{s_1} a_0 + a_1s + a_2s^2 + a_3s^3 ds, \quad (3.5)$$

$$\kappa_1 = a_0 + a_1s_1 + a_2s_1^2 + a_3s_1^3, \quad (3.6)$$

$$\kappa'_1 = \left.\frac{d\kappa(s)}{ds}\right|_{s=s_1}, \quad (3.7)$$

where  $\theta_0$  is the tangent of the bend at the start point. Here, Eqs. 3.3 and 3.4 do not have analytical solutions. The equations can be solved numerically as described in appendix-A. This bend design was used in [Paper D, E] to minimize the coupling between different transverse modes. To exemplify this bend, the physical position, tangent of the bend, the curvature and the change of the curvature of the bend are shown in Fig. 3.2. The bend is used to connect the clockwise and counter-clockwise Archimedean spirals ( $r=R+A\phi$ , where  $R=100 \mu\text{m}$  and  $A=10/\pi$ ). The star symbols in Fig. 3.2 indicate the corresponding values at the start point of the Archimedean spiral, which should match that of the end point of the bend. Optical microscopy images of a fabricated Archimedean spiral waveguide and a snail-shaped microresonator are shown in Fig. 3.3.

#### 3.1.3 Mode coupling due to interfacial inhomogeneities

The interfacial inhomogeneities of a waveguide typically include surface roughness and sidewall roughness. Surface roughness mainly comes from material deposition, while sidewall roughness is mainly introduced during lithography and dry etching,

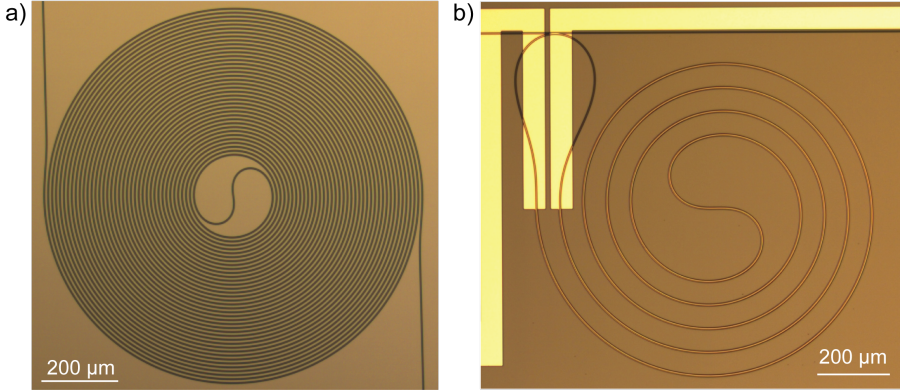


**Figure 3.3:** Optical microscopy images of an Archimedean spiral waveguide (a) and a snail-shaped microresonator (b)

see more details in Chapter 5. The interfacial inhomogeneities of the waveguide introduce a dielectric perturbation, which breaks the orthogonality relation between the modes, thus allowing coupling from the intended guiding mode to other modes including different transverse modes and radiation modes [78]. The coupling only happens in the perturbation regime, and the coupling constant is determined by the overlap of the coupled modes.

Although similar interfacial inhomogeneities can be achieved in waveguides with different geometries and refractive index contrast, their impact on the scattering losses can be different. In order to qualitatively evaluate how sensitive the different waveguide geometries are to the scattering loss induced from interfacial inhomogeneities, we can simply evaluate the propagation loss by [36]

$$\alpha_r \approx A \left[ \frac{\partial n_{\text{eff}}}{\partial w} + \frac{\partial n_{\text{eff}}}{\partial h} \right], \quad (3.8)$$

where  $w$  and  $h$  is the width and height of the waveguides, respectively.  $A$  is a scaling factor which takes into account both the RMS roughness and correlation length of interfacial inhomogeneities, while  $A$  is independent on the waveguide geometry. This equation can be understood by the 'sensitivity' of the effective index of the mode to the variations of width and height produced by the sidewall roughness and surface roughness, respectively. Since the sidewall roughness and surface roughness of the waveguide typically differs significantly from each other, we calculate  $\partial n_{\text{eff}}/\partial w$  and

### 3.1. Origin of waveguide losses

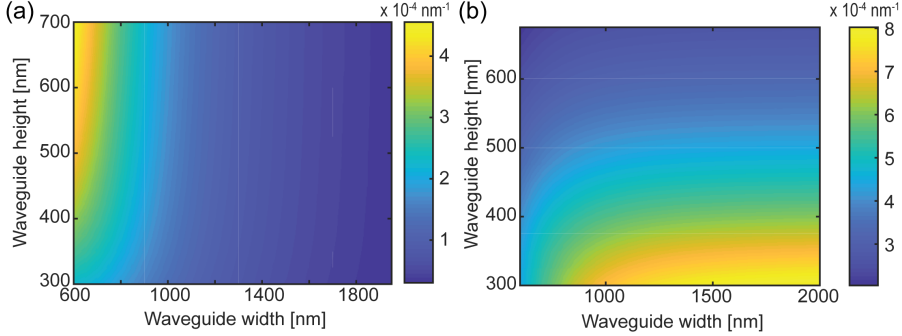


**Figure 3.4:** The fundamental TE mode of (a)  $\partial n_{\text{eff}}/\partial w$  and (b)  $\partial n_{\text{eff}}/\partial h$  with respect to different waveguide geometry.

$\partial n_{\text{eff}}/\partial h$  separately. Fig. 3.4a and b illustrates the variation of the effective index of the mode with the waveguide geometry for  $\text{Si}_3\text{N}_4$  waveguides at the wavelength 1550 nm. Since  $\partial n_{\text{eff}}/\partial w$  represents the 'sensitivity' to sidewall roughness, Fig. 3.4a indicates that thin and wide waveguides are less sensitive to the scattering loss induced from sidewall roughness. However, this type of waveguides are unsuitable for nonlinear optics based on the analysis in Chapter 2. In fact, we need sufficient thick waveguides in order to achieve anomalous dispersion, and to be relatively narrow to maintain small effective area. Hence the waveguide with this type of design is very susceptible to the sidewall roughness. It's clear that advanced nanofabrication techniques are required to attain  $\text{Si}_3\text{N}_4$  waveguides with sidewalls as smooth as possible. Fig. 3.4b indicates that thicker waveguides are less sensitive to surface roughness, and this is in line with the requirement of  $\text{Si}_3\text{N}_4$  waveguide designs for nonlinear optics.

In order to accurately and quantitatively model the waveguide radiation loss due to sidewall roughness, three-dimensional models of waveguide scattering loss are needed [86, 87]. In [86], the model is based on the volume current method, where variations of dielectric constant on waveguide sidewalls are considered as equivalent current densities. In [87], radiated light due to waveguide roughness is considered to be coupled to radiation modes. Both [86] and [87] constructed three-dimensional radiation modes taking the high refractive index of the core material into account. However, unfortunately, these two references draw conclusions that are opposite to each other. Ref [87] concludes that 2D model [88] underestimate the waveguide loss

compared with 3D model, while [86] concludes the opposite.

Notwithstanding, according to the models from both [86–88], waveguide scattering loss is linearly proportional to squared RMS roughness  $\sigma^2$ , indicating that ultra-smooth surfaces are required to reach ultralow-loss scattering losses in high confinement waveguides. At the start point of this thesis work, the RMS roughness of waveguide sidewalls was  $\sim 5$  nm [56]. But, at the late stage of this PhD, this value has been reduce to less than 1 nm [Paper B]. This corresponds to more than 25 times reduction of scattering loss due to sidewall roughness. The SEM images showing the evolution of the fabricated  $\text{Si}_3\text{N}_4$  waveguides are shown in Chapter 5, Fig. 5.5. The RMS roughness of the top and bottom surfaces of the waveguides is  $\sim 0.5$  nm for SiRN [56][Paper A], while it's less than 0.2 nm for  $\text{Si}_3\text{N}_4$  waveguides. This corresponds to more than 4 times reduction in scattering loss originating from surface roughness.

It has to be remarked again that all the  $\text{Si}_3\text{N}_4$  waveguides used in this thesis are multi-mode waveguides due to required anomalous dispersion. The fundamental mode of a waveguide can be coupled to higher-order modes due to sidewall roughness. This can be modeled by modified coupled-power theory based on [87, 89]. Here, coupled-power theory is only valid for weak coupling between different transverse modes, i.e., a complete exchange of power between two modes requires a distance much larger than the wavelength. Since we are considering the weak coupling due to weak sidewall roughness, this approximated theory is valid. Considering all the power is carried at the fundamental mode ( $\mu$ ) at the initial point of a waveguide, the coupled power equation due to one waveguide sidewall can be written as [89]

$$\frac{dP_\mu}{dz} = -(2\alpha_\mu + \sum_{\nu=1}^N h_{\mu\nu})P_\mu, \quad (3.9)$$

where  $P_\mu$  is the power carried by the fundamental mode  $\mu$ ,  $2\alpha_\mu$  is the propagation loss of mode  $\mu$ , and  $\nu$  indicates all the other guided modes that carry power apart from  $\mu$  mode.  $h_{\mu\nu}$  are the coupling coefficients between modes  $\mu$  and  $\nu$ , and are described as

$$h_{\mu\nu} = |\hat{K}_{\mu\nu}|^2 \langle |F(\beta_\mu - \beta_\nu)|^2 \rangle, \quad (3.10)$$

Here, the spectral density of waveguide roughness  $\langle |F(\beta_\mu - \beta_\nu)|^2 \rangle$  is

$$\langle |F(\beta_\mu - \beta_\nu)|^2 \rangle = \frac{2\sigma^2}{L_c} \frac{1}{(\beta_\mu - \beta_\nu)^2 + 1/L_c^2}, \quad (3.11)$$

### 3.1. Origin of waveguide losses

---

where  $L_c$  is the correlation length.  $|\hat{K}_{\mu\nu}|^2 = |\hat{K}_{\mu\nu}^{(i)}|^2 + |\hat{K}_{\mu\nu}^{(e)}|^2$ .  $\hat{K}_{\mu\nu}^{(i)}$  and  $\hat{K}_{\mu\nu}^{(e)}$  account for the coupling between mode  $\mu$  and  $\nu$ , due to the field at the internal and external sides of waveguide edge, respectively. They are described as [87]

$$\hat{K}_{\mu\nu}^{(i)} = \frac{i\omega\epsilon_0}{4P} (n_2^2 - n_1^2) \int_{-d}^d dy [\vec{E}_{\mu t}^* \cdot \vec{E}_{\nu t}]_{x=w-\sigma/2}, \quad (3.12)$$

$$\hat{K}_{\mu\nu}^{(e)} = \frac{i\omega\epsilon_0}{4P} (n_2^2 - n_1^2) \int_{-d}^d dy [\vec{E}_{\mu t}^* \cdot \vec{E}_{\nu t}]_{x=w+\sigma/2}, \quad (3.13)$$

where  $P$  is the total power of the guided mode,  $\epsilon_0$  is permittivity in vacuum,  $n_2$  and  $n_1$  are the refractive index of the core and clad materials, respectively.  $\vec{E}_{\mu t}$  and  $\vec{E}_{\nu t}$  are transverse parts of electrical field of mode  $\mu$  and  $\nu$ , respectively. Waveguide width is  $2w$ , and height is  $2d$ . A  $\text{Si}_3\text{N}_4$  waveguide with height 700 nm and width 2000 nm is used as an example for coupling loss calculation at wavelength of 1550 nm. The waveguide supports 3 transverse modes in TE polarization ( $\text{TE}_0$ ,  $\text{TE}_1$  and  $\text{TE}_2$ ) and 3 transverse modes in TM polarization ( $\text{TM}_0$ ,  $\text{TM}_1$  and  $\text{TM}_2$ ). The mode field of different transverse modes at wavelength 1550 nm are simulated using Lumerical Mode, and the coupling coefficients  $2h_{\mu\nu}$  (considering coupling due to sidewall roughness from both sidewalls of the waveguide) for both TE and TM polarization with respect to different correlation lengths are calculated and shown in Fig. 3.5. The coupling is undesirably maximized when correlation length is  $1/|\beta_\mu - \beta_\nu|$ . Since attaining correlation length larger than  $1.5 \mu\text{m}$  seems to be difficult [52, 90][Paper B], it's beneficial to have small correlation length. The coupling from  $\text{TE}_0$  to  $\text{TE}_2$  is overall much stronger than that to  $\text{TE}_1$  since the electric field of  $\text{TE}_2$  at the waveguide edge is much larger than that of  $\text{TE}_1$ . With  $\sigma=1\text{nm}$  and  $L_c=500\text{nm}$  reported in [Paper B], the loss due to coupling from  $\text{TE}_0$  to  $\text{TE}_1$  is 0.34 dB/m, and is 0.77 dB/m from  $\text{TE}_0$  to  $\text{TE}_2$ . The total propagation loss of the waveguides was measured to be  $\sim 3\text{ dB/m}$ .

In addition to the coupling between different transverse modes, which only happens in multi-mode waveguides, sidewall roughness of a waveguide can introduce coupling from the forward-propagating mode to the backward-propagating mode. In fact, since back-scattering coefficient scales with  $(\partial n_{\text{eff}}/\partial w)^2$  [91], this effect is more significant for high confinement single-mode waveguides, seeing Fig. 2.2 and 3.4. The power of back scattered light increases exponentially due to periodic sidewall roughness, which can be regarded as Bragg scattering, whereas the power of the back scattered light increases linearly due to random sidewall roughness [89]. This provides a guideline for the nano-fabrication of waveguides. In this thesis work, we

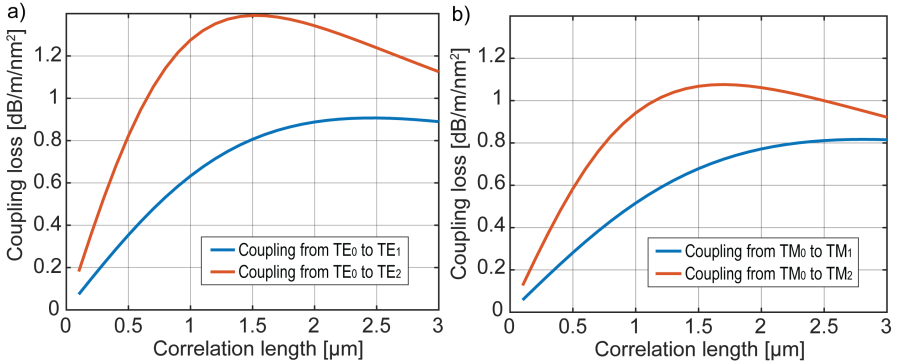


**Figure 3.5:** Coupling from the fundamental mode to higher-order modes due to sidewall roughness from both sidewalls. The  $\text{Si}_3\text{N}_4$  waveguide geometry is height 700 nm and width 2000 nm. a) TE polarization. b) TM polarization. The coupling loss is normalized to squared RMS roughness in squared nanometers.

observed a relatively weak resonance splitting in microresonators due to the coupling between clockwise- and counter-clockwise propagating modes. This effect will be described in section 3.2.2.

### 3.1.4 Material losses

Material losses can include absorptive and scattering losses. The absorptive losses include intrinsic absorption due to electronic transitions and vibrational transitions [78], as well as extrinsic absorption due to contaminants introduced during material deposition and any post-processes. Electronic transitions refer to electrons getting energy from photons and raising from the valence band to the conduction band. This effect is almost negligible in both  $\text{Si}_3\text{N}_4$  and  $\text{SiO}_2$  at the telecommunication band, due to their large bandgap  $> 4$  eV. Absorption due to vibrational transitions results from molecule vibrational modes, e.g., bending and stretching modes. In contrast to electronic transitions in ultraviolet wavelength, vibrational transitions typically result in absorption in the infrared region.  $\text{Si}_3\text{N}_4$  films deposited from precursors  $\text{SiH}_2\text{Cl}_2$  and  $\text{NH}_3$  have undesired N-H bonds, which result in vibrational transition in wavelength near 1510 nm [92]. Even though high temperature ( $>1100$  °C) is implemented to outgas hydrogen [93–95], the residual of N-H bonds can still result in non-negligible absorption near 1510 nm in ultra-high Q  $\text{Si}_3\text{N}_4$  microresonators

## 3.2. Waveguide loss characterization methods

---

[75]. Apart from intrinsic absorption, extrinsic absorption can be introduced during material depositions and high temperature processes. It was pointed out in [52] that ppm-level metal impurity concentration introduced from LPCVD can result in significant absorptive loss.

Rayleigh scattering can arise in materials with volumetric inhomogeneities of refractive index. Regarding silicon nitride thin films deposited by LPCVD, Si nanoparticles can be introduced by the pyrolysis of DCS gas, and this effect is more significant for SiRN [96]. Moreover, it's observed that Si-clusters are further increased after annealing at high temperature ( $> 1100^{\circ}\text{C}$ ) in SiRN thin films [97]. These Si nano-particles and clusters introduce large refractive index inhomogeneities, and can dramatically introduce losses due to Rayleigh scattering. In [Paper A], relatively small gases ratio  $\text{DCS}:\text{NH}_3=3.9$  is used to deposit SiRN films without crack formation, and the ratio is below the threshold to avoid increased Si cluster during annealing process at  $1100^{\circ}\text{C}$  [97]. However, non-negligible material loss was observed compared with  $\text{Si}_3\text{N}_4$  in [Paper B]. Apart from Si nano-particles which introduce significant inhomogeneities of refractive index, non-uniformity of refractive index of  $\text{Si}_3\text{N}_4$  thin films can also originate from unstable flows of precursor gases and unstable temperature during deposition and, more fundamentally, is introduced when the material is solidified from melting state to amorphous solid state [78].

## 3.2 Waveguide loss characterization methods

Under different scenarios, different methods are needed to characterize waveguide losses. Three methods used in this thesis work are described, including their pros and cons.

### 3.2.1 Cut-back method

The cut-back method for characterization of waveguide loss relies on measuring the transmission losses of several waveguides with different lengths. The transmission loss of a waveguide includes coupling losses between the optical fiber and the waveguide, and propagation loss of the waveguide. The measurement typically follows a procedure, 1) measure the transmission loss of a waveguide with length  $L_1$ ; 2) cleave the waveguide into two parts with lengths  $L_2$  and  $L_3$  ( $L_2 \neq L_3$ ), and measure the transmission losses of cleaved waveguides; 3) apply a first-order polynomial fitting on three transmission losses with respect to their waveguide lengths. The fitted slope

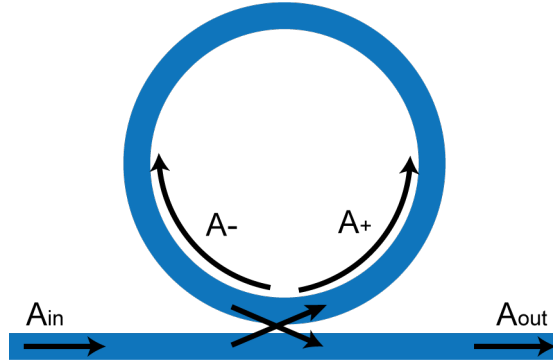


**Figure 3.6:** The schematic of a microring resonator coupled with a bus waveguide.

corresponds to propagation loss of the waveguide, and the intercept represents the total coupling loss from both coupling facets.

This method is destructive, meaning that a waveguide needs to be cleaved into several parts. It can be extended to measure several waveguides with different lengths. On the bright side, the method is convenient since it only relies on an isolated waveguide and doesn't rely heavily on the precision of the tunable laser. Since the method does not strictly distinguish propagation from coupling losses, multiple pieces of the waveguide should be used to decrease the uncertainty. In paper A, this method was used to measure the waveguide losses.

### 3.2.2 Microring resonator

Microring resonators have been widely used to characterize waveguide loss [98]. This method is very convenient when the waveguide losses go below 1 dB/m. The schematic of a microring resonator is shown in Fig. 3.6. The equivalent propagation loss is acquired from the intrinsic linewidth or intrinsic Q factor of the microring resonator. As discussed in section 3.1.3, mode coupling between forward- and backward-propagating modes can be introduced due to interfacial inhomogeneities of a waveguide. The resonance profile have a Lorentzian shape when the coupling is negligible and feature a split doublet when coupling between counterpropagating modes is apparent [99]. During this thesis work, it was observed that some resonances were affected by this coupling effect. An example is given in Fig. 3.7.

### 3.2. Waveguide loss characterization methods

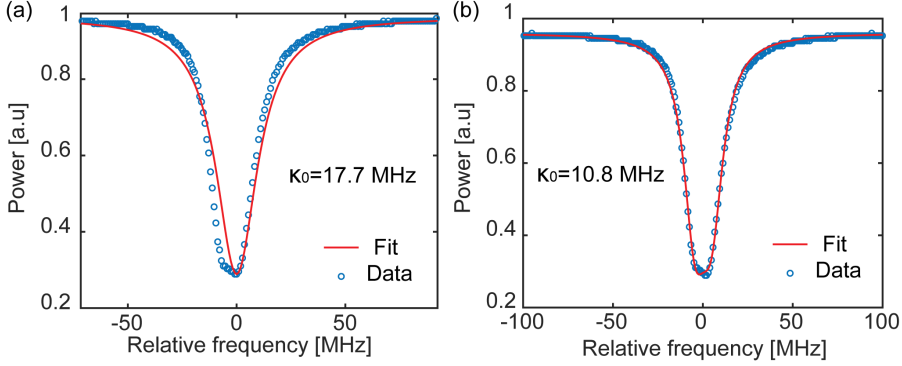


**Figure 3.7:** A measured resonance with fitting of Lorentzian model (a), and resonance split model (b).

Although no visible splitting feature was observed from the raw measurement data, the Lorentzian model (Fig. 3.7a) leads to an improper fitting, whereas the resonance split model (Fig. 3.7b) results in a better fit. Remarkably, almost a factor of two difference is obtained in the retrieved value of the intrinsic loss.

When the coupling between forward- and backward-propagating modes are included, the set of coupled-mode equations describing the principle of microring resonator are [99]

$$\frac{dA_+}{dt} = -\left(\frac{\kappa_0}{2} + \frac{\kappa_{ex}}{2} + i\Delta\omega\right) \cdot A_+ + iA_- \cdot \frac{\kappa_c}{2} + iA_{in} \cdot \sqrt{\kappa_{ex}}, \quad (3.14)$$

$$\frac{dA_-}{dt} = -\left(\frac{\kappa_0}{2} + \frac{\kappa_{ex}}{2} + i\Delta\omega\right) \cdot A_- + iA_+ \cdot \frac{\kappa_c}{2}, \quad (3.15)$$

$$A_{out} = A_{in} + i\sqrt{\kappa_{ex}} \cdot A_+, \quad (3.16)$$

Here  $A_+$  and  $A_-$  are the amplitude of the electric fields normalized to energy in the counter clockwise and clockwise directions, respectively, in the microring.  $A_{in}$  and  $A_{out}$  are the amplitude of the electric fields normalized to power at the input and output of the bus waveguide, respectively. The intrinsic loss rate (intrinsic linewidth) is

$$\kappa_0 = \frac{\alpha c}{2\pi n_g}, \quad (3.17)$$

where  $\alpha$  is propagation loss,  $c$  is speed of light in vacuum and  $n_g$  is group index of the microring waveguide. Here, the propagation loss of the waveguide includes both

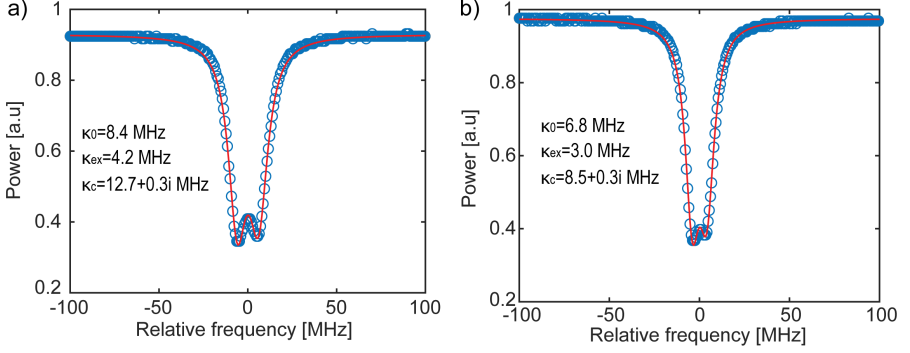


**Figure 3.8:** Two examples of measured resonance split. Blue circles are measurement data, and red curves are fitting results.

scattering losses and absorptive losses.  $\kappa_{ex}$  is the external coupling rate (extrinsic linewidth), depending on the coupling strength between bus and ring waveguides.  $\Delta\omega$  is the frequency detuning with respect to the frequency of an unperturbed resonance.  $\kappa_c$  is the internal coupling between counter-clockwise and clockwise modes, which is originated from interfacial inhomogeneities [99]. When  $\kappa_c \neq 0$ , resonance split can be observed. The transmission response can be described as

$$\left| \frac{A_{out}}{A_{in}} \right|^2 = \left| \frac{(\kappa_0/2)^2 - (\kappa_{ex}/2)^2 - \Delta\omega^2 + i\Delta\omega\kappa_0 + (\kappa_c/2)^2}{(\kappa_0/2 + \kappa_{ex}/2)^2 + (\kappa_c/2)^2 - \Delta\omega^2 + i\Delta\omega(\kappa_0 + \kappa_{ex})} \right|^2, \quad (3.18)$$

The split resonance is symmetric when  $\kappa_c$  is a real number, while asymmetric resonance split is observed when  $\kappa_c$  is a complex number. Practically, two fittings with  $\kappa_c$  as a real number and a complex number are applied on the measurement data. The better fitting is adopted. The asymmetry of the resonance split can be interpreted by imperfections of the coupler [100] and indirect (dissipative) scattering between counter-clockwise and clockwise modes [52, 101].

Two split resonances acquired from a microring resonator with ring waveguide  $750 \text{ nm} \times 2000 \text{ nm}$  are shown in Fig. 3.8. The intrinsic linewidth are 8.4 MHz and 6.8 MHz, corresponding to equivalent propagation loss (calculated by  $\alpha = 2\pi n_g k_0/c$ ) of 1.6 dB/m and 1.3 dB/m, respectively.

When coupling between two counter-propagating modes is negligible ( $\kappa_c = 0$ ),

## 3.2. Waveguide loss characterization methods

---

Lorentzian resonances can be obtained

$$\left| \frac{A_{out}}{A_{in}} \right|^2 = \left| 1 - \frac{\kappa_{ex}}{\kappa_0/2 + \kappa_{ex}/2 + i\Delta\omega} \right|^2, \quad (3.19)$$

Here, additional information is needed to distinguish  $\kappa_0$  from  $\kappa_{ex}$ , for example measuring several microring resonators with different gaps or measuring phase response of transmission scan. The microring resonator is over-coupled when  $\kappa_{ex} > \kappa_0$ , while is under-coupled when  $\kappa_{ex} < \kappa_0$ .

Waveguide loss characterization based on microring resonator is fast and convenient since it does not require waveguide to be sufficiently long. However, a few cautions should be paid on this method. Firstly, microring resonator is a good way to evaluate the imperfections of waveguides and material losses, but it omits the fabrication yield since only a short waveguide is needed, see more detailed analysis in section 5.1. Secondly, the bus waveguide should be carefully designed to maintain high coupling ideality (the fundamental mode of the ring waveguide should be coupled to the fundamental mode of the bus waveguide) [102, 103], especially in the high-Q regime. Last but not least, the gap between bus and ring waveguides should be perfectly filled by cladding material. Otherwise, the strong back-scattering in the coupling region could lead to an incorrect determination of waveguide propagation loss.

### 3.2.3 Optical frequency-domain reflectometry

Optical frequency-domain reflectometry (OFDR) is used for the analysis of reflection characteristics of optical components. The light source can be a pulse, then a spectrometer is needed to simultaneously attain all spectral information. For simplicity, in this thesis, the light source is a swept-wavelength laser, and the spectrometer is replaced by a photodetector [104]. The schematic of the OFDR used in this thesis is shown in Fig. 3.9. The reference arm is indicated by a red arrow. The device arm, which is used for measuring a spiral waveguide, is indicated by a green arrow. The reflected signal originates from scattering of the measured waveguide. The complex transfer function of the waveguide can be written as  $H(\omega)$ . We can consider the waveguide as a multi-layer medium, then  $H(\omega)$  becomes

$$H(\omega) = \sum_j r_j(\omega) \exp(-i\omega\tau_j), \quad (3.20)$$

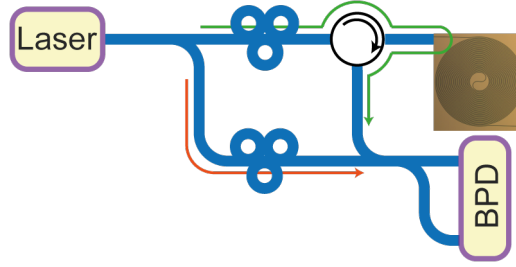


**Figure 3.9:** Schematic of OFDR. The reference arm and measurement arm are labeled by red and green color, respectively. BPD, balanced photodetector.

where  $r_j(\omega)$  is the transfer function of the waveguide to location  $j$ , and  $\tau_j$  is its delay with respect to the reference arm. The measured power by the photodetector is [105]

$$P(\omega) \propto \sum_j |E(\omega)|^2 [1 + |r_j(\omega)|^2 + r_j(\omega)\exp(-i\omega\tau_j) + c.c.], \quad (3.21)$$

where  $|E(\omega)|^2$  is the power spectrum of the swept-wavelength laser source. By applying inverse-Fourier transform to  $P(\omega)$ , reflected power with respect to delay  $\tau$  can be obtained. In the other word, the reflected power with respect to waveguide position is retrieved. Assuming the reflectivity of the waveguide is similar at different positions, the waveguide propagation loss can be acquired by applying a first-order polynomial fit on the inverse-Fourier transformed  $P(\omega)$ . OFDR is a high-sensitivity and non-destructive technique [106], and small defects in the waveguide can be identified precisely. The only drawback is that the laser tuning must be calibrated carefully. In this thesis, this is done with the aid of a self-referenced frequency comb, similar to [107].

## Chapter 4

# Effect of linear losses in Kerr nonlinear optics

As mentioned in Chapter 2, an integrated waveguide can highly confine light in a sub- $\mu\text{m}^2$  effective area. With such a small effective area, high optical intensity  $> 100 \text{ MW/cm}^2$  can be obtained by efficiently coupling 1 W of optical power. For nonlinear optics, light with such high optical intensity can interact with the waveguide by modifying the refractive index of the materials. The nonlinear Kerr effect highly relies on the nonlinear phase shift ( $\Phi_{NL} = \gamma PL_{\text{eff}}$ ) which is accumulated along the propagation in a nonlinear waveguide. Therefore, the propagation loss of the waveguide is one of the key factors in nonlinear optics. This chapter introduces the effects of propagation loss in Kerr nonlinear optics, especially in parametric amplifiers and Kerr microcombs.

### 4.1 Kerr effect

Nonlinear optical phenomena arise from the nonlinear relation between the induced polarization of a material subject to a strong electric field. The electric flux density relates to the electric field through the constitutive relation

$$\vec{D} = \epsilon_0 \vec{E} + \vec{P}, \quad (4.1)$$

where  $\vec{P}$  is the induced polarization, and  $\vec{D}$  is electrical flux density. Since this thesis focuses on amorphous  $\text{Si}_3\text{N}_4$  and  $\text{SiO}_2$ , the medium can be considered to be isotropic and homogeneous. Therefore,  $\vec{P}$  is parallel to  $\vec{E}$  and can be written as [108]

$$\vec{P} = \epsilon_0(\chi^{(1)} \cdot \vec{E} + \chi^{(2)} : \vec{E}\vec{E} + \chi^{(3)} : \vec{E}\vec{E}\vec{E} + \dots), \quad (4.2)$$

where  $\chi^{(i)}$  is  $i$ -th order susceptibility.  $\chi^{(1)}$  is for linear optics, based on which the refractive index can be defined as  $n_0 = \sqrt{1 + \chi^{(1)}}$ . The term  $\chi^{(2)}$  is responsible for second-harmonic generation and sum frequency generation, and it only appears in materials lacking inversion symmetry, and is negligible in  $\text{Si}_3\text{N}_4$  and  $\text{SiO}_2$ . The third-order susceptibility  $\chi^{(3)}$  exists in all materials, and is responsible for third-harmonic generation and four-wave mixing (FWM). This thesis focuses on third-order nonlinearity. For  $\chi^{(3)}$  media, the refractive index can be written as

$$n = n_0 + n_2 |E|^2, \quad (4.3)$$

where  $n_2$  is the nonlinear-index coefficient. Considering  $\vec{E}$  is linearly polarized in  $x$  direction,  $n_2$  is related to  $\chi^{(3)}$  as

$$n_2 = \frac{3}{8n_0} \text{Re}(\chi_{xxxx}^{(3)}). \quad (4.4)$$

The Kerr effect indicates that the variation of refractive index is linearly proportional to the intensity of the light. In an integrated waveguide, the core and clad materials can have significantly different  $n_2$  values. For example  $n_2$  value for  $\text{Si}_3\text{N}_4$  ( $2.4 \times 10^{-15} \text{cm}^2/\text{W}$  [109]) is 10 times larger than that for  $\text{SiO}_2$  ( $2.2 \times 10^{-16} \text{cm}^2/\text{W}$  [110]). Moreover, as described in Chapter 2, the optical mode of a waveguide can be dramatically changed by engineering the waveguide geometry. Therefore, an averaged nonlinear-index coefficient  $\bar{n}_2$  is introduced as [72]

$$\bar{n}_2 = k \left( \frac{\epsilon_0}{\mu_0} \right) \frac{\int n_0^2(x,y) n_2(x,y) [2 |\vec{E}|^4 + |\vec{E}^2|^2] dA}{3 \int |(\vec{E} \times \vec{H}^*) \cdot \hat{z}|^2 dA}. \quad (4.5)$$

Here, the spatial distribution of  $n_0$ ,  $n_2$  and mode fields are taken into account. Compared with [108], the full vectorial nature of the propagating mode is considered. The nonlinear parameter  $\gamma$  is introduced [72]

$$\gamma = \frac{2\pi\bar{n}_2}{\lambda A_{\text{eff}}}, \quad (4.6)$$

where  $A_{\text{eff}}$  is described in Eq. 2.2. It's obvious that a large  $\bar{n}_2$  and small  $A_{\text{eff}}$  are desired for attaining a large nonlinear parameter.

## 4.2 Effect of loss on parametric amplifiers

Optical parametric amplification (OPA) based on the Kerr effect is a FWM process, where the input signal wave is amplified by the pump wave along the propagation in a nonlinear waveguide, and an idler wave is generated. This thesis focuses on parametric amplifiers based on a degenerated FWM process, where two pump photons with same angular frequency  $\omega_p$  are converted into one signal photon ( $\omega_s$ ) and one idler photon ( $\omega_i$ ), and  $2\omega_p = \omega_s + \omega_i$ . The schematic of an OPA based on a degenerated FWM process is depicted in Fig. 4.1, and the definitions of gain and conversion efficiency are given. In contrast to amplifiers based on transitions between energy levels, the operation wavelength of OPAs is flexible and relies on the dispersion engineering of a nonlinear waveguide. By precisely maintaining the phase matching among the pump, signal and idler waves, ultra-broadband operation can be achieved [31]. In contrast to conventional amplifier with quantum limited 3 dB noise figure (NF) [111], an OPA working in a phase-sensitive mode can ideally achieve a NF of 0 dB [112]. In order to amplify a continuous stream of data, the pump wave should be CW. CW-pumped OPAs were only achieved in bulky optical fibers [113, 114] due to their ultralow loss. Substantial efforts were paid aiming for CW-pumped OPAs on different integrated Kerr nonlinear waveguide platforms [30, 31, 115–119], but the results have been limited by both linear and nonlinear losses. This thesis reports the first CW-pumped OPA in an integrated Kerr waveguide. It's achieved thanks to the ultra-low propagation losses and absence of nonlinear losses in the near-infrared of the silicon nitride waveguides presented in [paper D].

When the loss of the nonlinear medium is ignored, the analytical solution of the parametric gain coefficient  $g$  can be acquired [113, 120], and  $g$  is described as

$$g = \sqrt{(\gamma P_p)^2 - (\gamma P_p - \Delta\beta/2)^2}, \quad (4.7)$$

where  $P_p$  is the pump power, and  $\Delta\beta = 2\beta_p - \beta_s - \beta_i$ .  $\beta_p$ ,  $\beta_s$  and  $\beta_i$  are the propagation constant of the pump, signal and idler waves. It's obvious that maximum parametric gain coefficient is obtained when perfect phase matching  $\Delta\beta/2 = \gamma P_p$  is achieved. When the power of amplified signal wave is much weaker than that of pump, i.e., the depletion of the pump wave is negligible, the signal gain ( $G$ ) can be written as

$$G = 1 + \left[ \frac{\gamma P_p}{g} \sinh(gL) \right]^2. \quad (4.8)$$

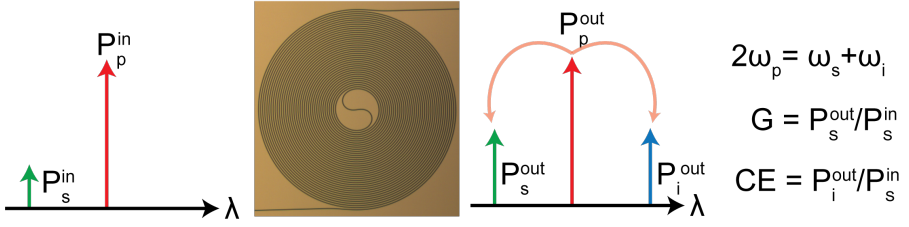


**Figure 4.1:** The schematic of an OPA based on a degenerated FWM process. The pump wave and the signal wave are launched into a nonlinear waveguide. At the output of the waveguide, the signal wave is amplified, and an idler wave is generated. Gain ( $G$ ) is defined as the ratio of the power of the signal wave at the output to that at the input. Conversion efficiency ( $CE$ ) is defined as the ratio of the idler wave at output to the power of the signal wave at the input.

When perfect phase matching is maintained along the propagation, an exponential  $G$  can be obtained, and is written as

$$G^{(exp)} \approx \frac{1}{4} \exp(2\gamma P_p L). \quad (4.9)$$

When the loss of the linear medium are considered, it's typical to replace the length of the Kerr nonlinear medium with the effective length  $L_{\text{eff}} = \frac{1 - \exp(-\alpha L)}{\alpha}$ . However, this approximation is not valid for lossy waveguides as the above expression only accounts for the limited nonlinear phase shift accumulated by the pump and ignores the attenuation experienced by the signal and idler waves.

As a result, in order to precisely model OPA in a waveguide with linear loss, the nonlinear Schrödinger equation (NLSE) is needed [108]

$$\frac{\partial A}{\partial z} = i\gamma |A|^2 A - \frac{i\beta_2}{2} \frac{\partial^2 A}{\partial t^2} - \frac{\alpha}{2} A, \quad (4.10)$$

where  $A$  is the slowly varying electric field envelope. The three terms on the right hand side of NLSE are responsible for the Kerr nonlinear effect, dispersion and propagation loss, respectively. For simplicity, only second-order dispersion is considered, i.e., a Taylor expansion up to second order in Eq. 2.3.

Few simulations are carried out based on a 3 meter  $\text{Si}_3\text{N}_4$  waveguide with height 660 nm and width 1600 nm. The  $\gamma$  is  $1.13 \text{ m}^{-1}\text{W}^{-1}$ ,  $\beta_2 = -3.5 \text{ ps}^2/\text{km}$  at 1560 nm, the wavelength of the pump wave is 1560 nm and the pump power is 34 dBm. The

## 4.2. Effect of loss on parametric amplifiers

---

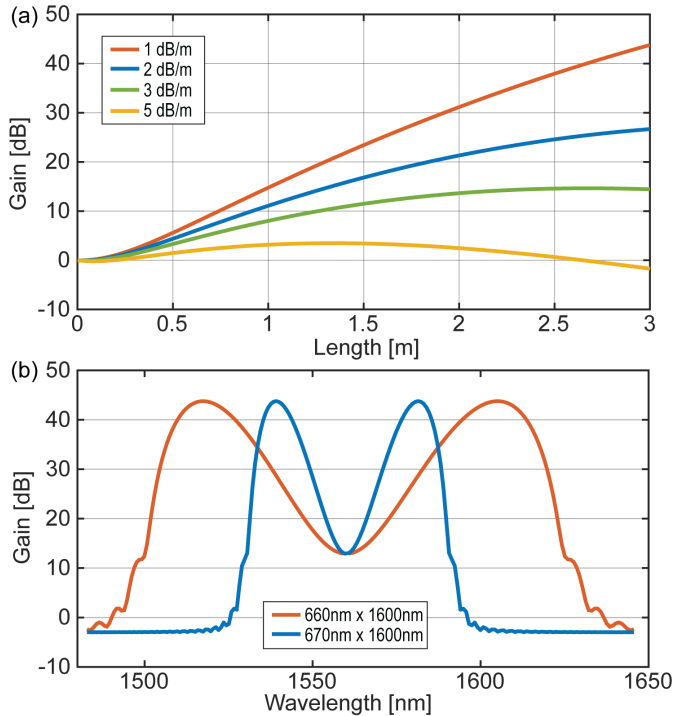


**Figure 4.2:** Simulation result of OPAs. (a) Signal gain along the propagation in a 3 meter  $\text{Si}_3\text{N}_4$  waveguide with height 660nm and width 1600nm. The signal wavelength is located at the peak of the gain spectrum at the output of the waveguide. Four different waveguide losses are included. (b) Gain spectra of 3 meter  $\text{Si}_3\text{N}_4$  waveguides with slightly different height. The losses of both waveguides are 1 dB/m.

simulation results based on different waveguide losses are shown in Fig. 4.2a. The wavelength of the signal wave is located at the peak of the gain spectrum at the output port. As can be seen in Fig. 4.2a, the gain of the signal wave can be as large as 43 dB in a 3 meter  $\text{Si}_3\text{N}_4$  waveguide with propagation loss of 1 dB/m. It's obvious that, with a propagation loss of 1.4 dB/m, the waveguide length of 1.42 meter is not the optimal length in [Paper D]. However, the length of the waveguide in [Paper D] was chosen as a compromise of the writing time in EBL and fabrication yield (see Chapter 5 for a detailed analysis). The gain of the signal wave degrades dramatically with increased waveguide loss from 1 dB/m to 3dB/m. In a  $\text{Si}_3\text{N}_4$  waveguide with loss of 5 dB/m, only a maximum of 3 dB gain can be obtained by a 1.2-meter-long waveguide. From this analysis, it is obvious that both meter-scale  $\text{Si}_3\text{N}_4$  waveguides and ultralow-losses are the key to attain CW-pumped OPAs, as demonstrated in [Paper D]. The corresponding gain spectrum of a 3 meter  $\text{Si}_3\text{N}_4$  waveguide with loss of 1 dB/m is shown in the red curve in Fig. 4.2b. As can be seen, the bandwidth of OPA with gain larger than 10 dB exceeds 130 nm, which can cover both C- and L-bands. However, practically, the variation of waveguide dispersion should be taken into account. As discussed in section 2.2, the variation of the thickness of  $\text{Si}_3\text{N}_4$  thin film across the wafer can be more than 10 nm. Therefore, a simulation based on a  $\text{Si}_3\text{N}_4$  waveguide with slightly increased height (670 nm) is carried out and illustrated in blue curve in Fig. 4.2(b). By increasing the waveguide height from 660 nm to 670 nm, the dispersion value at 1560 nm is modified from  $-3.5 \text{ ps}^2/\text{km}$  to  $-15 \text{ ps}^2/\text{km}$ . Consequently, the bandwidth of OPA with gain greater than 10 dB is reduced from 130 nm to 60 nm. Furthermore, if the dispersion variation along the waveguide is considered, the impact can be even worse than reduced bandwidth. Since the phase matching condition ( $\Delta\beta/2 = \gamma P_p$ ) along the propagation can not be perfectly met, the gain of OPA can be degraded. Based on this analysis, the layout of 1.42 meter long  $\text{Si}_3\text{N}_4$  waveguides in [Paper D] is not optimal. Ideally, the long waveguide should be packed in a squared device area so that the impact of the variation of film thickness is minimized. In fact, since the waveguide loss is non-negligible, the right hand side of the phase matching equation is reducing along the propagation. This means the perfect phase matching is not met, and is more severe for more lossy waveguides. In order to compensate this effect, waveguide tapering design [121] should be adopted to keep perfect phase matching, which in turn increases the gain. However, this can further increases the requirement of rigid dispersion engineering.

The increased total propagation loss of a waveguide also degrades the NF of OPA. In fact, the noise figure of an amplifier is as important as its gain. The analysis of

### 4.3. Effect of loss on Kerr microcombs

---

the NF of lossy phase-sensitive amplifiers is presented for the first time in [Paper D]. The analysis presented in the supplementary of [Paper D] clearly indicates that, for the same length of the waveguide, even though higher pump power can be used to overcome the larger loss of the waveguide to achieve same parametric gain, the NF of an OPA is degraded due to the larger waveguide loss. It should be marked that, with same parametric gain, the NF of an OPA is determined by the total loss of the waveguide.

### 4.3 Effect of loss on Kerr microcombs

The generation of optical microcombs in high-Q microresonators relying on the Kerr effect was firstly reported in [39] using a SiO<sub>2</sub> microtoroid. The operational principle is similar to an optical parametric oscillator, relying on the intensity build up facilitated by the high-Q microresonator. Due to the strong optical field confinement and resonant power buildup [122], parametric amplification can be attained with extremely low power levels at the bus waveguide. When parametric gain is large enough to overcome the propagation loss in a microresonator, new comb lines are generated through FWM processes. The threshold power to reach parametric oscillation is estimated by

$$P_{\text{th}} = 1.54 \frac{\pi}{2} \frac{Q_c}{2Q_L} \frac{n^2 V}{n_2 \lambda Q_L^2}, \quad (4.11)$$

where  $V$  is the mode volume of the microresonator,  $Q_c$  and  $Q_L$  are coupled quality factor and loaded quality factor, respectively. The intrinsic quality factor  $Q_i$  is related to the intrinsic linewidth  $\kappa_0$  by  $Q_i = \omega/2\pi\kappa_0$ , and is related with  $Q_c$  and  $Q_L$  by  $1/Q_L = 1/Q_i + 1/Q_c$ . According to Eq. 4.11, it's clearly that  $P_{\text{th}}$  scales with  $\sim 1/Q_i^2$ . Moreover, for cavities with small FSR, where the volume is increased, much higher  $Q_i$  is needed to overcome the increase in power threshold. Fig. 4.3 illustrates the dependence of  $P_{\text{th}}$  on  $Q_i$ , including Si<sub>3</sub>N<sub>4</sub> microresonators with FSR of 1 THz, 100 GHz and 20 GHz. The parameters used for the calculation are  $A_{\text{eff}}=1 \mu\text{m}^2$ ,  $\lambda=1550$  nm,  $Q_c=Q_i$  and  $n_2=2.4 \times 10^{-19} \text{ m}^2/\text{W}$ . As can be seen in Fig. 4.3, when working with a microresonator with FSR of 1 THz [Paper F], only a few milliwatts of optical power are needed to compensate the low  $Q_i \sim 1 \times 10^6$ . However, when working with a microresonator with FSR of 20 GHz or even 14 GHz in [Paper E], high  $Q_i > 10^7$  is required to bring down the operational power to milliwatts level. To be more precise, the DKS state requires to operate with a CW pump power a few times higher than

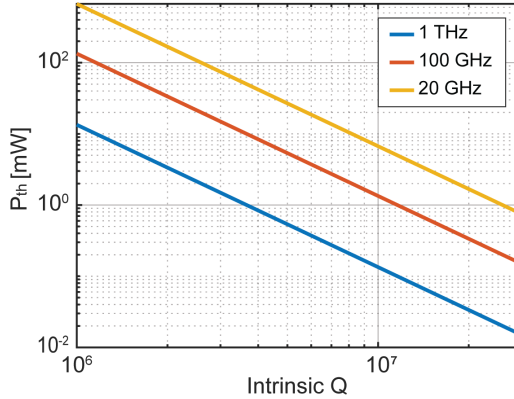


**Figure 4.3:** Dependence of  $P_{\text{th}}$  on  $Q_i$ .  $\text{Si}_3\text{N}_4$  microresonators with FSR of 1 THz, 100 GHz and 20 GHz are included.

the parametric oscillation threshold [123]. In [Paper B, E], much higher pump power than  $P_{\text{th}}$  for parametric oscillation was chosen so that the soliton existence range is large and the corresponding soliton steps are relatively long [123, 124], as this reduces significantly the complexity of the experiments.

DKS microcombs exist in both normal and anomalous dispersion regimes [123, 125–128]. In the normal dispersion regime, the temporal waveform of a DKS microcomb is a dark pulse, where locally reduced optical power shows up in a CW background with high power [129]. One outstanding feature of DKS microcombs in normal dispersion regime is that its power conversion efficiency (calculated by the converted power excluding the pump line normalized to the power of input pump) can reach  $> 30\%$  [130]. In the anomalous dispersion regime, the temporal waveform of a DKS microcomb is a bright soliton with a typical temporal shape of squared hyperbolic secant ( $\text{sech}^2$ ). A single (multi-) soliton microcomb refers to single (more than one) soliton pulse circulating in a microresonator. The power conversion efficiency of single soliton microcombs in anomalous dispersion regime is typically only a few percentages due to large effective detuning between the pump wavelength and the cavity resonance [130].

The dynamics of microcombs are typically modeled by the Ikeda map [131] or the Lugiato-Lefever equation [124, 132]. Here, we use the Ikeda map to analyze the effect of  $Q_i$  on the power of the weakest comb line within a certain bandwidth. This

### 4.3. Effect of loss on Kerr microcombs

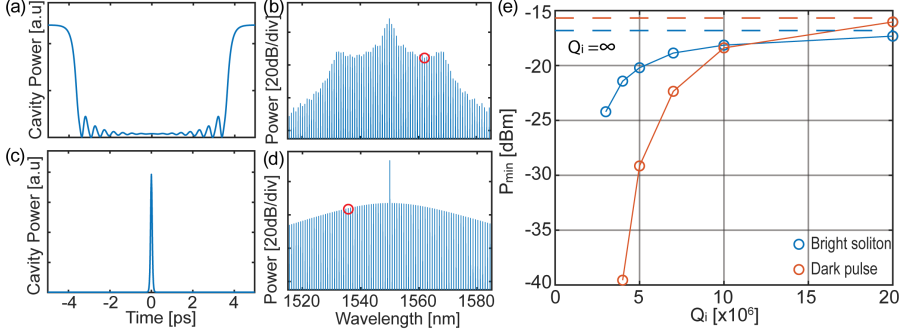


**Figure 4.4:** (a) Intracavity temporal waveform of a dark pulse comb when  $Q_i = \infty$ . (b) Spectrum of the dark pulse microcomb at the output port. The red circle highlights the weakest comb line. (c) and (d) are similar to (a) and (b), but for a bright soliton comb. (e) Dependence of the power of the weakest comb lines in C-band with respect to intrinsic  $Q$ . The dashed line corresponds to the maximum achievable power of the weakest line in a lossless microresonator.

metric is relevant in the context of optical communications, as microcombs tend to be equalized to this comb line before transmission in a fiber link [133, 134]. In the following simulations, the pump wavelength is located at 1550 nm. The comb lines from 1535 nm to 1565 nm are taken into account. The parameters used for simulations are close to  $\text{Si}_3\text{N}_4$  microresonators: pump power is 20 mW,  $\gamma=1 \text{ m}^{-1}\text{W}^{-1}$ , FSR=100 GHz, coupling strength between bus and ring waveguides is 0.005. The dispersion for dark pulse microcombs is  $100 \text{ ps}^2/\text{km}$ , while the dispersion for bright soliton microcombs is  $-100 \text{ ps}^2/\text{km}$ . The detuning between the pump wavelength and cavity resonance is optimized to maximize  $P_{\min}$  for both bright soliton microcombs and dark pulse microcombs. The simulation results are shown in Fig. 4.4. As can be seen,  $P_{\min}$  of both types of microcomb are improved with increased  $Q_i$ . While bright soliton microcomb with  $Q_i > 7 \times 10^6$  is sufficient to attain  $P_{\min}$  approaching the ideal case, a dark pulse microcomb requires  $Q_i > 10 \times 10^6$  to achieve high performance. When  $Q_i$  of dark pulse microcomb is smaller than  $10 \times 10^6$ , the  $P_{\min}$  drops more dramatically compared with bright soliton microcomb. Therefore, normal dispersion microcombs are more demanding in terms of  $Q_i$ . In [Paper B], a high performance dark pulse microcomb with repetition rate of 100 GHz was firstly achieved in a microresonator with  $Q_i > 10 \times 10^6$ . This comb source was later used in [135] to reach

the highest data rate ever from a chip-scale comb source. It needs to be remarked that more careful engineering of dispersion and coupling strength [136] are required to optimize  $P_{\min}$  in aforementioned scenario. Here, only the impact of  $Q_i$  is analyzed. The above analysis proved that high- $Q$  microresonators are needed to reduce the pump power and improve the achievable comb line power. As discussed in the previous chapter, lossy waveguides result from imperfections that can also induce coupling between transverse modes. In microresonators, this coupling results in so-called avoided mode crossings [137]. Such avoided mode crossings, not only distort the spectra of DKS microcombs, but also potentially prohibit the generation of bright soliton microcomb [137]. In [Paper E], the statistical  $Q_i$  of the microresonator is improved to  $19 \times 10^6$ , and racetrack-shaped microresonators were properly designed to minimize the coupling between transverse modes. Therefore, low-repetition rate (down to 14 GHz) DKS microcombs were achieved for the first time in a compact microresonator with a footprint  $< 1 \text{ mm}^2$ . Apart from scattering losses, absorption losses in materials can result in increased thermal effects, which can make it even more challenging to access bright soliton microcombs [57]. During this PhD work, we observed that, when initializing soliton microcomb, the resonance shift due to thermal effect in SiRN [Paper A] was much stronger than that of  $\text{Si}_3\text{N}_4$  [Paper B, E]. Considering similar thermo-optic coefficients of  $\text{Si}_3\text{N}_4$  and SiRN [138], the enhanced resonance shift in SiRN indirectly indicates that the material loss (especially absorptive loss) in SiRN is much larger than that of  $\text{Si}_3\text{N}_4$ . This observation is consistent with few factors discussed in section 3.1.4.

## Chapter 5

# Fabrication techniques of ultra-low-loss silicon nitride waveguides

As described in Chapter 2, any imperfections in optical waveguides can lead to scattering losses, including scattering to radiation modes and transverse modes, and absorptive losses. The effects of losses on OPA and Kerr microcomb are discussed in chapter 4. It's obvious that ultralow-loss waveguides are needed for both parametric amplifiers and DKS microcombs. Here, we give an overview of the fabrication flow of silicon nitride waveguides. The few key fabrication techniques that lead to ultralow-losses are discussed in detail. The fabrication yield for photonics devices are discussed in the end.

### 5.1 Overview of fabrication process

In order to achieve ultralow-loss  $\text{Si}_3\text{N}_4$  waveguides, necessary cautions should be paid on almost every fabrication step. The schematic of fabrication flow is shown in Fig. 5.1. The whole process is divided into five parts highlighted in frames with different colors, including fabrication of crack barriers, silicon nitride deposition,

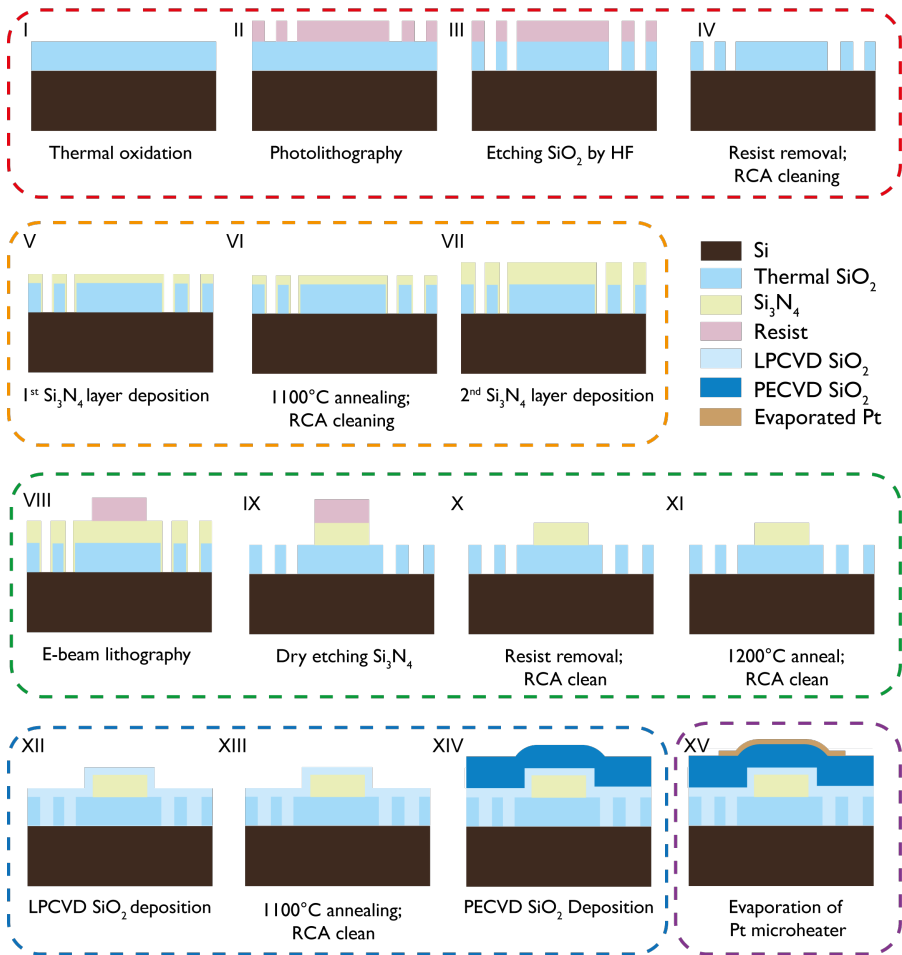


**Figure 5.1:** Schematic of fabrication flow of ultralow-loss  $\text{Si}_3\text{N}_4$  waveguides with microheaters. The red, orange, green, blue and purple dashed frames indicate the processes for fabrication of crack barriers, silicon nitride deposition, waveguide patterning, top cladding deposition and microheater evaporation, respectively.

## 5.2. Silicon nitride thin film deposition

---

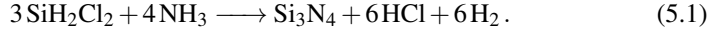
waveguide patterning, top cladding deposition and fabrication of microheater. Each part will be described briefly in this section, and few key steps that significantly contribute to attaining ultralow-losses will be described in following sections.

The fabrication process starts with a thermally oxidized 3-inch Si wafer with 3  $\mu\text{m}$   $\text{SiO}_2$ . The patterns of crack barriers are defined by UV lithography, and are translated into thick  $\text{SiO}_2$  layer by buffered-HF etching. The created trench structures are used to overcome the crack formations [41] in  $\text{Si}_3\text{N}_4$  films due to tensile stress [37]. In [Paper A], the crack barriers are not needed for SiRN due to its lower stress than  $\text{Si}_3\text{N}_4$  [61]. After fabrication of crack barriers,  $\text{Si}_3\text{N}_4$  films with different thickness are deposited utilizing a thermal cycling process to reduce the stress [38]. The patterns of waveguides are defined by EBL since EBL can enable small features down to 8 nm and provide relatively good line edge roughness. DUV stepper lithography can also enable ultralow-loss  $\text{Si}_3\text{N}_4$  waveguide [54, 139] while providing high-speed production. However, it's not available in the cleanroom at Chalmers. The patterns of waveguides are transferred into silicon nitride layer by inductively-coupled-plasma reactive-ion etching (ICP RIE) using etchant of  $\text{CHF}_3$  and  $\text{O}_2$ . An RCA clean is applied on the wafer to remove the residual of resist and polymers introduced from ICP RIE. Then, the wafer is annealed at 1200  $^\circ\text{C}$  under Ar ambient for 3 hours to outgas hydrogen. After the annealing process, a combination of LPCVD and PECVD  $\text{SiO}_2$  (with total thickness of  $\sim 2.5 \mu\text{m}$ ) is used due to the trade off between the quality of  $\text{SiO}_2$  films and deposition rate. In the end, microheaters based on Pt are evaporated and patterned on  $\text{SiO}_2$  surface through a lift-off process. The microheaters are made by 5 nm Ti and 200 nm Pt. Thin Ti layer is used to provide a good adhesion layer between  $\text{SiO}_2$  and Pt. Microheaters are commonly used for thermo-optic tuning of refractive index [109, 140]. In [Paper B, E], microheaters were used to initialize DKS microcomb [141]. The typical bandwidth of microheater is around 6-10 kHz depending on the spacing between the microheater and the silicon nitride waveguide.

## 5.2 Silicon nitride thin film deposition

Silicon nitride typically can be deposited by sputtering, PECVD and LPCVD processes. In this thesis, only LPCVD silicon nitride is used because of its superb quality compared with sputtered and PECVD  $\text{Si}_3\text{N}_4$  [142]. Precursor gases dichlorosilane ( $\text{SiH}_2\text{Cl}_2$ ) and ammonia ( $\text{NH}_3$ ) are used to form amorphous  $\text{Si}_3\text{N}_4$  with chemical

reaction as



LPCVD  $\text{Si}_3\text{N}_4$  process involves the following steps: 1) precursor gases  $\text{SiH}_2\text{Cl}_2$  and  $\text{NH}_3$  diffuse from the main gas stream to the wafer surface; 2) precursor gases are adsorbed on the wafer surface; 3) precursor gases migrate and react on the wafer surface; 4) byproducts  $\text{HCl}$  and  $\text{H}_2$  are desorbed from the wafer surface, and are transported away from the wafer. We deposited LPCVD  $\text{Si}_3\text{N}_4$  at  $770^\circ\text{C}$  under pressure of 250 mTorr. The high temperature results in a higher surface reaction rate and more migration in step 3. The enhanced migration on the wafer surface leads to a uniform and conformal deposition [142]. The low pressure during LPCVD process increases the mean free path of the gases and significantly increases the diffusion to the wafer surface compared with atmospheric pressure CVD. These two effects contribute to high uniformity of film thickness across the wafer and conformal coverage. During LPCVD  $\text{Si}_3\text{N}_4$  depositions, Si nano-particles can be introduced due to the pyrolysis of DCS gas under high temperature



Therefore, sufficient  $\text{NH}_3$  gases are needed to assure that the  $\text{NH}_3$  molecules are the predominant adsorbing species on the wafer surface [143], and, consequently, reduce the possibility of the pyrolysis of DCS gas. However, the increased gas flow of  $\text{NH}_3$  can result in enhanced N-H bonds [94], which result in absorption near the wavelength of 1510 nm [92]. Even though high temperature annealing at  $1200^\circ\text{C}$  is commonly used to outgas hydrogen, the residual of N-H bonds are still not negligible [20, 75].  $\text{Si}_3\text{N}_4$  films deposited by LPCVD typically have high stress ( $\sim 1$  GPa) [144], which results in crack formations when the thickness of  $\text{Si}_3\text{N}_4$  film is thicker than 300 nm. The crack formations can easily degrade the yield to a very low level (see section 5.6). One way to overcome this challenge is using SiRN, which features much lower stress than  $\text{Si}_3\text{N}_4$  [37]. In [Paper A], the minimum gases ratio DCS: $\text{NH}_3$  was adopted to deposit 700 nm SiRN without cracks. The thickness of 700 nm was selected for the flexibility of dispersion engineering for both normal and anomalous regime. However, we noticed enhanced waveguide losses, including enhanced absorptive loss, compared with [Paper B]. This can be explained by increased Si clusters [96, 97] originated from pyrolysis of DCS gas [143]. The undesired Si clusters can result in Rayleigh scattering loss and two-photon absorption at wavelength of 1550 nm. Nevertheless, SiRN can still be useful for applications,

### 5.3. Electron beam lithography

---

which don't need ultralow-loss silicon nitride waveguide. In [Paper C], an octave-spanning SCG was achieved in all-normal-dispersion SiRN waveguide, even though the waveguide loss was  $\sim 40$  dB/m.

In order to overcome the crack formation in  $\text{Si}_3\text{N}_4$  thin films, trenches of crack barriers are pre-defined on thermally oxidized Si wafers to arrest cracks [40, 41], which originate from the edge of the wafers. Instead of scribing the wafer surface to create mechanical trenches [41], we use UV lithography to carefully define the patterns of crack barriers. We noticed that the shape of crack barriers highly determines the ability to arrest the cracks, similar to what is discussed in [145].

### 5.3 Electron beam lithography

EBL relies on scanning a focused electron beam on a wafer covered with resist to create the desired patterns. It is convenient to change the designs of devices since EBL is a maskless lithography. EBL exposes the resist shot by shot, therefore the writing time of EBL is linearly proportional to the area of the devices. The writing time ( $t_{on}$ ) of EBL can be estimated by

$$t_{on} = \frac{A_{device}}{L_{BSS}^2 \cdot R_{speed}}, \quad (5.3)$$

where  $L_{BSS}$  is the beam step size (BSS) which is defined by the distance between adjacent shots, and  $R_{speed}$  is the writing speed ( $\sim 100$  MHz in this work, using the Raith 5200 available at Chalmers). The BSS of EBL determines how accurate the e-beam shots are placed and, consequently, determines how accurate the device patterns are exposed. The BSS can be smaller than 1 nm, but the reduced BSS dramatically increases the writing time. According to [146], small BSS and fast writing provide lower waveguide loss. Therefore, once the BSS is determined, the maximum allowed current of EBL should be chosen to meet the maximum  $R_{speed}$ . In [Paper A, B, E], the BSS used for EBL is 2 nm, which provides a good balance between the loss performance of the microresonators and the writing time. In [Paper D], the writing time for a 1.42-meter waveguide is  $\sim 60$  min, even though the BSS was increased to 4 nm. This also explains why 3-meter waveguide design was not chosen. Since EBL precisely exposes the patterns of the devices shot by shot, cautions should be paid on almost every step of EBL. The following discussions will be divided into two parts, 1) strategies within a writing field (WF); 2) strategies for inter-WFs.

### 5.3.1 Within a writing field

The WF of EBL means the maximum field that the electron beam can deflect and expose the resist without moving the sample. The WF can vary from  $160\ \mu\text{m} \times 160\ \mu\text{m}$  to  $1040\ \mu\text{m} \times 1040\ \mu\text{m}$ , depending on the resolution of the WF. The size of microresonators used in [Paper A, B, E] is smaller than the maximum WF, therefore the stitching errors (which will be described in next section) located at the interface of adjacent WFs can be safely avoided. Within a WF, the device pattern should be fractured into trapezoids so that each trapezoid is smaller than the size of a subfield ( $4.5\ \mu\text{m} \times 4.5\ \mu\text{m}$ ). The fracturing of a device pattern is illustrated in Fig. 5.2. The pattern of a microresonator (waveguide width  $2\ \mu\text{m}$ ) is shown in Fig. 5.2a, and it needs to be fractured into trapezoids as illustrated in Fig. 5.2b. However, since large trapezoids with width ranging from 300 nm to 1000 nm are introduced, the problem of 'squaring the circle' (described in section 3.1.2) raises again and introduces excess propagation loss. Fig. 5.2c shows the equivalent loss of SiRN microresonators with different radii, at early stage of this thesis work. Due to undesired fracturing in EBL, much larger losses were observed from the microresonators with smaller radii. Therefore, we need to fracture the pattern of devices (especially curved waveguides) into small trapezoids with width of  $\sim 100\ \text{nm}$ , as depicted in Fig. 5.2d. With improved fracturing method, we observed similar losses from microresonators with different radii. Microresonators with  $\sim\text{THz}$  FSR still feature lower  $Q_i$  compared with the microresonators with FSR of 220 GHz or 100 GHz, but it's mainly as a result of the modified waveguide mode due to small bending radius. It needs to be pointed out that simply fracturing the pattern into small trapezoids is still not enough. Any imperfect fracturing can dramatically degrade the intrinsic  $Q$  of the microresonators. An example is shown in Fig. 5.2e. Although the width of the trapezoids are as small as  $\sim 100\ \text{nm}$ , a small imperfection shows up between trapezoids. We observed that these small imperfections in EBL can significantly degrade  $Q_i$ s of microresonators from  $12 \times 10^6$  to  $5 \times 10^6$ .

Once the patterns are perfectly fractured into trapezoids, the shots of electron beam need to be nicely arranged. The illustration of the arrangement of shots is shown in Fig. 5.3. Each circle in Fig. 5.3b represents a shot of electron beam, and the distance between adjacent shots is 2 nm. As can be seen, the shots are not well arranged especially at the edge of the pattern. The improperly arranged shots can increase the line edge roughness of the resist, which will be transferred into  $\text{Si}_3\text{N}_4$  waveguides and result in undesired sidewall roughness. In order to solve this issue, the 'high resolution mode' function embedded in the so-called Beamer software (GenISys) for

### 5.3. Electron beam lithography

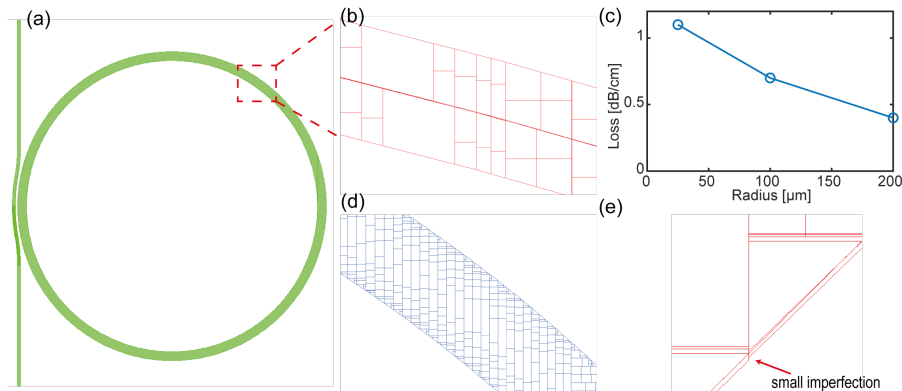


**Figure 5.2:** Illustration of fracturing a microresonator into trapezoids. (a) the pattern of a microresonator. (b) an example of improperly fractured pattern. The trapezoids are too large and result in aliasing. (c) the equivalent loss of SiRN microresonators with different radii. Much larger loss was observed for microresonators with smaller radius, due to improperly fractured pattern. (d) fracturing the pattern into small trapezoids. (e) a small defect in fracturing.

the Raith 5200 was used to improve the arrangement of shots, shown in Fig. 5.3c. As can be seen, a much better arrangement of the shots is achieved at the edge of the pattern. Further improvement of the arrangement of the shots can be achieved by implementing single line edge smoothing strategy [147]. However, this strategy embedded in Beamer software is currently not available for the Raith system.

The above mentioned factors are fundamental and universal in EBL. On the other hand, the EBL system itself can have some imperfections. This includes the noise from the system and environmental sources, the imperfect arrangement of subfields and instability of electron beam [146]. These undesired effects can be reduced by implementing a multipass strategy, where the resist is exposed multiple times to reduce the line edge roughness [146]. In [Paper D], by implementing multipass (2 times) method, the waveguide loss was successfully reduced from 3.4 dB/m to 1.4 dB/m. In [Paper E], we observed an enhanced  $Q_i$  from  $12 \times 10^6$  to  $19 \times 10^6$ , by using this method.

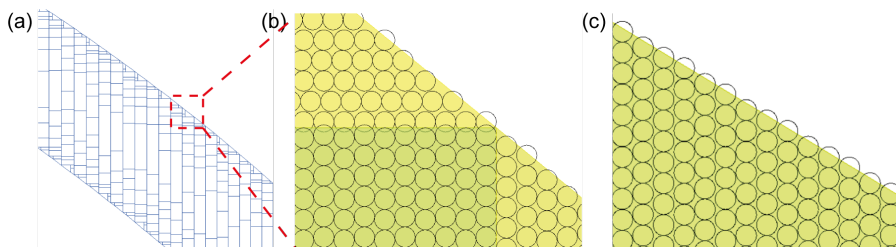


**Figure 5.3:** Illustration of the arrangement of the shots. (a) a fractured pattern. (b) improperly arranged shots. (c) the arrangement of shots using 'high resolution mode'

### 5.3.2 Between writing fields

If the pattern of a device is larger than the size of a WF, multiple WFs must be concatenated to expose the pattern. Stitching errors can show up at the interface between adjacent WFs. The stitching errors are not mainly resulted from the movement of the stage which holds the samples, since the stage position is precisely controlled by a laser interferometer. The stitching errors mainly originate from the imperfect deflection of the electron beam [148]. The origin of stitching error is depicted in Fig. 5.4a. Importantly, this effect is deterministic and repeatable, and therefore can be properly accounted for. In principle, if the deflection of the electron beam was perfectly calibrated, i.e., the calibration of the WF is perfect, then there would not be stitching error as described by the blue solid frames in Fig.5.4a. However, if there was a shrinkage of the WF as illustrated by the red dashed frames, stitching errors with an offset in x direction will be observed. Similarly, as depicted by the green dashed frames, an improperly calibrated rotation of the WF can result in an offset in y direction. The stitching errors that originate from imperfect calibration of the WF are systematic, i.e., the stitching errors are identical at boundaries of all WFs. Apart from systematic errors, stochastic stitching errors are resulted from thermal effect, charging effect and precision of the laser interferometer. In [Paper D], we noticed that the stitching errors are almost identical at boundaries of all WFs, indicating that the stitching errors of our EBL system are dominated by the imperfection of the WF calibration. The representative stitching error is shown in Fig.5.4b. An offset of 50 nm is shown in y direction, and an offset of 14 nm is observed in x direction. These stitching errors are relatively large, and can result in scattering losses. There-

## 5.4. Inductively-coupled-plasma reactive-ion etching

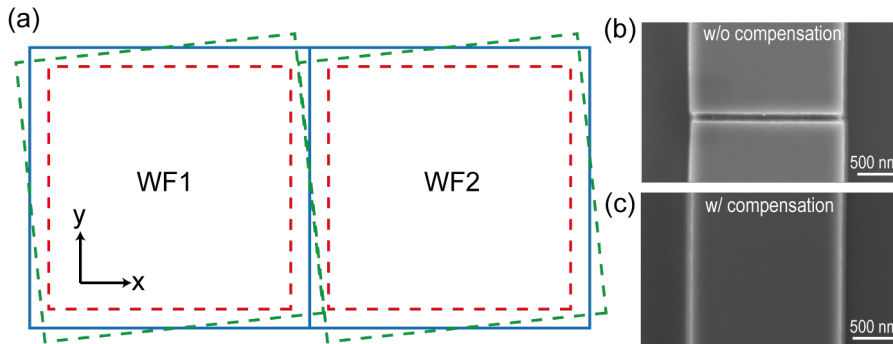


**Figure 5.4:** (a) Illustration of origin of stitching errors. Blue solid frames indicate perfect WFs. The dashed red and green frames indicate shrinkage and rotation of WFs, respectively. (b) SEM image of the resist without stitching error compensation. (c) SEM image of the resist with stitching error compensation.

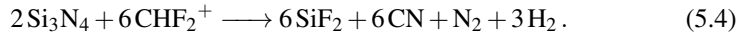
fore, a stitching error compensation process was implemented. The specific values of stitching errors are pre-measured under SEM based on a test sample, then, when fabricating the devices, the adjacent WFs are precisely shifted according to the pre-measured stitching error. The SEM images of the exposed resist with and without stitching error compensation are shown in Fig. 5.4b and c. The resist with stitching error compensation has negligible stitching error. The success of stitching error compensation process was further proved by the OFDR measurement in [Paper D]. This process can be generally applied on EBL when the pattern size is larger than the WF.

## 5.4 Inductively-coupled-plasma reactive-ion etching

Inductively-coupled-plasma reactive-ion etching (ICP RIE) is a dry etching process, which is commonly used to transfer the pattern from the developed resist into the underneath thin films. ICP RIE is typically more anisotropic compared with wet etching. In ICP RIE system, the etchant gases are injected from the top of the etching chamber, and the plasma are generated by applying radio frequency (RF) power on inductive coils. The created plasma includes reactive species ranging from electrons to ions and to radicals [142]. The high RF power applied on inductive coils leads to high density plasma which is chemically reactive with the target material.

These reactions are typically isotropic. The plasma enters the etching chamber, and is accelerated by the DC bias generated by the RF power applied on top and bottom electrodes. The accelerated plasma provides energetic ion bombardment, which is more anisotropic etching.

Si based materials (Si, SiO<sub>2</sub> and Si<sub>3</sub>N<sub>4</sub>) are commonly etched by fluorine-based gases (CHF<sub>3</sub>, CF<sub>4</sub> and NF<sub>3</sub>). In this thesis work, CHF<sub>3</sub> and O<sub>2</sub> gases are used to etch Si<sub>3</sub>N<sub>4</sub>. CHF<sub>3</sub> plasma produces a variety of reactive ions and radicals, e.g., CHF<sub>2</sub><sup>+</sup>, F, CHF<sub>2</sub><sup>-</sup> and F<sup>-</sup> [149]. The negative ions typically don't contribute to the etching process due to the DC bias between the top and bottom electrodes. The reactive ion CHF<sub>2</sub><sup>+</sup> can react with Si<sub>3</sub>N<sub>4</sub> with the highest etch yield shown as [150]



Here, the reaction product SiF<sub>2</sub> and CN are radicals [151], and are volatile compounds which will be exhausted from the chamber. The radical F can react with Si<sub>3</sub>N<sub>4</sub> as [152]



Compared with radical SiF<sub>2</sub>, SiF<sub>4</sub> is more stable, and doesn't decompose to Si formation. Typically, CHF<sub>3</sub> plasma can form C-F polymer layers on the substrate, resist and sidewall of waveguide [153]. These polymer formations not only retard the etching but also introduce nanometer-scale roughness. Therefore, sufficient O<sub>2</sub> is needed to remove polymer formations. Moreover, O<sub>2</sub> and CHF<sub>3</sub> mixture forms more volatile compounds (CO and CO<sub>2</sub>), and, simultaneously, generate more F radicals which react with Si<sub>3</sub>N<sub>4</sub>. However, introducing O<sub>2</sub> dramatically reduces the selectivity (the ratio of the etch rate of Si<sub>3</sub>N<sub>4</sub> to that of resist) between Si<sub>3</sub>N<sub>4</sub> and resist. Therefore, optimizing dry etching recipe of Si<sub>3</sub>N<sub>4</sub> typically means finding a good balance among sidewall roughness, sidewall angle and selectivity.

Fig. 5.5 shows the SEM images of fabricated Si<sub>3</sub>N<sub>4</sub> waveguides at beginning (a), middle (b) and late (c) of this PhD work. As can be seen, the sidewall roughness of Si<sub>3</sub>N<sub>4</sub> waveguides were improved steadily. Fig. 5.5c is the waveguide used in [Paper B]. The SEM images of waveguides in [Paper D, E] look similar to Fig. 5.5c. The main improvement are from implementing multipass in EBL and annealing at 1200 °C under Ar ambient.

## 5.5. SiO<sub>2</sub> cladding deposition

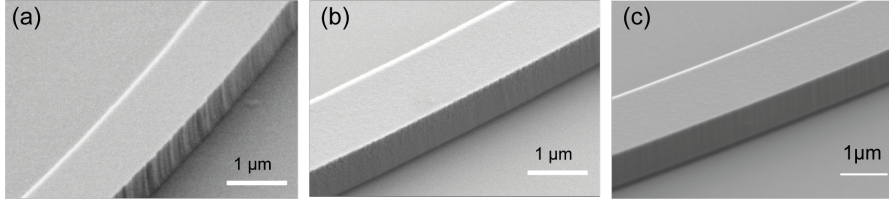
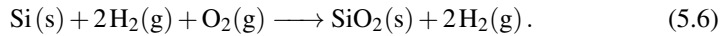


**Figure 5.5:** (a) SEM image of fabricated Si<sub>3</sub>N<sub>4</sub> waveguides at the beginning of this PhD work. (b) SEM image of the fabricated SiRN waveguide used in [Paper A]. (c) SEM image of the Si<sub>3</sub>N<sub>4</sub> in [Paper B].

## 5.5 SiO<sub>2</sub> cladding deposition

In our fabrication of ultralow-loss Si<sub>3</sub>N<sub>4</sub> waveguides, three different types of SiO<sub>2</sub> cladding are used. The bottom cladding is based on thermal oxidation of Si. This process relies on inward diffusion of oxygen into the Si wafer, with reaction shown as



It's also called wet oxidation. The wet oxidation of Si is faster than dry oxidation due to the present of H<sub>2</sub>. However, since both dry and wet oxidation rely on the diffusion process, the growth rate of SiO<sub>2</sub> slows down dramatically once SiO<sub>2</sub> barrier layer is formed on the surface of Si wafers. The growth rate of thermal oxidation follows the Deal-Grove model [154]. At a temperature of 1070 °C, it takes ~20 hours to grow 3 μm thermally oxidized SiO<sub>2</sub>. The cost of thermally oxidized Si wafers are commonly leveraged by loading tens of wafers simultaneously into the oxidization furnace. Thermally oxidized SiO<sub>2</sub> has extremely high quality, and, very recently, greater than 10<sup>9</sup> Q<sub>i</sub> (corresponding to propagation loss of 0.025 dB/m) was achieved in SiO<sub>2</sub> wedge microresonators [155]. Considering the state of the art of high-confinement Si<sub>3</sub>N<sub>4</sub> waveguide loss (1 dB/m), the material loss of thermally oxidized SiO<sub>2</sub> can be safely neglected for high-confinement Si<sub>3</sub>N<sub>4</sub> waveguides.

As depicted in step XII in Fig. 5.1, a layer of LPCVD SiO<sub>2</sub> is deposited on Si<sub>3</sub>N<sub>4</sub> waveguides. Here, LPCVD SiO<sub>2</sub> relies on the pyrolysis of tetraethyl orthosilicate (TEOS) at elevated temperature (> 600°C), with reaction shown as



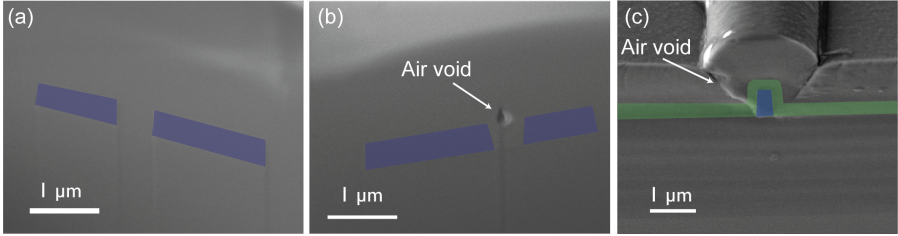


**Figure 5.6:** (a) SEM image of the cross section of the coupling region of a microresonator after FIB milling. The top  $\text{SiO}_2$  cladding is deposited by LPCVD. (b) idem to (a), but the top cladding is deposited by PECVD. (c) SEM image of the cleaved chip facet.  $\text{Si}_3\text{N}_4$  and LPCVD  $\text{SiO}_2$  are highlighted by blue and green colors, respectively.

In this thesis work, LPCVD  $\text{SiO}_2$  was deposited at  $710^\circ\text{C}$  under pressure of 250 mTorr. Here, the effect of low pressure and high temperature lead to conformal deposition, which is described in section (5.2). The conformal deposition contributes to nicely filled gap between bus and ring waveguides. This is extremely important for microresonators since imperfections in the coupling region could result in undesired scattering loss. A focused-ion beam (FIB) milling was applied on the coupling region of a microresonator clad by LPCVD  $\text{SiO}_2$ , and its SEM image is shown in Fig. 5.6a. The  $\text{Si}_3\text{N}_4$  waveguides are highlighted in blue. The height of the waveguide is 730 nm, and the gap between bus and ring waveguide is 350 nm. As can be seen, no air void is observed thanks to the conformal deposition of LPCVD  $\text{SiO}_2$ . We anneal the wafer after depositing LPCVD  $\text{SiO}_2$  on  $\text{Si}_3\text{N}_4$  waveguides. According to our comparative studies, by annealing LPCVD  $\text{SiO}_2$ , the  $Q_i$  of  $\text{Si}_3\text{N}_4$  microresonators can be enhanced from  $7 \times 10^6$  to  $11 \times 10^6$ , compared with the control wafer. This huge improvement can be explained by two factors. Firstly, the as-deposit LPCVD  $\text{SiO}_2$  films are a bit porous, and need to be densified by annealing at temperatures between  $1000$  and  $1150^\circ\text{C}$  [156]. This is consistent with our observations that annealed LPCVD  $\text{SiO}_2$  thin films feature a reduced thickness  $\sim 10\%$  and increased refractive index approaching that of thermally oxidized  $\text{SiO}_2$ . Secondly, by annealing LPCVD  $\text{SiO}_2$ , a gradient refractive index is created at the interface between  $\text{Si}_3\text{N}_4$  and  $\text{SiO}_2$  through interdiffusion [34]. The gradient refractive index could reduce the index contrast at the interface, which in turn reduces the scattering loss due to sidewall roughness [86, 87]. The quality of LPCVD  $\text{SiO}_2$  based on TEOS rivals the quality of

## 5.5. SiO<sub>2</sub> cladding deposition

---

thermally oxidized SiO<sub>2</sub> [156]. Recently, ultra-high Q microresonators, approaching 422 million (equivalent loss of  $\sim 0.06$  dB/m) [20, 21], were achieved in low confinement Si<sub>3</sub>N<sub>4</sub> waveguides. For these devices, thick LPCVD SiO<sub>2</sub> layers are used. Considering low confinement nature of these Si<sub>3</sub>N<sub>4</sub> waveguides, it indirectly indicates that LPCVD SiO<sub>2</sub> has very low material loss. The deposition rate of LPCVD SiO<sub>2</sub> is typically around 8 nm/min. Therefore, it's time consuming and expensive to deposit thick LPCVD SiO<sub>2</sub>. In this thesis work, since high-confinement Si<sub>3</sub>N<sub>4</sub> waveguides are used, only  $\sim 500$  nm LPCVD SiO<sub>2</sub> is deposited on Si<sub>3</sub>N<sub>4</sub> waveguides. PECVD SiO<sub>2</sub> is used to reach the target thickness of top cladding layer. PECVD SiO<sub>2</sub> is deposited at much lower temperature (300 °C) compared to LPCVD SiO<sub>2</sub>. Therefore, it adds less restrictions on the materials that a wafer contains. Typically, the precursor gases SiH<sub>4</sub> and N<sub>2</sub>O are used to deposit SiO<sub>2</sub>. The reaction is elevated by the highly reactive chemical species created by the inductively coupled plasma, and the deposition rate of PECVD is much higher than that of LPCVD. However, due to the relatively high pressure (550 mTorr) and relatively low temperature compared to LPCVD, the ability of step coverage is much poorer than LPCVD. An FIB milling was applied to the coupling region of a microresonator clad by PECVD SiO<sub>2</sub>. Its SEM image is shown in Fig.5.6b. The height of the waveguide is 700 nm, and the gap between bus and ring waveguide is 350 nm. A clear air void was observed at the coupling region due to poor step coverage. In fact, when the sidewall angle of the waveguide is close to 90°, PECVD SiO<sub>2</sub> is not even good to clad an isolated waveguide. An SEM of cleaved chip facet is shown in Fig. 5.6c. The Si<sub>3</sub>N<sub>4</sub> waveguide and the LPCVD SiO<sub>2</sub> layer are highlighted in blue and green colors, respectively. As can be seen, the LPCVD SiO<sub>2</sub> deposition is very conformal, while PECVD SiO<sub>2</sub> cannot cover an isolated waveguide nicely. Air voids are observed at both left and right sides of the waveguide. At the input and the output of devices, the mode size of the waveguides are commonly designed [73] to match the spot size of the lensed fiber, e.g., diameter of 2.5  $\mu$ m. At this regime, the undesired air voids can not only scatter light, but also modify the mode size of the waveguides which is ideally designed for specific coupling fiber. This issue should be solved by planarizing the wafer surface by chemical mechanical polishing (CMP) prior to PECVD SiO<sub>2</sub> deposition. Of course, simply depositing thicker LPCVD SiO<sub>2</sub> could also solve this problem.

## 5.6 Analysis of fabrication yield

While high-Q microresonators were reported in high-confinement  $\text{Si}_3\text{N}_4$  microresonators [41, 48, 157], it's common that a single isolated resonance with highest  $Q_i$  is shown and reported. Only very recently, high Q, based on more statistical analysis of all measured resonances from multiple microresonators, are reported in [50, 54, 139] [Paper B, E]. The statistical analysis is beneficial to avoid undesired errors from measurements and data fitting. However, it's still insufficient to evaluate the yield of nano-fabrications since microresonators typically only occupy small device areas. For example, a  $\text{Si}_3\text{N}_4$  microresonator (waveguide width  $2\ \mu\text{m}$ ) with FSR of 100 GHz (with a radius of  $\sim 227\ \mu\text{m}$ ) only has a device area of  $0.003\ \text{mm}^2$ . In fact, devices with large device area are more suitable for yield analysis. In [Paper D], we reported 60% yield of 1.42-meter-long defect-free  $\text{Si}_3\text{N}_4$  waveguides (waveguide width  $2\ \mu\text{m}$ , device area is  $2.84\ \text{mm}^2$  for each waveguide). We measured 20  $\text{Si}_3\text{N}_4$  waveguides with lengths of 1.42 meter, among which 12 waveguides are defect-free according to OFDR measurements. The mean propagation loss of defect-free waveguides is 1.7 dB/m. In fact, for photonic integration, it's irrational to simply report yield by calculating the ratio of the number of working devices to total number of devices. There are two reasons. Firstly, the device area of photonics devices can vary from tens of  $\mu\text{m}^2$  to few  $\text{mm}^2$ . A device with larger area typically results in lower yield. Secondly, it's challenging to assemble different devices after a completed fabrication process, i.e., it's difficult to firstly fabricate 20 pieces of 10 cm waveguides, then pick and assemble 10 pieces of perfect 10 cm waveguides to obtain a 1-meter-long waveguide. Based on these two factors, it's clear that we need to define a photonics yield parameter that is normalized to a unit area of the device. Here,  $R_{mm}$  is defined as the photonics yield parameter for unit  $\text{mm}^2$  device area. Then, the yield can be calculated by

$$Y = R_{mm}^{A_{device}/(1\text{mm}^2)}, \quad (5.8)$$

where  $Y$  is yield, and  $A_{device}$  is the area of a device. To exemplify Eq. 5.8, the values from [Paper D] ( $Y=0.6$ ,  $A_{device}=2.84\ \text{mm}^2$ ) are used. Then,  $R_{mm}$  is calculated to be 0.84. With calculated  $R_{mm}$ , we can calculate the yield for aforementioned  $\text{Si}_3\text{N}_4$  microresonator (waveguide width  $2\ \mu\text{m}$ ) with FSR of 100 GHz. The yield is as high as 99.98%! Even for microresonators with FSR as low as 1 GHz, the calculated yield is still as high as 97.54%. This means hundreds of 1 GHz microresonators need to be evaluated in order to rigidly report  $R_{mm}$  approaching 0.8. With the above analysis, it is clear that microresonators are unsuitable for analyzing fabrication yield, especially

## 5.6. Analysis of fabrication yield

---

when  $R_{mm}$  is relatively high. Nevertheless, characterization based on microresonators is still a good method to evaluate equivalent waveguide loss, which gives insight into the fabrication techniques.

In section 4.2, according to the simulation result, a  $\text{Si}_3\text{N}_4$  waveguide (with loss 1.4 dB/m) with length longer than 3 meter should be used for an OPA. However, only 1.42-meter waveguides were used in [Paper D]. One reason is the fabrication yield. Based on  $R_{mm}=0.84$ , the yield of 3-meter waveguides would be further reduced to 36%. In our fabrication process, the main yield killers are in process step II, III and VIII described in Fig. 5.1. In step II, due to small defects of photoresist, some surface may not be fully covered by photoresist. Then, in step III, HF can penetrate through these defects and etch the  $\text{SiO}_2$  layer creating small holes. Large propagation loss can be observed as long as the waveguide pass through a single hole. In order to solve this, thicker photoresist or hard mask should be used in step II. In step VIII, the imperfection of the resist can also result in large propagation loss in waveguides. Moreover, we have had a serious issue with nano-particle contamination in the MaN-2405 resist provided by the supplier since 2019.



## Chapter 6

# Summary and future outlook

This thesis work presents a steadily reduced loss in high confinement  $\text{Si}_3\text{N}_4$  waveguides owing to optimization of fabrication flow, lithography and dry etching. The properly designed ultralow-loss  $\text{Si}_3\text{N}_4$  waveguides enabled generation of DKS microcombs with repetition rates ranging from 1 THz to 14 GHz, while limiting the footprint of the devices within  $1\text{ mm}^2$ . The high yield of the fabrication allows us to attain high confinement meter-long  $\text{Si}_3\text{N}_4$  waveguides with a record-low loss of 1.4 dB/m. Thanks to these ultralow-loss  $\text{Si}_3\text{N}_4$  waveguides, a CW-pumped optical parametric amplifier is achieved in a Kerr nonlinear waveguide for the first time. However, similar as steadily boosted density of transistors in integrated circuits, urges to attain better performance of integrated photonics devices never stop. Optical waveguide, the most fundamental component of photonic integration, deserves endless efforts. Further improvements are envisioned.

In [Paper E], a multipass EBL significantly enhanced the  $Q_i$  from  $12 \times 10^6$  to  $19 \times 10^6$ . This indicates the current lithography is still far from perfect. Additionally, since the waveguide loss is approaching 1 dB/m, the scattering loss induced from the surface roughness of  $\text{Si}_3\text{N}_4$  becomes non-negligible [48]. Therefore, a CMP process should be applied on the deposited film to further reduce the surface roughness.

Improvements in scattering losses also call for a refinement in the diagnostic tools. In this thesis, the sidewall roughness of waveguides are qualitatively inspected by SEM, and the quantitative evaluation based on image signal processing is reaching its limitation. More refined approaches based on AFM would be required.

Last but not least, improving the coupling loss is important. For an OPA, the coupling loss directly degrades the achievable NF. Dry etching or facet polishing should be used to attain smooth chip facets. The air voids due to poor coverage of PECVD  $\text{SiO}_2$  need to be solved by applying CMP prior to PECVD deposition. Moreover, by implementing three dimensional integration of thin  $\text{Si}_3\text{N}_4$  [22, 158], ultralow coupling loss between a waveguide and a single mode fiber can be achieved [159]. In addition to improving coupling losses, this 3D integration approach would allow for the realization of heterogeneous integration with active optical components.

## Chapter 7

# Summary of papers

### Paper A

**"Low-loss high-Q silicon-rich silicon nitride microresonators for Kerr nonlinear optics"**, *Opt. Lett.* vol. 44, no. 13, pp. 3326-3329 (2019).

In this paper, we used the minimum ratio between precursor gases DCS:NH<sub>3</sub> to deposit crack-free SiRN thin films with thickness of 700 nm, which allow flexible dispersion engineering. We successfully outgas hydrogen from the SiRN film, and achieved low loss ( $\sim 40$  dB/m) in SiRN platform. Low-noise microcombs with repetition rate of 220 GHz and 1THz were achieved in SiRN platform for the first time.

**My contributions:** I developed the fabrication recipe, designed and fabricated the devices. I characterized the devices and did microcomb experiments with support from the co-authors. I wrote the paper with support from the co-authors, and presented the results at CLEO in San Jose, USA in 2018.

## Paper B

**"High-Q Si<sub>3</sub>N<sub>4</sub> microresonators based on a subtractive processing for Kerr nonlinear optics"**, Opt. Express vol. 27, no. 24, pp. 35719-35727 (2019).

In this paper, mean intrinsic  $Q > 11 \times 10^6$  was achieved in dispersion-engineered Si<sub>3</sub>N<sub>4</sub> microresonators. Such high-Qs allowed us to generate 100 GHz soliton microcomb for the first time in Si<sub>3</sub>N<sub>4</sub> microresonators fabricated using a subtractive processing method. High performance mode-locked dark-pulse microcomb was generated in a Si<sub>3</sub>N<sub>4</sub> microresonator with intrinsic  $Q > 10^7$  for the first time.

**My contributions:** I developed the fabrication recipe, designed and fabricated the devices. I characterized the devices with support from the co-authors. I did microcomb experiments. I wrote the paper with support from the co-authors, and presented part of the results at CLEO 2020.

## Paper C

**"Octave-spanning frequency comb generation in all-normal-dispersion silicon-rich silicon nitride waveguide"**, in Conference on Lasers and Electro-Optics (CLEO), San Jose, USA, paper. STu3H.7, May 2020.

In this work, we used an all-normal-dispersion SiRN waveguide to achieve coherent octave-spanning supercontinuum. It's the first octave-spanning supercontinuum generation in an all-normal-dispersion nanophotonic waveguide.

**My contributions:** I assisted with device design, supercontinuum generation experiment and paper writing. I fabricated the devices.

---

## Paper D

**"Low-noise continuous-wave-pumped parametric amplifier using a silicon-nitride waveguide"**, Manuscript submitted 2021.

In this paper, we achieved 1.42-meter-long high confinement  $\text{Si}_3\text{N}_4$  waveguides with record-low loss of 1.4 dB/m. Active stitching error compensation was implemented in EBL. Based on these ultralow-loss  $\text{Si}_3\text{N}_4$  waveguides, we achieved CW-pumped optical parametric amplifiers, for the first time, in an integrated Kerr nonlinear waveguide. We developed the theory of NF for lossy phase-sensitive amplifier.

**My contributions:** I developed the fabrication recipe, designed and fabricated the devices. I characterized the devices, performed parametric amplification experiments and wrote the manuscript with co-authors.

## Paper E

**Integrated, ultra-compact high-Q silicon nitride microresonators for low-repetition-rate soliton microcombs"**, Manuscript submitted 2021.

In this paper, we achieved soliton microcomb with repetition rate down to 14 GHz for the first time in  $\text{Si}_3\text{N}_4$  microresonators fabricated using a subtractive processing method. The optimized designs of finger- and snail-shaped microresonators not only allowed us to attain low-repetition-rate soliton microcombs, but also reduced the footprint of the devices by an order of magnitude to  $\sim 1 \text{ mm}^2$ . The statistical intrinsic Q reaches  $19 \times 10^6$ , allowing us to overcome the challenge of dealing with increased cavity volumes.

**My contributions:** I designed, fabricated and characterized the devices. I did microcomb generation and locking experiments with co-authors. I wrote the manuscript with co-authors, and I presented the preliminary results at CLEO 2020.

## Paper F

**"Optical Dual-Comb Vernier Division of an Octave-Spanning Kerr Microcomb"**,  
To be presented in CLEO 2021.

In this work, two soliton microcombs with repetition rate of  $\sim 900$  GHz are generated in two  $\text{Si}_3\text{N}_4$  microresonator with same pump laser. The repetition rate of two soliton microcombs are offset by  $\sim 20$  GHz. Vernier dual-comb frequency division is used to measure the repetition rate of two soliton microcombs.

**My contributions:** I fabricated the devices. I assisted with the device design and soliton microcomb generation.

# Appendices

## Appendix A- Adiabatic bend solver

The adiabatic bend using the algorithm of minimization of the variation of the curvature [83] needs to be solved numerically since Eq. 3.3 and 3.4 do not have analytical expressions. Here, solving S bend for an Archimedean spiral (In polar coordinate,  $r=R+A \cdot \phi$ , where  $R$  is the radius at start point,  $\phi$  is angle.) is taken as an example. Firstly, the expressions of the position, the tangent, the curvature and the change of the curvature of an Archimedean spiral are, respectively, as following

$$(x, iy) = ((R + A\phi) \cdot \cos\phi, i \cdot (R + A\phi) \cdot \sin\phi) \quad (7.1)$$

$$\tan(\theta) = \frac{A \cdot \sin\phi + (R + A\phi)\cos\phi}{A \cdot \cos\phi - (R + A\phi) \cdot \sin\phi} \quad (7.2)$$

$$\kappa(\phi) = \frac{2A^2 + R^2 + A^2\phi^2 + 2RA\phi}{(A^2 + R^2 + A^2\phi^2 + 2RA\phi)^{1.5}} \quad (7.3)$$

$$\frac{d\kappa(\phi)}{ds} = \frac{-(A^2\phi + AR) \cdot (A^2\phi^2 + 2AR\phi + 4A^2 + R^2)}{(R^2 + A^2 + A^2\phi^2 + 2RA\phi)^3} \quad (7.4)$$

The position  $(x_1, iy_1)$ , the tangent  $(\theta_1)$ , the curvature  $(\kappa_1)$  and the change of the curvature  $(\kappa'_1)$  at the start point of the spiral ( $\phi=0$ ) need to be used as boundary condition for the adiabatic bend.

Then we can start to solve the adiabatic bend  $\kappa(s) = a_0 + a_1s + a_2s^2 + a_3s^3$ . The unknown parameters are the start position  $(x_0, iy_0)$ ,  $\theta_0$  (the tangent of the curve at the start point),  $a_0$ ,  $a_1$ ,  $a_2$ ,  $a_3$  and  $s_1$  (the total length of the bend). The start point of the adiabatic bend is the center of the S bend. Since the S bend features rotational symmetry, we only need to solve half of the S bend. The start position can be set to

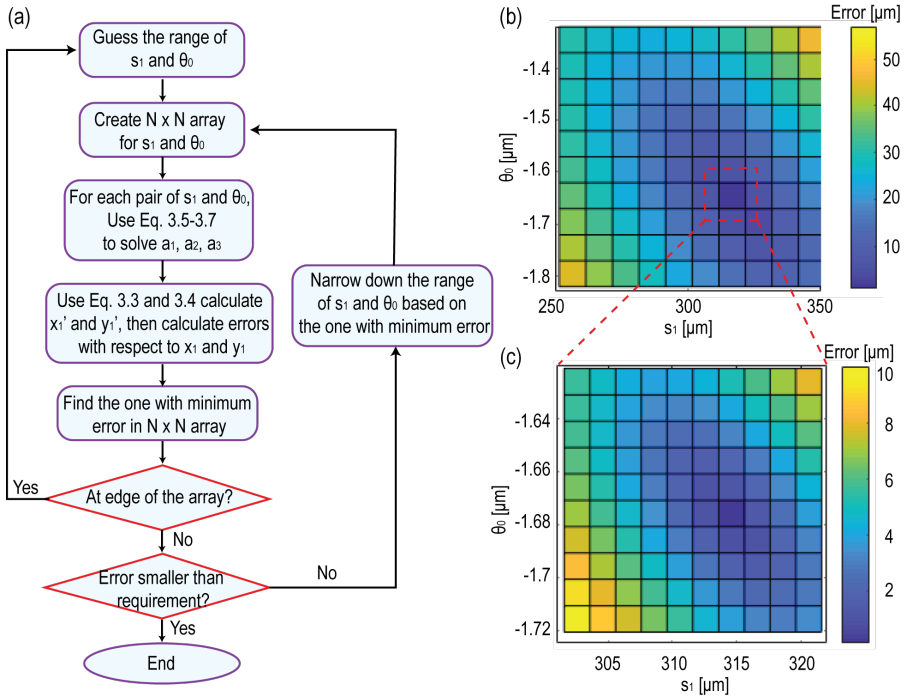


**Figure 7.1:** (a) Flow chart of the bend solver. (b) The error array ( $10 \times 10$ ) for the initial ranges of  $s_1$  and  $\theta_0$ . (c) The error array after narrowing down one time the range of  $s_1$  and  $\theta_0$

(0,0). The curvature of the bend at the start position should be zero ( $a_0=0$ ) since it's connecting two rotational symmetric curve. Therefore, the unknowns are  $\theta_0$ ,  $a_1$ ,  $a_2$ ,  $a_3$  and  $s_1$ . They can be solved based on five equations Eq. 3.3-3.7. Since the only challenging equations are Eq. 3.3 and 3.4. We can solve the equations by sweeping two parameters, for example  $s_1$  and  $\theta_0$ . We need to initially guess the ranges for  $s_1$  and  $\theta_0$ , and we create a N by N array. Then we can solve the equations following the flow chart as shown in Fig. 7.1 Typically, the requirement for the error between  $(x_1, iy_1)$  and  $(x'_1, iy'_1)$  is smaller than 0.1 nm, and it takes less than 10 loops to accurately solve the equations.

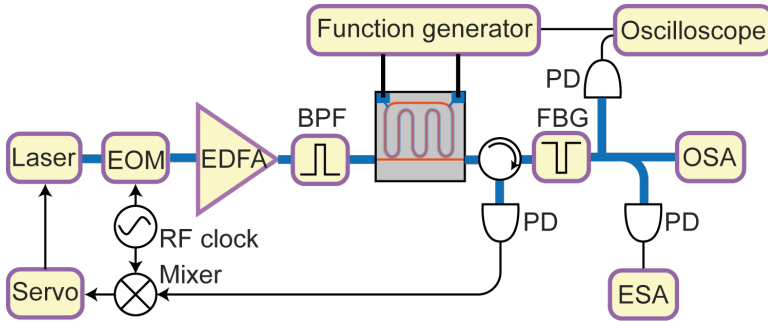


**Figure 7.2:** The setup of soliton microcomb experiment with PDH locking. EOM, electro-optic modulator; BPF, optical bandpass filter; FBG, fiber Bragg grating; OSA, optical spectrum analyzer; PD, photodiode.

## Appendix B- Tips for high power coupling

When coupling a high optical power into a waveguide, the lensed fiber can be bent due to thermal effect. The coupling between the lensed fiber and the waveguide can be very unstable. Few tips are provided to stabilize the coupling.

1. The lensed fiber should be firmly attached on the translation arm by a clamp or glue.
2. The free hanging part of the lensed fiber should be as short as possible.
3. Optimizing the yaw and the pitch of the lensed fiber not only reduces the coupling loss, but also enhances the stability of the lensed fiber.
4. Fix everything firmly, including the 3-axis stages and the chip.

With all above tips, it's possible to have stable coupling that only varies within 0.1 dB in 30 min.

## Appendix C- Initialization of soliton microcombs

The setup used for soliton microcombs experiment with PDH locking is shown in Fig. 7.2. The soliton microcomb is initialized by the microheater on chip. The flow chart of initializing soliton microcomb is shown in Fig. 7.3.

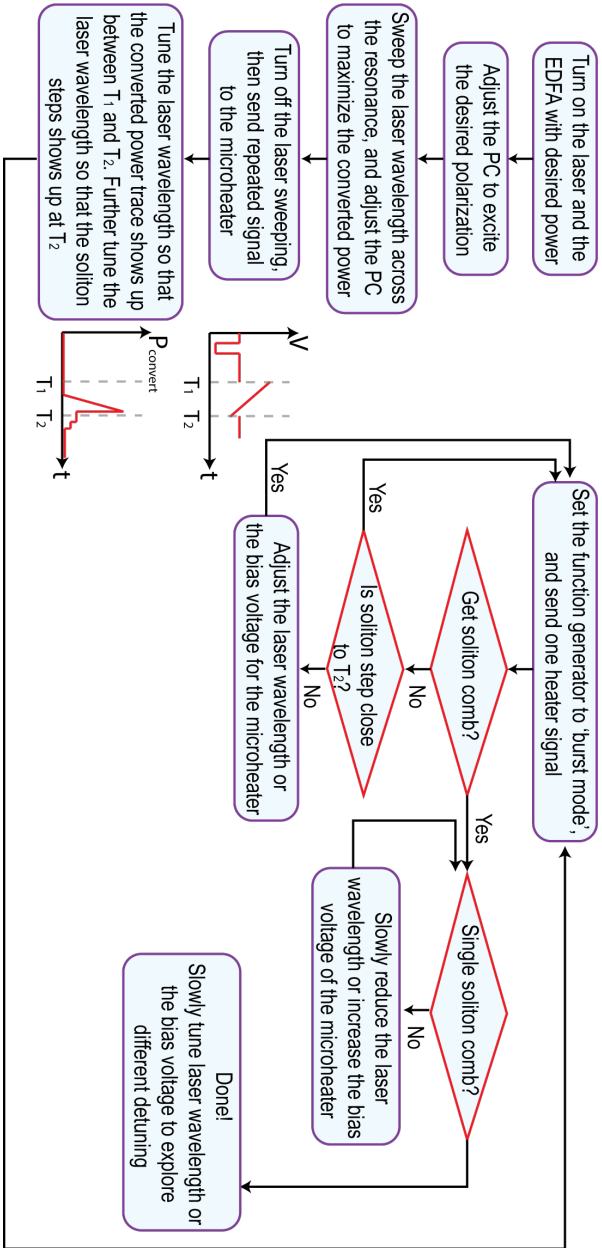


Figure 7.3: Flow chart of bright soliton microcomb initialization. PC, polarization controller.

# Bibliography

- [1] J. Summers, T. Vallaitis, P. Evans, M. Ziari, P. Studenkov, M. Fisher, J. Sena, A. James, S. Corzine, D. Pavinski, J. Ou-Yang, M. Missey, D. Gold, W. Williams, M. Lai, D. Welch, and F. Kish, “Monolithic InP-based coherent transmitter photonic integrated circuit with 2.25 Tbit/s capacity,” *Electronics Letters*, vol. 50, no. 16, pp. 1150–1152, 2014.
- [2] C. R. Doerr, “Silicon photonic integration in telecommunications,” *Frontiers in Physics*, vol. 3, pp. 1–16, 2015.
- [3] R. Soref and J. Lorenzo, “All-silicon active and passive guided-wave components for  $\lambda = 1.3$  and  $1.6 \mu\text{m}$ ,” *IEEE Journal of Quantum Electronics*, vol. 22, no. 6, pp. 873–879, 1986.
- [4] G. T. Reed, G. Mashanovich, F. Y. Gardes, and D. J. Thomson, “Silicon optical modulators,” *Nature Photonics*, vol. 4, no. 8, pp. 518–526, 2010.
- [5] Y. A. Vlasov and S. J. McNab, “Losses in single-mode silicon-on-insulator strip waveguides and bends,” *Optics Express*, vol. 12, no. 8, pp. 1622–1631, 2004.
- [6] M. A. Tran, D. Huang, T. Komljenovic, J. Peters, A. Malik, and J. E. Bowers, “Ultra-low-loss silicon waveguides for heterogeneously integrated silicon/III-V photonics,” *Applied Sciences (Switzerland)*, vol. 8, no. 7, 2018.
- [7] “Photonic Integrated Circuits | imec,” <https://www.imec-int.com/en/what-we-offer/ic-link/photonic-integrated-circuits>.
- [8] Z. Fang, Q. Y. Chen, and C. Z. Zhao, “A review of recent progress in lasers on silicon,” *Optics and Laser Technology*, vol. 46, no. 1, pp. 103–110, 2013.

- 
- [9] D. Liang and J. E. Bowers, "Recent progress in lasers on silicon," *Nature Photonics*, vol. 4, no. 8, pp. 511–517, 2010.
- [10] C. Monat and Y. Su, "Hybrid photonics beyond silicon," *APL Photonics*, vol. 5, no. 2, p. 020402, 2020.
- [11] Y. H. Xie, K. L. Wang, and Y. C. Kao, "An investigation on surface conditions for Si molecular beam epitaxial (MBE) growth," *Journal of Vacuum Science & Technology A: Vacuum, Surfaces, and Films*, vol. 3, no. 3, pp. 1035–1039, 1985.
- [12] E. Yamaichi, T. Ueda, Q. Gao, C. Yamagishi, and M. Akiyama, "Method to obtain low-dislocation-density regions by patterning with SiO<sub>2</sub> on GaAs/Si followed by annealing," *Japanese Journal of Applied Physics*, vol. 33, no. 10B, pp. 1442–1444, 1994.
- [13] K. Samonji, H. Yonezu, Y. Takagi, K. Iwaki, N. Ohshima, J. K. Shin, and K. Pak, "Reduction of threading dislocation density in InP-on-Si heteroepitaxy with strained short-period superlattices," *Applied Physics Letters*, vol. 69, no. 1, pp. 100–102, 1996.
- [14] D. Liang and J. E. Bowers, "Highly efficient vertical outgassing channels for low-temperature InP-to-silicon direct wafer bonding on the silicon-on-insulator substrate," *Journal of Vacuum Science & Technology B: Microelectronics and Nanometer Structures*, vol. 26, no. 4, p. 1560, 2008.
- [15] D. Liang, G. Roelkens, R. Baets, and J. E. Bowers, "Hybrid integrated platforms for silicon photonics," *Materials*, vol. 3, no. 3, pp. 1782–1802, 2010.
- [16] D. Huang, M. A. Tran, J. Guo, J. Peters, T. Komljenovic, A. Malik, P. A. Morton, and J. E. Bowers, "High-power sub-kHz linewidth lasers fully integrated on silicon," *Optica*, vol. 6, no. 6, pp. 745–752, 2019.
- [17] M. Zhang, C. Wang, R. Cheng, A. Shams-Ansari, and M. Loncar, "Monolithic ultrahigh-Q lithium niobate microring resonator," *Optica*, vol. 4, no. 12, pp. 1536–1537, 2017.
- [18] C. Wang, M. Zhang, X. Chen, M. Bertrand, A. Shams-Ansari, S. Chandrasekhar, P. Winzer, and M. Lončar, "Integrated lithium niobate

## Bibliography

---

- electro-optic modulators operating at CMOS-compatible voltages,” *Nature*, vol. 562, no. 7725, pp. 101–104, 2018.
- [19] M. He, M. Xu, Y. Ren, J. Jian, Z. Ruan, Y. Xu, S. Gao, S. Sun, X. Wen, L. Zhou, L. Liu, C. Guo, H. Chen, S. Yu, L. Liu, and X. Cai, “High-performance hybrid silicon and lithium niobate Mach–Zehnder modulators for 100 Gbit/s<sup>-1</sup> and beyond,” *Nature Photonics*, vol. 13, no. 5, pp. 359–364, 2019.
- [20] M. W. Puckett, K. Liu, N. Chauhan, Q. Zhao, N. Jin, H. Cheng, J. Wu, R. O. Behunin, P. T. Rakich, K. D. Nelson, and D. J. Blumenthal, “422 Million intrinsic quality factor planar integrated all-waveguide resonator with sub-MHz linewidth,” *Nature Communications*, vol. 12, no. 1, p. 934, 2021.
- [21] W. Jin, Q.-F. Yang, L. Chang, B. Shen, H. Wang, M. A. Leal, L. Wu, M. Gao, A. Feshali, M. Paniccia, K. J. Vahala, and J. E. Bowers, “Hertz-line-width semiconductor lasers using CMOS-ready ultra-high-Q microresonators,” *Nature Photonics*, 2021, <https://doi.org/10.1038/s41566-021-00761-7>.
- [22] W. D. Sacher, J. C. Mikkelsen, P. Dumais, J. Jiang, D. Goodwill, X. Luo, Y. Huang, Y. Yang, A. Bois, P. G.-Q. Lo, E. Bernier, and J. K. S. Poon, “Tri-layer silicon nitride-on-silicon photonic platform for ultra-low-loss crossings and interlayer transitions,” *Optics Express*, vol. 25, no. 25, pp. 30 862–30 875, 2017.
- [23] D. J. Moss, R. Morandotti, A. L. Gaeta, and M. Lipson, “New CMOS-compatible platforms based on silicon nitride and Hydex for nonlinear optics,” *Nature Photonics*, vol. 7, no. 8, pp. 597–607, 2013.
- [24] W. Stutius and W. Streifer, “Silicon nitride films on silicon for optical waveguides,” *Applied Optics*, vol. 16, no. 12, pp. 3218–3222, 1977.
- [25] J. S. Levy, A. Gondarenko, M. A. Foster, A. C. Turner-Foster, A. L. Gaeta, and M. Lipson, “CMOS-compatible multiple-wavelength oscillator for on-chip optical interconnects,” *Nature Photonics*, vol. 4, no. 1, pp. 37–40, 2010.
- [26] D. J. B. Michael Belt, Michael L. Davenport, John E. Bowers, “Ultra-low-loss Ta<sub>2</sub>O<sub>5</sub>-core/SiO<sub>2</sub> -clad planar waveguides on Si substrates,” *Optica*, vol. 4, no. 5, pp. 2–6, 2017.

- [27] H. Jung, C. Xiong, K. Y. Fong, X. Zhang, and H. X. Tang, "Optical frequency comb generation from aluminum nitride microring resonator," *Optics Letters*, vol. 38, no. 15, pp. 2810–2813, 2013.
- [28] X. Liu, C. Sun, B. Xiong, L. Wang, J. Wang, Y. Han, Z. Hao, H. Li, Y. Luo, J. Yan, T. Wei, Y. Zhang, and J. Wang, "Integrated High- Q Crystalline AlN Microresonators for Broadband Kerr and Raman Frequency Combs," *ACS Photonics*, vol. 5, no. 5, pp. 1943–1950, 2018.
- [29] M. R. Lamont, B. Luther-Davies, D.-Y. Choi, S. Madden, X. Gai, and B. J. Eggleton, "Net-gain from a parametric amplifier on a chalcogenide optical chip," *Optics Express*, vol. 16, no. 25, pp. 20 374–20 381, 2008.
- [30] R. Neo, J. Schröder, Y. Paquot, D.-Y. Choi, S. Madden, B. Luther-Davies, and B. J. Eggleton, "Phase-sensitive amplification of light in a  $\chi^{(3)}$  photonic chip using a dispersion engineered chalcogenide ridge waveguide," *Optics Express*, vol. 21, no. 7, pp. 7926–7933, 2013.
- [31] M. Pu, H. Hu, L. Ottaviano, E. Semenova, D. Vukovic, L. K. Oxenløwe, and K. Yvind, "Ultra-Efficient and Broadband Nonlinear AlGaAs-on-Insulator Chip for Low-Power Optical Signal Processing," *Laser and Photonics Reviews*, vol. 12, no. 12, p. 1800111, 2018.
- [32] L. Chang, W. Xie, H. Shu, Q. F. Yang, B. Shen, A. Boes, J. D. Peters, W. Jin, C. Xiang, S. Liu, G. Moille, S. P. Yu, X. Wang, K. Srinivasan, S. B. Papp, K. Vahala, and J. E. Bowers, "Ultra-efficient frequency comb generation in AlGaAs-on-insulator microresonators," *Nature Communications*, vol. 11, no. 1, pp. 1–8, 2020.
- [33] J. Liu, G. Huang, R. N. Wang, J. He, A. S. Raja, T. Liu, N. J. Engelsen, and T. J. Kippenberg, "High-yield wafer-scale fabrication of ultralow-loss, dispersion-engineered silicon nitride photonic circuits," *arXiv:2005.13949*, 2020.
- [34] J. F. Bauters, M. J. R. Heck, D. D. John, J. S. Barton, C. M. Bruinink, A. Leinse, R. G. Heideman, D. J. Blumenthal, and J. E. Bowers, "Planar waveguides with less than 0.1 dB/m propagation loss fabricated with wafer bonding," *Optics Express*, vol. 19, no. 24, p. 24090, 2011.

## Bibliography

---

- [35] M.-C. Tien, J. F. Bauters, M. J. R. Heck, D. J. Blumenthal, and J. E. Bowers, "Ultra-low loss  $\text{Si}_3\text{N}_4$  waveguides with low nonlinearity and high power handling capability," *Optics Express*, vol. 18, no. 23, p. 23562, 2010.
- [36] D. Melati, A. Melloni, and F. Morichetti, "Real photonic waveguides: guiding light through imperfections," *Advances in Optics and Photonics*, vol. 6, no. 2, pp. 156–224, 2014.
- [37] P. Temple-Boyer, C. Rossi, E. Saint-Etienne, and E. Scheid, "Residual stress in low pressure chemical vapor deposition  $\text{SiN}_x$  films deposited from silane and ammonia," *Journal of Vacuum Science and Technology*, vol. A 16, no. 4, pp. 2003–2007, 1998.
- [38] A. Gondarenko, J. S. Levy, and M. Lipson, "High confinement micron-scale silicon nitride high Q ring resonator," *Optics Express*, vol. 17, no. 14, pp. 11 366–11 370, 2009.
- [39] P. Del'Haye, A. Schliesser, O. Arcizet, T. Wilken, R. Holzwarth, and T. J. Kippenberg, "Optical frequency comb generation from a monolithic microresonator," *Nature*, vol. 450, no. 7173, pp. 1214–1217, 2007.
- [40] K. H. Nam, I. H. Park, and S. H. Ko, "Patterning by controlled cracking," *Nature*, vol. 485, no. 7397, pp. 221–224, 2012.
- [41] K. Luke, A. Dutt, C. B. Poitras, and M. Lipson, "Overcoming  $\text{Si}_3\text{N}_4$  film stress limitations for high quality factor ring resonators," *Optics Express*, vol. 21, no. 19, pp. 22 829–22 833, 2013.
- [42] J. P. Epping, M. Hoekman, R. Mateman, A. Leinse, R. G. Heideman, A. van Rees, P. J. van der Slot, C. J. Lee, and K.-J. Boller, "High confinement, high yield  $\text{Si}_3\text{N}_4$  waveguides for nonlinear optical applications," *Optics Express*, vol. 23, no. 2, pp. 642–648, 2015.
- [43] M. H. P. Pfeiffer, A. Kordts, V. Brasch, M. Zervas, M. Geiselmann, J. D. Jost, and T. J. Kippenberg, "Photonic Damascene process for integrated high-Q microresonator based nonlinear photonics," *Optica*, vol. 3, no. 1, pp. 20–25, 2016.

- [44] W. T. Li, D. A. P. Bulla, and R. Boswell, "Surface oxidation of Al masks for deep dry-etch of silica optical waveguides," *Surface and Coatings Technology*, vol. 201, no. 9-11 SPEC. ISS., pp. 4979–4983, 2007.
- [45] M. H. P. Pfeiffer, C. Herkommer, J. Liu, H. Guo, M. Karpov, E. Lucas, M. Zervas, and T. J. Kippenberg, "Octave-spanning dissipative Kerr soliton frequency combs in  $\text{Si}_3\text{N}_4$  microresonators," *Optica*, vol. 4, no. 7, pp. 684–691, 2017.
- [46] H. Guo, C. Herkommer, A. Billat, D. Grassani, C. Zhang, M. H. P. Pfeiffer, W. Weng, C.-S. Brès, and T. J. Kippenberg, "Mid-infrared frequency comb via coherent dispersive wave generation in silicon nitride nanophotonic waveguides," *Nature Photonics*, vol. 12, pp. 330–335, 2018.
- [47] J. F. Bauters, M. J. R. Heck, D. D. John, M.-C. Tien, W. Li, J. S. Barton, D. J. Blumenthal, J. E. Bowers, A. Leinse, and R. G. Heideman, "Ultra-low-loss Single-mode  $\text{Si}_3\text{N}_4$  Waveguides with 0.7 dB/m Propagation Loss," in *37th ECOC*. Optical Society of America, 2011, p. Th.12.LeSaleve.3.
- [48] X. Ji, F. A. S. Barbosa, S. P. Roberts, A. Dutt, J. Cardenas, Y. Okawachi, A. Bryant, A. L. Gaeta, and M. Lipson, "Ultra-low-loss on-chip resonators with sub-milliwatt parametric oscillation threshold," *Optica*, vol. 4, no. 6, pp. 619–624, 2017.
- [49] B. Stern, X. Ji, Y. Okawachi, A. L. Gaeta, and M. Lipson, "Battery-operated integrated frequency comb generator," *Nature*, vol. 562, no. 7727, pp. 401–405, 2018.
- [50] X. Ji, J. K. Jang, U. D. Dave, M. Corato-Zanarella, C. Joshi, A. L. Gaeta, and M. Lipson, "Exploiting ultralow loss multimode waveguides for broadband frequency combs," *Laser and Photonics Reviews*, vol. 2000353, pp. 6–11, 2020.
- [51] V. Brasch, M. Geiselmann, T. Herr, G. Lihachev, M. H. P. Pfeiffer, M. L. Gorodetsky, and T. J. Kippenberg, "Photonic chip – based optical frequency comb using soliton Cherenkov radiation," *Science*, vol. 351, no. 6271, pp. 357–360, 2016.

- [52] M. H. P. Pfeiffer, J. Liu, A. S. Raja, T. Morais, B. Ghadiani, and T. J. Kippenberg, “Ultra-smooth silicon nitride waveguides based on the Damascene reflow process: fabrication and loss origins,” *Optica*, vol. 5, no. 7, pp. 884–892, 2018.
- [53] J. Liu, A. S. Raja, M. Karpov, B. Ghadiani, M. H. P. Pfeiffer, B. Du, N. J. Engelsen, H. Guo, M. Zervas, and T. J. Kippenberg, “Ultralow-power chip-based soliton microcombs for photonic integration,” *Optica*, vol. 5, no. 10, pp. 1347–1353, 2018.
- [54] J. Liu, E. Lucas, A. S. Raja, J. He, J. Riemensberger, R. N. Wang, M. Karpov, H. Guo, R. Bouchand, and T. J. Kippenberg, “Photonic microwave generation in the X- and K-band using integrated soliton microcombs,” *Nature Photonics*, vol. 14, no. 8, pp. 486–491, 2020.
- [55] Y. Xuan, Y. Liu, L. T. Varghese, A. J. Metcalf, X. Xue, P.-H. Wang, K. Han, J. A. Jaramillo-Villegas, A. Al Noman, C. Wang, S. Kim, M. Teng, Y. J. Lee, B. Niu, L. Fan, J. Wang, D. E. Leaird, A. M. Weiner, and M. Qi, “High-Q silicon nitride microresonators exhibiting low-power frequency comb initiation,” *Optica*, vol. 3, no. 11, pp. 1171–1180, 2016.
- [56] C. J. Krüchel, A. Fülöp, T. Klintberg, J. Bengtsson, P. A. Andrekson, and V. Torres-Company, “Linear and nonlinear characterization of low-stress high-confinement silicon-rich nitride waveguides,” *Optics Express*, vol. 23, no. 20, pp. 25 827–25 837, 2015.
- [57] Q. Li, T. C. Briles, D. A. Westly, T. E. Drake, J. R. Stone, B. R. Ilic, S. A. Diddams, S. B. Papp, and K. Srinivasan, “Stably accessing octave-spanning microresonator frequency combs in the soliton regime,” *Optica*, vol. 4, no. 2, pp. 193–203, 2017.
- [58] T. E. Drake, T. C. Briles, J. R. Stone, D. T. Spencer, D. R. Carlson, D. D. Hickstein, Q. Li, D. Westly, K. Srinivasan, S. A. Diddams, and S. B. Papp, “Terahertz-rate Kerr-microresonator optical clockwork,” *Physical Review X*, vol. 9, no. 3, p. 31023, 2019.
- [59] K. Wu and A. W. Poon, “Stress-released Si<sub>3</sub>N<sub>4</sub> fabrication process for dispersion-engineered integrated silicon photonics,” *Optics Express*, vol. 28, no. 12, pp. 17 708–17 722, 2020.

- [60] H. El Dirani, L. Youssef, C. Petit-Etienne, S. Kerdiles, P. Grosse, C. Monat, E. Pargon, and C. Sciancalepore, “Ultralow-loss tightly confining  $\text{Si}_3\text{N}_4$  waveguides and high-Q microresonators,” *Optics Express*, vol. 27, no. 21, pp. 30 726–30 740, 2019.
- [61] J. G. E. Gardeniers, “LPCVD silicon-rich silicon nitride films for applications in micromechanics, studied with statistical experimental design,” *Journal of Vacuum Science & Technology A: Vacuum, Surfaces, and Films*, vol. 14, no. 5, pp. 2879–2892, 1996.
- [62] P. Marin-Palomo, J. N. Kemal, M. Karpov, A. Kordts, J. Pfeifle, M. H. Pfeiffer, P. Trocha, S. Wolf, V. Brasch, M. H. Anderson, R. Rosenberger, K. Vijayan, W. Freude, T. J. Kippenberg, and C. Koos, “Microresonator-based solitons for massively parallel coherent optical communications,” *Nature*, vol. 546, no. 7657, pp. 274–279, 2017.
- [63] A. Fülöp, M. Mazur, A. Lorences-Riesgo, Ó. B. Helgason, P. H. Wang, Y. Xuan, D. E. Leaird, M. Qi, P. A. Andrekson, A. M. Weiner, and V. Torres-Company, “High-order coherent communications using mode-locked dark-pulse Kerr combs from microresonators,” *Nature Communications*, vol. 9, no. 1, p. 1598, 2018.
- [64] B. Corcoran, M. Tan, X. Xu, A. Boes, J. Wu, T. G. Nguyen, S. T. Chu, B. E. Little, R. Morandotti, A. Mitchell, and D. J. Moss, “Ultra-dense optical data transmission over standard fibre with a single chip source,” *Nature Communications*, vol. 11, no. 1, pp. 1–7, 2020.
- [65] D. T. Spencer, T. Drake, T. C. Briles, J. Stone, L. C. Sinclair, C. Fredrick, Q. Li, D. Westly, B. R. Ilic, A. Bluestone, N. Volet, T. Komljenovic, L. Chang, S. H. Lee, D. Y. Oh, M. G. Suh, K. Y. Yang, M. H. Pfeiffer, T. J. Kippenberg, E. Norberg, L. Theogarajan, K. Vahala, N. R. Newbury, K. Srinivasan, J. E. Bowers, S. A. Diddams, and S. B. Papp, “An optical-frequency synthesizer using integrated photonics,” *Nature*, vol. 557, no. 7703, pp. 81–85, 2018.
- [66] P. Trocha, D. Ganin, M. Karpov, M. H. Pfeiffer, A. Kordts, J. Krockenberger, S. Wolf, P. Marin-Palomo, C. Weimann, S. Randel, W. Freude, T. J. Kippenberg, and C. Koos, “Ultrafast optical ranging using microresonator soliton frequency combs,” *Science*, vol. 359, no. 6378, pp. 887–891, 2018.

## Bibliography

---

- [67] J. Riemensberger, A. Lukashchuk, M. Karpov, W. Weng, E. Lucas, J. Liu, and T. J. Kippenberg, “Massively parallel coherent laser ranging using a soliton microcomb,” *Nature*, vol. 581, no. 7807, pp. 164–170, 2020.
- [68] A. Dutt, C. Joshi, X. Ji, J. Cardenas, Y. Okawachi, K. Luke, A. L. Gaeta, and M. Lipson, “On-chip dual-comb source for spectroscopy,” *Science Advances*, vol. 4, no. 3, p. e1701858, 2018.
- [69] B. Shen, L. Chang, J. Liu, H. Wang, Q. F. Yang, C. Xiang, R. N. Wang, J. He, T. Liu, W. Xie, J. Guo, D. Kinghorn, L. Wu, Q. X. Ji, T. J. Kippenberg, K. Vahala, and J. E. Bowers, “Integrated turnkey soliton microcombs,” *Nature*, vol. 582, no. 7812, pp. 365–369, 2020.
- [70] H. Guo, W. Weng, J. Liu, F. Yang, W. Hänsel, C. S. Brès, L. Thévenaz, R. Holzwarth, and T. J. Kippenberg, “Nanophotonic supercontinuum-based mid-infrared dual-comb spectroscopy,” *Optica*, vol. 7, no. 9, pp. 1181–1188, 2020.
- [71] Z. Ye, K. Twayana, P. A. Andrekson, and V. Torres-Company, “High-Q Si<sub>3</sub>N<sub>4</sub> microresonators based on a subtractive processing for Kerr nonlinear optics,” *Optics Express*, vol. 27, no. 24, pp. 35 719–35 727, 2019.
- [72] S. Afshar V and T. M. monro, “A full vectorial model for pulse propagation in emerging waveguides with subwavelength structures part I: Kerr nonlinearity,” *Optics Express*, vol. 17, no. 14, pp. 2298–2318, 2009.
- [73] V. R. Almeida, R. R. Panepucci, and M. Lipson, “Nanotaper for compact mode conversion,” *Optics Letters*, vol. 28, no. 15, pp. 1302–1304, 2003.
- [74] S. Barbara, S. Barbara, S. Barbara, S. Barbara, M. Photonics, and W. Friendship, “Narrow-linewidth III-V/Si/Si<sub>3</sub>N<sub>4</sub> laser using multilayer heterogeneous integration,” *Optica*, vol. 7, no. 1, pp. 20–21, 2020.
- [75] W. Jin, Q.-F. Yang, L. Chang, B. Shen, H. Wang, M. A. Leal, L. Wu, M. Gao, A. Feshali, M. Paniccia, K. J. Vahala, and J. E. Bowers, “Hertz-linewidth semiconductor lasers using CMOS-ready ultra-high-Q microresonators,” *Nature Photonics*, 2021, <https://doi.org/10.1038/s41566-021-00761-7>.
- [76] N. Akhmediev and M. Karlsson, “Cherenkov radiation emitted by solitons in optical fibers,” *Physical Review A*, vol. 51, no. 3, pp. 2602–2607, 1995.

- 
- [77] S. P. Yu, T. C. Briles, G. T. Moille, X. Lu, S. A. Diddams, K. Srinivasan, and S. B. Papp, “Tuning Kerr-soliton frequency combs to atomic resonances,” *Physical Review Applied*, vol. 11, no. 4, p. 044017, 2019.
- [78] C. Pollock and M. Lipson, *Integrated Photonics*. Springer, 2003.
- [79] R. J. Bojko, J. Li, L. He, T. Baehr-Jones, M. Hochberg, and Y. Aida, “Electron beam lithography writing strategies for low loss, high confinement silicon optical waveguides,” *Journal of Vacuum Science & Technology B, Nanotechnology and Microelectronics: Materials, Processing, Measurement, and Phenomena*, vol. 29, no. 6, p. 06F309, 2011.
- [80] M. Cherchi, S. Ylinen, M. Harjanne, M. Kapulainen, and T. Aalto, “Dramatic size reduction of waveguide bends on a micron-scale silicon photonic platform,” *Optics Express*, vol. 21, no. 15, pp. 17 814–17 823, 2013.
- [81] T. S. T. Fujisawa, S. Makino and K. Saitoh, “Si-wire 90 ° waveguide bend using clothoid and normal curves for large scale photonic integrated circuits,” *Optics Express*, vol. 25, no. 8, pp. 9150–9159, 2017.
- [82] X. Jiang, H. Wu, and D. Dai, “Low-loss and low-crosstalk multimode waveguide bend on silicon,” *Optics Express*, vol. 26, no. 13, pp. 17 680–17 689, 2018.
- [83] T. Chen, H. Lee, J. Li, and K. J. Vahala, “A general design algorithm for low optical loss adiabatic connections in waveguides,” *Optics Express*, vol. 20, no. 20, pp. 22 819–22 829, 2012.
- [84] D. J. WALTON, “Spiral Spline Curves for Highway Design,” *Computer-Aided Civil and Infrastructure Engineering*, vol. 4, no. 2, pp. 99–106, 1989.
- [85] R. Levien, “From spiral to spline: optimal techniques in interactive curve design,” Ph.D. dissertation, 2009.
- [86] T. Barwicz, H. A. Haus, and L. Fellow, “Three-dimensional analysis of scattering losses due to sidewall roughness in microphotonic waveguides,” vol. 23, no. 9, pp. 2719–2732, 2005.

## Bibliography

---

- [87] C. G. Poulton, C. Koos, M. Fujii, A. Pfrang, T. Schimmel, J. Leuthold, and W. Freude, "Radiation modes and roughness loss in high index-contrast waveguides," *IEEE Journal on Selected Topics in Quantum Electronics*, vol. 12, no. 6, pp. 1306–1320, 2006.
- [88] K. K. Lee, D. R. Lim, H. C. Luan, A. Agarwal, J. Foresi, and L. C. Kimerling, "Effect of size and roughness on light transmission in a Si/SiO<sub>2</sub> waveguide: Experiments and model," *Applied Physics Letters*, vol. 77, no. 11, pp. 1617–1619, 2000.
- [89] D. Marcuse, *Theory of dielectric optical waveguides*, 2nd ed., 1991.
- [90] S. P. Roberts, X. Ji, J. Cardenas, A. Bryant, and M. Lipson, "Sidewall roughness in Si<sub>3</sub>N<sub>4</sub> waveguides directly measured by atomic force microscopy," in *Conference on Lasers and Electro-Optics*, 2017, p. SM3K.6.
- [91] F. Morichetti, A. Canciamilla, C. Ferrari, M. Torregiani, A. Melloni, and M. Martinelli, "Roughness induced backscattering in optical silicon waveguides," *Physical Review Letters*, vol. 104, no. 3, pp. 1–4, 2010.
- [92] K. O. Bugaev, A. A. Zelenina, and V. A. Volodin, "Vibrational spectroscopy of chemical species in silicon and silicon-rich nitride thin films," *International Journal of Spectroscopy*, vol. 2012, p. 281851, 2012.
- [93] H. J. Stein and H. A. R. Wegener, "Chemically bound hydrogen in CVD Si<sub>3</sub>N<sub>4</sub>: dependence on NH<sub>3</sub>/SiH<sub>4</sub> ratio and on annealing," *Journal of The Electrochemical Society*, vol. 124, no. 6, pp. 908–912, 1977.
- [94] T. Makino, "Composition and structure control by source gas ratio in LPCVD SiN<sub>x</sub>," *Journal of The Electrochemical Society*, vol. 130, no. 2, p. 450, 1983.
- [95] K. Luke, Y. Okawachi, M. R. E. Lamont, A. L. Gaeta, and M. Lipson, "Broadband mid-infrared frequency comb generation in a Si<sub>3</sub>N<sub>4</sub> microresonator," *Optics Letters*, vol. 40, no. 21, pp. 4823–4826, 2015.
- [96] D. Dong, E. A. Irene, and D. R. Young, "Preparation and some properties of chemically vapor-deposited Si-rich SiO<sub>2</sub> and Si<sub>3</sub>N<sub>4</sub> Films," vol. 123, no. 5, pp. 819–823, 1978.

- [97] K. N. Andersen, W. E. Svendsen, T. Stimpel-Lindner, T. Sulima, and H. Baumgärtner, “Annealing and deposition effects of the chemical composition of silicon-rich nitride,” *Applied Surface Science*, vol. 243, no. 1-4, pp. 401–408, 2005.
- [98] P. Rabiei, W. H. Steier, C. Zhang, and L. R. Dalton, “Polymer micro-ring filters and modulators,” *Journal of Lightwave Technology*, vol. 20, no. 11, pp. 1968–1975, 2002.
- [99] M. L. Gorodetsky, A. D. Pryamikov, and V. S. Ilchenko, “Rayleigh scattering in high-Q microspheres,” *Journal of Optical Society of America*, vol. 17, no. 6, pp. 1051–1057, 2000.
- [100] A. Li, T. Van Vaerenbergh, P. De Heyn, P. Bienstman, and W. Bogaerts, “Backscattering in silicon microring resonators: A quantitative analysis,” *Laser and Photonics Reviews*, vol. 10, no. 3, pp. 420–431, 2016.
- [101] Q. Li, A. A. Eftekhar, Z. Xia, and A. Adibi, “Unified approach to mode splitting and scattering loss in high-Q whispering-gallery-mode microresonators,” *Physical Review A - Atomic, Molecular, and Optical Physics*, vol. 88, no. 3, pp. 1–11, 2013.
- [102] M. H. Pfeiffer, J. Liu, M. Geiselmann, and T. J. Kippenberg, “Coupling Ideality of Integrated Planar High- Q Microresonators,” *Physical Review Applied*, vol. 7, no. 2, p. 024026, 2017.
- [103] D. T. Spencer, J. F. Bauters, M. J. R. Heck, and J. E. Bowers, “Integrated waveguide coupled Si<sub>3</sub>N<sub>4</sub> resonators in the ultrahigh-Q regime,” *Optica*, vol. 1, no. 3, pp. 153–157, 2014.
- [104] E. D. Moore, “Advances in Swept-Wavelength Interferometry for Precision Measurements,” Ph.D. dissertation, 2011.
- [105] A. M. Weiner, *Ultrafast optics*, 2009.
- [106] B. J. Soller, D. K. Gifford, M. S. Wolfe, and M. E. Froggatt, “High resolution optical frequency domain reflectometry for characterization of components and assemblies,” *Optics Express*, vol. 13, no. 2, pp. 666–674, 2005.

## Bibliography

---

- [107] P. Del’Haye, O. Arcizet, M. L. Gorodetsky, R. Holzwarth, and T. J. Kippenberg, “Frequency comb assisted diode laser spectroscopy for measurement of microcavity dispersion,” *Nature Photonics*, vol. 3, no. 9, pp. 529–533, 2009.
- [108] G. P. Agrawal, *Nonlinear Fiber Optics Fifth Edition*, 2007.
- [109] K. Ikeda, R. E. Saperstein, N. Alic, and Y. Fainman, “Thermal and Kerr nonlinear properties of plasma-deposited silicon nitride/ silicon dioxide waveguides,” *Optics Express*, vol. 16, no. 17, pp. 12 987–12 994, 2008.
- [110] A. Boskovic, L. Gruner-Nielsen, O. A. Levring, S. V. Chernikov, and J. R. Taylor, “Direct continuous-wave measurement of  $n_2$  in various types of telecommunication fiber at 1.55  $\mu\text{m}$ ,” *Optics Letters*, vol. 21, no. 24, p. 1966, 1996.
- [111] C. M. Caves, “Quantum limits on noise in linear amplifiers,” *Physical Review D*, vol. 26, no. 8, pp. 1817–1839, 1982.
- [112] J. A. Levenson, P. Grangier, I. Abram, and T. Rivera, “Reduction of quantum noise in optical parametric amplification,” *Journal of the Optical Society of America B*, vol. 10, no. 11, p. 2233, 1993.
- [113] J. Hansryd, P. A. Andrekson, M. Westlund, J. Li, and P. O. Hedekvist, “Fiber-based optical parametric amplifiers and their applications,” *IEEE Journal on Selected Topics in Quantum Electronics*, vol. 8, no. 3, pp. 506–520, 2002.
- [114] S. Xing, D. Grassani, S. Kharitonov, L. Brilland, C. Caillaud, J. Trolès, and C.-S. Brès, “Mid-infrared continuous-wave parametric amplification in chalcogenide microstructured fibers,” *Optica*, vol. 4, no. 6, p. 643, 2017.
- [115] M. A. Foster, A. C. Turner, J. E. Sharping, B. S. Schmidt, M. Lipson, and A. L. Gaeta, “Broad-band optical parametric gain on a silicon photonic chip,” *Nature*, vol. 441, no. 7096, pp. 960–963, 2006.
- [116] X. Liu, R. M. Osgood, Y. A. Vlasov, and W. M. Green, “Mid-infrared optical parametric amplifier using silicon nanophotonic waveguides,” *Nature Photonics*, vol. 4, no. 8, pp. 557–560, 2010.

- [117] A. Gajda, L. Zimmermann, M. Jazayerifar, G. Winzer, H. Tian, R. Elschner, T. Richter, C. Schubert, B. Tillack, and K. Petermann, “Highly efficient CW parametric conversion at 1550 nm in SOI waveguides by reverse biased p-i-n junction,” *Optics Express*, vol. 20, no. 12, p. 13100, 2012.
- [118] K. J. A. Ooi, D. K. T. Ng, T. Wang, A. K. L. Chee, S. K. Ng, Q. Wang, L. K. Ang, A. M. Agarwal, L. C. Kimerling, and D. T. H. Tan, “Pushing the limits of CMOS optical parametric amplifiers with USRN:Si<sub>7</sub>N<sub>3</sub> above the two-photon absorption edge,” *Nature Communications*, vol. 8, p. 13878, 2017.
- [119] Y. Zhang, C. Reimer, J. Wu, P. Roztocky, B. Wetzels, B. E. Little, S. T. Chu, D. J. Moss, B. J. Eggleton, M. Kues, and R. Morandotti, “Multichannel phase-sensitive amplification in a low-loss CMOS-compatible spiral waveguide,” *Optics Letters*, vol. 42, no. 21, p. 4391, 2017.
- [120] R. H. Stolen and J. E. Bjorkholm, “Parametric Amplification and Frequency,” *IEEE Journal of Quantum Electronics*, vol. 18, no. 7, pp. 1062–1072, 1982.
- [121] P. Zhao, Z. Ye, K. Vijayan, C. Naveau, J. Schröder, M. Karlsson, and P. A. Andrekson, “Waveguide tapering for improved parametric amplification in integrated nonlinear Si<sub>3</sub>N<sub>4</sub> waveguides,” *Optics Express*, vol. 28, no. 16, p. 23467, 2020.
- [122] J. E. Heebner and R. W. Boyd, “Enhanced all-optical switching by use of a nonlinear fiber ring resonator,” *Optics Letters*, vol. 24, no. 12, p. 847, 1999.
- [123] C. Godey, I. V. Balakireva, A. Coillet, and Y. K. Chembo, “Stability analysis of the spatiotemporal Lugiato-Lefever model for Kerr optical frequency combs in the anomalous and normal dispersion regimes,” *Physical Review A - Atomic, Molecular, and Optical Physics*, vol. 89, no. 6, 2014.
- [124] T. Herr, V. Brasch, J. D. Jost, C. Y. Wang, N. M. Kondratiev, M. L. Gorodetsky, and T. J. Kippenberg, “Temporal solitons in optical microresonators,” *Nature Photonics*, vol. 8, no. 2, pp. 145–152, 2014.
- [125] A. B. Matsko, A. A. Savchenkov, and L. Maleki, “Normal group-velocity dispersion Kerr frequency comb,” *Optics Letters*, vol. 37, no. 1, pp. 43–45, 2012.

## Bibliography

---

- [126] X. Xue, Y. Xuan, Y. Liu, P.-H. Wang, S. Chen, J. Wang, D. E. Leaird, M. Qi, and A. M. Weiner, “Mode-locked dark pulse Kerr combs in normal-dispersion microresonators,” *Nature Photonics*, vol. 9, no. 9, pp. 594–600, 2015.
- [127] Ó. B. Helgason, F. R. Arteaga-Sierra, Z. Ye, K. Twayana, P. A. Andrekson, M. Karlsson, J. Schröder, and Victor Torres-Company, “Dissipative solitons in photonic molecules,” *Nature Photonics*, 2021, <http://arxiv.org/abs/1809.08637>.
- [128] T. Herr, V. Brasch, J. D. Jost, C. Y. Wang, N. M. Kondratiev, M. L. Gorodetsky, and T. J. Kippenberg, “Temporal solitons in optical microresonators,” *Nature Photonics*, vol. 8, no. 2, pp. 145–152, 2014.
- [129] P. Emplit, J. P. Hamaide, F. Reynaud, C. Froehly, and A. Barthelemy, “Picosecond steps and dark pulses through nonlinear single mode fibers,” *Optics Communications*, vol. 62, no. 6, pp. 374–379, 1987.
- [130] X. Xue, P. H. Wang, Y. Xuan, M. Qi, and A. M. Weiner, “Microresonator Kerr frequency combs with high conversion efficiency,” *Laser and Photonics Reviews*, vol. 11, no. 1, p. 1600276, 2017.
- [131] K. Ikeda, “Multiple-valued stationary state and its instability of the transmitted light by a ring cavity system,” *Optics Communications*, vol. 30, no. 2, pp. 257–261, 1979.
- [132] L. A. Lugiato and R. Lefever, “Spatial dissipative structures in passive optical systems,” *Physical Review Letters*, vol. 58, no. 21, pp. 2209–2211, 1987.
- [133] A. Fülöp, M. Mazur, A. Lorences-Riesgo, Ó. B. Helgason, P. H. Wang, Y. Xuan, D. E. Leaird, M. Qi, P. A. Andrekson, A. M. Weiner, and V. Torres-Company, “High-order coherent communications using mode-locked dark-pulse Kerr combs from microresonators,” *Nature Communications*, vol. 9, no. 1, p. 1598, 2018.
- [134] V. Torres-Company, J. Schroder, A. Fulop, M. Mazur, L. Lundberg, O. B. Helgason, M. Karlsson, and P. A. Andrekson, “Laser frequency combs for coherent optical communications,” *Journal of Lightwave Technology*, vol. 37, no. 7, pp. 1663–1670, 2019.

- [135] D. Kong, A. A. Jørgensen, M. R. Henriksen, F. Klejs, Z. Ye, Ø. B. Helgason, H. E. Hansen, H. Hu, M. Yankov, S. Forchhammer, P. Andrekson, A. Larsson, M. Karlsson, J. Schröder, Y. Sasaki, K. Aikawa, J. W. Thomsen, T. Morioka, M. Galili, V. Torres-Company, and L. K. Oxenløwe, “Single Dark-Pulse Kerr Comb Supporting 1.84 Pbit/s Transmission over 37-Core Fiber,” in *Conference on Lasers and Electro-Optics*. Optical Society of America, 2020, p. JTh4A.7.
- [136] Ó. B. Helgason, A. Fülöp, J. Schröder, P. A. Andrekson, A. M. Weiner, and V. Torres-Company, “Superchannel engineering of microcombs for optical communications,” *Journal of the Optical Society of America B*, vol. 36, no. 8, p. 2013, 2019.
- [137] T. Herr, V. Brasch, J. D. Jost, I. Mirgorodskiy, G. Lihachev, M. L. Gorodetsky, and T. J. Kippenberg, “Mode spectrum and temporal soliton formation in optical microresonators,” *Physical Review Letters*, vol. 113, no. 12, p. 123901, 2014.
- [138] H. Nejadriahi, A. Friedman, R. Sharma, S. Pappert, Y. Fainman, and P. Yu, “Thermo-optic properties of silicon-rich silicon nitride for on-chip applications,” *Opt. Express*, vol. 28, no. 17, pp. 24 951–24 960, 2020.
- [139] J. Liu, A. S. Raja, M. Karpov, B. Ghadiani, M. H. P. Pfeiffer, B. Du, N. J. Engelsen, H. Guo, M. Zervas, and T. J. Kippenberg, “Ultralow-power chip-based soliton microcombs for photonic integration,” *Optica*, vol. 5, no. 10, pp. 1347–1353, 2018.
- [140] X. Xue, Y. Xuan, C. Wang, P.-H. Wang, Y. Liu, B. Niu, D. E. Leaird, M. Qi, and A. M. Weiner, “Thermal tuning of Kerr frequency combs in silicon nitride microring resonators,” *Optics Express*, vol. 24, no. 1, p. 687, 2016.
- [141] C. Joshi, J. K. Jang, K. Luke, X. Ji, S. A. Miller, A. Klenner, Y. Okawachi, M. Lipson, and A. L. Gaeta, “Thermally Controlled Comb Generation and Soliton Modelocking in Microresonators,” *Optics Letters*, vol. 41, no. 11, pp. 2565–2568, 2016.
- [142] W. Lin, K. Benson, and R. Levy, *Microelectronic Materials and Processes*, 1989.

## Bibliography

---

- [143] S.-L. Zhang, J.-T. Wang, W. Kaplan, and M. Östling, “Silicon nitride films deposited from  $\text{SiH}_2\text{Cl}_2$   $\text{NH}_3$  by low pressure chemical vapor deposition: kinetics, thermodynamics, composition and structure,” *Thin Solid Films*, vol. 213, no. 2, pp. 182–191, 1992.
- [144] C. Yang and J. Pham, “Characteristic Study of Silicon Nitride Films Deposited by LPCVD and PECVD,” *Silicon*, vol. 10, no. 6, pp. 2561–2567, 2018.
- [145] M. H. P. Pfeiffer, C. Herkommer, J. Liu, T. Morais, M. Zervas, M. Geiselmann, and T. J. Kippenberg, “Photonic damascene process for low-loss, high-confinement silicon nitride waveguides,” *IEEE Journal of Selected Topics in Quantum Electronics*, vol. 24, no. 4, pp. 1–11, 2018.
- [146] R. J. Bojko, J. Li, L. He, T. Baehr-Jones, M. Hochberg, and Y. Aida, “Electron beam lithography writing strategies for low loss, high confinement silicon optical waveguides,” *Journal of Vacuum Science & Technology B*, vol. 29, no. 6, p. 06F309, 2011.
- [147] Shane Patrick, R. J. Bojko, S. J. H. Stammberger, E. Luan, and L. Chrostowski, “Improvement of silicon waveguide transmission by advanced e-beam lithography data fracturing strategies,” *Journal of Vacuum Science & Technology B, Nanotechnology and Microelectronics: Materials, Processing, Measurement, and Phenomena*, vol. 35, no. 6, p. 06G504, 2017.
- [148] R. K. Dey and B. Cui, “Stitching error reduction in electron beam lithography with in-situ feedback using self-developing resist,” *Journal of Vacuum Science & Technology B, Nanotechnology and Microelectronics: Materials, Processing, Measurement, and Phenomena*, vol. 31, no. 6, p. 06F409, 2013.
- [149] J. W. Coburn and H. F. Winters, “Plasma etching — a discussion of mechanisms,” *Critical Reviews in Solid State and Materials Sciences*, vol. 10, no. 2, pp. 119–141, 1981.
- [150] J. Dulak, B. J. Howard, and C. Steinbrüchel, “Etch mechanism in the reactive ion etching of silicon nitride,” *Journal of Vacuum Science & Technology A: Vacuum, Surfaces, and Films*, vol. 9, no. 3, pp. 775–778, 1991.

- [151] D. Field, "Spectroscopic studies of fluorescent emission in plasma etching of silicon nitride," *Journal of Vacuum Science & Technology B: Microelectronics and Nanometer Structures*, vol. 6, no. 2, p. 551, 1988.
- [152] T. C. Mele, J. Nulman, and J. P. Krusius, "Selective and anisotropic reactive ion etch of LPCVD silicon nitride with CHF<sub>3</sub> based gases." *Journal of Vacuum Science and Technology B: Microelectronics and Nanometer Structures*, vol. 2, no. 4, pp. 684–687, 1984.
- [153] Y. X. Li, P. J. French, and R. F. Wolffenbuttel, "Selective reactive ion etching of silicon nitride over silicon using CHF<sub>3</sub> with N<sub>2</sub> addition," *Journal of Vacuum Science and Technology B: Microelectronics and Nanometer Structures*, vol. 13, no. 5, pp. 2008–2012, 1995.
- [154] B. E. Deal and A. S. Grove, "General relationship for the thermal oxidation of silicon," *Journal of Applied Physics*, vol. 36, no. 12, pp. 3770–3778, 1965.
- [155] L. Wu, H. Wang, Q. Yang, Q.-x. Ji, B. Shen, C. Bao, M. Gao, and K. Vahala, "Greater than one billion Q factor for on-chip microresonators," *Optics Letters*, vol. 45, no. 18, pp. 5129–5131, 2020.
- [156] R. Miller, M. C. Öztürk, J. J. Wortman, F. S. Johnson, and D. T. Grider, "LPCVD of silicon dioxide by pyrolysis of teos in a rapid thermal processor," *Materials Letters*, vol. 8, no. 9, pp. 353–356, 1989.
- [157] Y. Xuan, Y. Liu, L. T. Varghese, A. J. Metcalf, X. Xue, P.-H. Wang, K. Han, J. A. Jaramillo-Villegas, A. Al Noman, C. Wang, S. Kim, M. Teng, Y. J. Lee, B. Niu, L. Fan, J. Wang, D. E. Leaird, A. M. Weiner, and M. Qi, "High-Q silicon nitride microresonators exhibiting low-power frequency comb initiation," *Optica*, vol. 3, no. 11, pp. 1171–1180, 2016.
- [158] N. Bai, X. Zhu, Y. Zhu, W. Hong, and X. Sun, "Tri-layer gradient and polarization-selective vertical couplers for interlayer transition," *Optics Express*, vol. 28, no. 15, p. 23048, 2020.
- [159] R. S. Tummidi and M. Webster, "Multilayer Silicon Nitride-based Coupler Integrated into a Silicon Photonics Platform with <1 dB Coupling Loss to a Standard SMF over O, S, C and L optical bands," in *Optical Fiber Communication Conference (OFC) 2020*, ser. OSA Technical Digest. San Diego: Optical Society of America, 2020, p. Th2A.10.